The Thesis Committee for Stephanie Gabrielle Konarski
Certifies that this is the approved version of the following thesis:

Nonlinear Acoustic and Dynamic Response of Heterogeneous Materials Containing Snapping Acoustic Metamaterial Inclusions

APPROVED BY

SUPERVISING COMMITTEE:

Mark F. Hamilton, Supervisor

Michael R. Haberman, Co-Supervisor

Nonlinear Acoustic and Dynamic Response of Heterogeneous Materials Containing Snapping Acoustic Metamaterial Inclusions

by

Stephanie Gabrielle Konarski, B.S.

THESIS

Presented to the Faculty of the Graduate School of

The University of Texas at Austin

in Partial Fulfillment

of the Requirements

for the Degree of

MASTER OF SCIENCE IN ENGINEERING

THE UNIVERSITY OF TEXAS AT AUSTIN

August 2014

Acknowledgments

First and foremost, I would like to thank my advisor, Dr. Michael R. Haberman, and secondary advisor, Dr. Mark F. Hamilton, whose guidance is invaluable and patience is very much appreciated. I would also like to acknowledge the Applied Research Laboratories at the University of Texas at Austin for awarding me the McKinney Fellowship in Acoustics. which has allowed me the opportunity to pursue an interesting research topic that I love. Finally, thank you to all my friends who have kept me sane over the years and provided the helpful advice and random distractions I needed to write this thesis.

Nonlinear Acoustic and Dynamic Response of Heterogeneous Materials Containing Snapping Acoustic Metamaterial Inclusions

Stephanie Gabrielle Konarski, M.S.E.
The University of Texas at Austin, 2014

Supervisors: Mark F. Hamilton
Michael R. Haberman

Acoustic metamaterials are sub-wavelength structures designed to overcome limitations in the material properties of conventional materials. The present research focuses on the nonlinear acoustic and dynamic response of a specific type of engineered microstructure called a snapping acoustic metamaterial (SAMM). Snapping of these elements is defined as large, rapid deformations induced by infinitesimal perturbations in the time-varying external pressure. Snapping behavior in SAMM elements results from their non-monotonic stress-strain response, which displays regimes of positive and negative stiffness. This work presents a modeling study of the nonlinear behavior of both individual SAMM elements and a heterogeneous material containing a dilute concentration of SAMM elements embedded in a nearly incompressible viscoelastic solid. Two different scenarios are considered: (i) nonlinear wave

propagation in the heterogeneous medium, and (*ii*) forced nonlinear dynamics of inclusions embedded in a viscoelastic medium. The nonlinearity of the SAMM elements is represented by a cubic pressure-volumetric strain relationship based on finite element model results from previous work. The effective nonlinear response of a heterogeneous mixture of SAMM elements embedded in a matrix, characterized by the parameters B/A and C/A, is then determined using both a nonlinear mixture law and a nonlinear Hashin-Shtrikman approach. The former estimate is limited to matrix materials with zero shear modulus, which cannot stabilize SAMM inclusions in regimes of negative stiffness. The augmented Hashin-Shtrikman method, however, includes nonlinear elasticity and the shear modulus of the matrix material. It therefore provides accurate estimates of the homogenized material when SAMM elements display negative stiffness and enhanced acoustical nonlinearity. The distortion of an acoustic wave propagating through the effective medium is studied through numerical solution of a nonlinear evolution equation that includes both quadratic and cubic nonlinearity. Finally, the forced nonlinear dynamic response of both a single SAMM element in a matrix and a domain of effective medium material embedded in matrix is considered. This behavior is of interest for generating enhanced absorption of acoustic wave energy because snapping leads to large hysteresis in the stress-strain response. A generalized Rayleigh-Plesset analysis is adapted to model the large-deformation dynamics associated with the system.

Table of Contents

List of Tables

List of Figures

Chapter 1

Introduction

1.1 Motivation

The world is filled with complex heterogeneous media that are studied for various applications in engineering. Some, like ocean sediments, biological tissue, wood and polycrystalline metals, are readily found in nature, while others, generally referred to as composite materials or "composites", are designed to elicit a specific response. Research on the properties of composites rapidly accelerated in the 1960s when technological advances allowed the creation of such heterogeneous materials [1]. Although composites containing natural materials may offer an increased or altered response over a single phased materials [2], their overall behavior is limited by the constituent materials used to create the composite. For example, it is well known that large amplitude waves will distort when propagating in a material that demonstrates a nonlinear stress-strain response in the presence of sufficiently weak losses [3]. The nonlinearity in the response of the medium, known as the material nonlinearity, is not only limited by the currently available constituent materials, but is also dominated by second order strain effects, often referred to as quadratic nonlinearity. Higher order effects, such as a dependence on cubic strain contributions, are usually negligible, and the ability to engineer the nonlinear response of a ma-

terial is currently very limited. However, cubic material nonlinearity and the ability to tailor both the quadratic and cubic nonlinear response are of interest because they may offer unique capabilities for improved resolution in acoustic imaging [4] or one-way propagation of acoustic energy [5]. Another trade-off of interest to the engineering community involves energy dissipation and mechanical stiffness of the medium [6]. In general, there is an inverse relationship between these two material properties; compliant materials provide high mechanical damping while the converse is true for stiff materials. The ability to produce composites that are both lossy and stiff is of significant interest to make improved devices and structures that isolate acoustical and vibratory disturbances. In an attempt to expand the range of attainable material properties offered by current composites, science has turned to a new class of materials that exploits small-scale structures to generate unconventional material response. The new heterogeneous media are referred to as "metamaterials".

1.2 Metamaterials

The term metamaterials describes a class of engineered sub-wavelength structures designed to produce overall properties (usually dynamic) that are unattainable with conventional materials. The term has been adopted in multiple disciplines, but is primarily of interest in the fields of electromagnetics and acoustics. The concept of metamaterials originated in the field of electromagnetism in the late twentieth century but the underlying principles quickly

became a topic of research in the field of acoustic and elastic materials [7, 8].

Although studies of metamaterials is a very recent development, related concepts do appear sparingly in the literature. For example, in the late nineteenth century, William Thomson (Lord Kelvin) suggested that longitudinal light waves with a velocity of zero are achievable if the æther, then considered to be an elastic medium, had a negative compressibility [9]. The most notable early example arose in the late 1960s when Veselago theoretically proposed an electromagnetic material with negative values of both the relative permittivity and permeability to achieve a negative refractive index [10]. The concept of negative constitutive properties remained an academic enigma for three decades until research on electromagnetic metamaterials finally rendered the study of those properties feasible [11]. Extensive theoretical efforts paired with experimental validation and useful applications of physically realizable structures with negative effective constitutive properties then emerged. Research of such materials has since evolved into the field of high interest it is today [12].

Researchers began to pursue the acoustic equivalent of the electromagnetic metamaterials shortly after experimental evidence confirmed theoretical predictions in electromagnetism. Acoustic metamaterials include heterogeneous materials displaying negative mass density or negative elastic stiffness, or materials where both these properties are negative. There have also been recent interest in acoustic metamaterials displaying nonlinear response [13, 14]. Some salient examples of acoustic metamaterials and related devices are high-

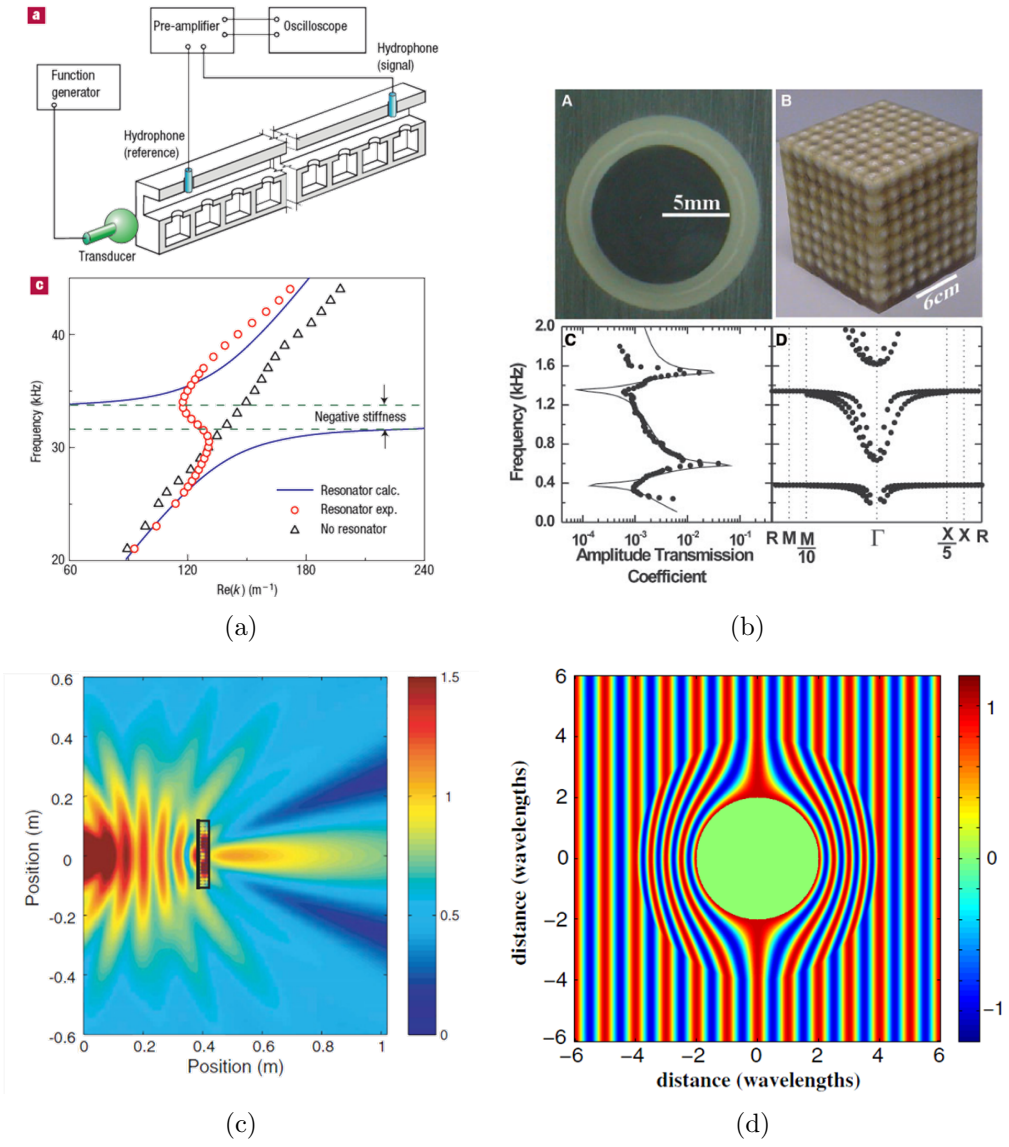

(a) (b)

(c) (d)

Figure 1.1: Examples of acoustic metamaterials: (a) Experimental chain of Helmholtz resonators with negative stiffness and dispersion response taken from Figure 2 in Ref. [15]; (b) Coated sphere that makes up sonic crystal and the measured response taken from Figure 1 in Ref. [16]; (c) Pressure field for an actual structured acoustic lens taken from Figure 4 in Ref. [17]; and (d) Pressure field with acoustic cloaking shell taken from Figure 2 in Ref. [18].

lighted in Fig. 1.1.

The non-intuitive concept of negative mass density can be demonstrated using Newton's second law of motion, $F = m\ddot{u}$, where F is an external excitation force required to provided an acceleration $\ddot{u}$ to mass m. If one considers lossless, time-harmonic motion, the displacement can be given by $u = u_0 \cos \omega t$ and the acceleration by

$$\ddot{u} = -\omega^2 u_0 \cos \omega t = \omega^2 u_0 \cos (\omega t + \pi) .$$

Expressing the acceleration in terms of the phase shift, π, indicates that the acceleration is always π out of phase with the displacement. The time-harmonic force required to impose the displacement will have a phase angle, φ, with respect to the displacement and is expressed as

$$F = F_0 \cos (\omega t + \varphi) = m\omega^2 u_0 \cos (\omega t + \pi)$$

where the amplitudes F_0 and u_0 are always positive. For a conventional systems with $m > 0$, one must have $\varphi = \pi$. Thus the excitation force is exactly in phase with the acceleration and π out of phase with the displacement. However, if the force is exactly in phase with the displacement, which occurs when $\varphi = 0$, the force must be π out of phase with the acceleration of the mass. This reversal of the common understanding of Newton's second law can be re-interpreted as a case where the force and acceleration are in phase, but the mass is assigned an effective value that is less than zero: $m < 0$. Physically, this corresponds to the metamaterial moving out of phase with the rest of the

structure. Examples of effective negative mass density arise when a system comprised of multiple, individual masses is approximated as a single effective mass [19].

Negative stiffness, which refers to a decreasing incremental resistance to an imposed increase in deformation, also characterizes an effective response. This can be understood in a manner similar to that shown for the negative effective mass density. The force, F, is related to the deformation, Δu, of a spring or medium with generalized stiffness k, such that $F = k\Delta u$. If the motion is once again considered to be time-harmonic, with $\Delta u = u_0 \cos \omega t$, then the excitation force is given by

$$F = F_0 \cos(\omega t + \varphi) = k u_0 \cos \omega t,$$

where the amplitudes F_0 and u_0 are always positive. Conventional, positive stiffness with $k > 0$ characterizes mechanical systems with an external excitation force that is in phase ($\varphi = 0$) with the deformation and the restoring force generated resists the deformation applied to its surroundings. The converse is true for negative stiffness, for which the applied force is $\varphi = \pi$ out of phase with the deformation. For a system exhibiting quasi-static negative stiffness, the internal energy versus imposed strain has negative curvature, implying that the system can *assist* the deformation induced by an externally applied force [20]. Negative stiffness can be generated either dynamically or structurally and the distinction between the two is detailed in Section 1.2.1. In either case, the response of a system with negative mass density or negative

stiffness reverses the behavior that one expects to observe with conventional materials. Research has shown that while continuous materials cannot possess negative stiffness or density, it is possible to achieve negative effective parameters by engineering sub-wavelength structures with hidden degrees of freedom to induce local resonances [15, 16] or internal energy with regions of negative curvature [21].

1.2.1 Negative Stiffness

The research detailed in this thesis is focused on the nonlinear response of acoustic metamaterial elements that have been designed to exhibit negative stiffness. It is therefore important to note the differences between the two distinct phenomena that this topic refers to in the literature. The first type employs sub-wavelength dynamics to elicit dynamic negative stiffness. Specifically, these metamaterials achieve effective negative properties from the locally resonant response of the system. The effective dynamic stiffness is only negative for a finite range of frequencies and is restricted to occur near the resonance of the system [15]. The majority of acoustic metamaterial literature on negative stiffness involves dynamic negative effective moduli achieved through such resonant effects.

Conversely, non-resonant acoustic metamaterials attain static negative moduli due to structural instabilities. The physical behavior associated with this type of negative stiffness is not restricted to a finite range of operating frequencies near a resonance of the sub-wavelength structure [6]. This con-

cept of negative stiffness can be elicited from buckling behavior of elements such as beams or thin shells, which has been studied in detail since the initial work of Leonhard Euler in the eighteenth century and predates modern consideration of acoustic metamaterials [22]. The original goal of research on structural buckling was to avoid the buckling instabilities because they lead to mechanical failure of the structures. Dynamic buckling with snap-through, or snapping, refers to a nonlinear response characterized by large, rapid displacements due to an infinitesimal change in the loading force [23]. As the structure approaches the buckling state, there is a decreasing resistance to the increasing loading force. Once the structure reaches a critical load, negative stiffness behavior will be observed for a displacement control loading. Although the term 'metamaterial' was not coined until decades later, the physical behavior associated with the buckling response of sub-wavelength structures is the underlying principal of the second type of negative stiffness studied with regard to acoustic metamaterials, which exploit, rather than avoid, the elastic instabilities.

When the dynamic stiffness of a material for certain frequencies is negative, as with the resonant metamaterials, the overall static elastic parameters are still positive and the system is structurally stable. Overall stability, however, is unattainable with static negative stiffness [24]. Although metamaterials that derive their exotic properties from resonant effects have the advantage of being statically stable, there are substantial disadvantages associated with the dependence on resonant effects. First, there is a limited frequency range

in which these materials can operate, which may impose restrictions on the versatility of the material. Second, internal losses can affect the resonance of a physical system, potentially diminishing the intended response [21]. Therefore, it is of interest to consider non-resonant acoustic metamaterials to overcome these limitations.

Though acoustic metamaterials displaying non-resonant negative stiffness is of interest, it is well known that static negative stiffness is unstable. For a heterogeneous material containing elements that rely on structural negative stiffness, the negative values of the microscopic elastic moduli may cause the macroscopic static stiffness to also be negative, resulting in overall instability. Fortunately, it is possible to constrain a negative stiffness element within a surrounding positive stiffness material to yield a stable heterogeneous medium that is characterized by positive effective stiffness [6]. Therefore, configurations are sought with overall positive static moduli that take advantage of the microscale structural instabilities, but are stabilized by a positive stiffness matrix to elicit the interesting response associated with negative stiffness while eliminating the limitations of relying on resonant effects.

1.3 Related Examples and Applications

The acoustic metamaterials of interest here offer unique means of generating strong nonlinearities, which is a relatively new area of study in the field of acoustic metamaterials. In order to provide a background on related research, the present section is divided into two subsections: linear acous-

tic metamaterials and nonlinear systems. Linear acoustic metamaterials are more widely studied than nonlinear acoustic metamaterials and thus appear more prevalently in the literature. Several examples of systems with negative material properties, including both dynamic negative stiffness and structural negative stiffness, are described in Section 1.3.1. The nonlinear response of acoustic metamaterial elements and heterogeneous acoustic metamaterials is the primary focus of this work. Section 1.3.2 therefore provides examples of related nonlinear systems including applications of nonlinear acoustic metamaterials.

1.3.1 Linear Acoustic Metamaterials

In recent years, the study of linear acoustic metamaterials have surfaced for a variety of applications, which are divided into two categories here. The first involves the ability of the effective medium to manipulate an incident acoustic wave and the second focuses on the dissipation of mechanical energy.

1.3.1.1 Wave Manipulation Due to Resonant Effects

Whether or not a medium can support wave propagation and how any subsequent waves propagate through the medium are of significant interest within the field of acoustics. A frequency range for which waves cannot propagate for periodic media is called a band gap or stop band. Combinations of different conventional solids and fluids have been utilized to design sonic crystals with different or wider frequency ranges of the band gap [25]. Sonic

crystals are synthetic, periodic structures with spatially varying material properties, such as stiffness or density. The resulting dynamic response of the sonic crystal is highly dependent upon the constitutive relationship of its components, the periodicity and shape of the heterogeneities, and sometimes even the external forces imposed on the system [26]. Within the field of acoustic metamaterials, it has been found that the negative material properties offer the ability to alter the characteristics of the band gaps to provide very high levels of acoustic isolation using a sub-wavelength structure. One of the earliest examples of acoustic metamaterials involved the fabrication of locally resonant sonic crystals comprised of thinly coated, high density spheres embedded in a polymer [16]. That experiment proved it was possible to tune the band gap by varying parameters of the heterogeneous medium, such as sub-wavelength geometry and material properties of the constituents. Although Liu *et al.* claimed the locally sonic crystals measured in Ref. [16] exhibited negative stiffness, later analysis showed that the behavior they observed was due to an effective negative mass density [27]. Acoustic metamaterials that actually displayed dynamic negative stiffness emerged later. For example, Fang *et al.* investigated engineering the frequency response in an acoustic waveguide at ultrasonic frequencies with an array of sub-wavelength Helmholtz resonators to generate negative effective dynamic moduli near the resonance of system [15].

In addition to acoustic metamaterials that display either effective negative mass or effective negative stiffness, it has also been shown that it is possible

to generate both negative properties simultaneously. A prime example is the acoustic split ring resonators proposed in direct analogy to the electromagnetic split ring resonators that were at the forefront of electromagnetic metamaterial research [28, 29]. Acoustic metamaterials with both negative stiffness and negative mass density can be used for sound focusing and confinement and offer the possibility to create a superlens that can exceed the diffraction limit to achieve sub-wavelength resolution imaging [30].

1.3.1.2 Damping Due to Structural Negative Stiffness

Vibrations in mechanical systems are often undesirable because they can adversely affect people and the performance of sensitive equipment. Therefore, engineers are often concerned with the ability of a system to isolate and dissipate unwanted mechanical energy. Lakes and co-workers have extensively investigated composites [31, 32] and column dampers [33, 34] that take advantage of structural negative stiffness, concluding that the presence of negative stiffness enhances both the overall static stiffness and mechanical damping. As a simple example, Lakes showed that buckled silicone rubber tubes demonstrated greatly enhanced damping capacity as compared to identical silicone rubber tubes in an unbuckled configuration [35]. Experiments with multi-walled carbon nanotubes lead to the same conclusion of increased damping due to the presence of buckling as compared to unbuckled carbon nanotubes [36]. Those initial results lead to studies of heterogeneous materials containing domains of negative stiffness that suggested the possibility of creating a stiff

composite material with enhanced damping to overcome the trade-off between stiffness and loss found in conventional materials. It is important to note, however, that there may be caveats to those early works on structural negative stiffness. Stability analysis of composites with a negative stiffness phase indicate that it may be possible to obtain unusually large magnitudes for the effective dynamic stiffness, but not for the overall static stiffness [24, 37].

1.3.2 Nonlinear Systems

Nonlinear systems are studied for several reasons. One may be to improve upon a linear theory that does not adequately describe the system at hand for large disturbances. Another motivation may be to achieve some response that cannot be realized with a linear material. Examples of the latter appear in the present section with nonlinear systems applied to vibration isolation and nonlinear wave manipulation applications.

1.3.2.1 Vibration Isolation

Systems with negative stiffness or zero stiffness have been shown to improve both the shock isolation and vibration isolation capabilities of a system [38]. In addition to negative stiffness, nonlinear systems with "quasi-zero-stiffness" (QZS) are widely studied within the field of vibration isolation because decreasing the stiffness makes the system more capable of isolating against low frequency vibrations [39]. Systems with quasi-zero-stiffness can be created through different combinations of negative and positive stiffness

springs [38, 39]. Employing negative or zero linear stiffness for vibration isolation dates back to the mid twentieth century when Molyneux proposed zero stiffness as a means of isolating from mechanical vibrations in 1957, acknowledging the existence of an unstable, negative stiffness regime [40]. In the late 1970's, a guiding mechanisms was designed with negative stiffness springs to alleviate unwanted movement within the system [41]. Other designs relying upon springs with an effective negative stiffness to absorb vibrations appeared in the 1990's and were applied specifically to isolation tables to protect sensitive equipment against sub-Hertz vibrations [42, 43]. More recent examples of suspension systems for vibration isolation include applications for vehicles [44] and railroads [45].

Similarly, vibration isolation of a linear vibrating system can be achieved by coupling it to a strongly nonlinear component. The nonlinear attachment, termed a nonlinear energy sink (NES), is basically a nonlinear version of a linear tuned mass damper that absorbs the dynamic vibrations at certain frequencies. The mechanism is designed to facilitate efficient transfer of energy from the linear system that one wishes to isolate from vibrations to the nonlinear element. The energy within the NES is distributed from the primary mode in the linear component to higher order modes present in the nonlinear attachment, which are subsequently dissipated rapidly through mechanical losses. Quinn and co-workers recently studied several NES attachments that employed springs with cubic nonlinearity and zero linear stiffness, such that the force-displacement response is given simply by $F = k_{\text{NL}}x^3$. The character-

istic of zero linear stiffness is termed an "essential nonlinearity". The cubically nonlinear springs greatly accelerated the dissipation of vibrational energy of the system in comparison to a system with only linear components [46]. NESs with nonlinear attachments that contain both a cubic stiffness term and a negative linear stiffness have studied more recently. The presence of the negative linear stiffness in the nonlinear component more efficiently dissipated energy in comparison to the NESs that possessed the essentially nonlinearity [47].

1.3.2.2 Nonlinear Wave Manipulation

It is also possible to alter properties of the band gap using nonlinear periodic systems. Therefore, this section highlights research that is analogous to the work presented in Section 1.3.1.1. The nonlinear dispersion relation for periodic strings [48] and chains of nonlinear oscillators [49] have been studied in an attempt to understand the effects nonlinearity have on the band gap. Further, periodic systems made of elastomers that undergo nonlinear deformations have also been designed to alter the features of band gaps as a function of an imposed deformation for different loading conditions [13, 50]. These acoustic metamaterials may find applications as phononic switches because the properties of the medium change due to some external force, but are reversible and repeatable [51]. Another related nonlinear material that has been suggested as a nonlinear acoustic metamaterial is a granular crystal, which is a compact chain of elastic particles. The response of the granular crystals can be tuned depending on the material properties, geometry, and applied static

force, making them applicable to acoustic switches and one-way energy flow devices [14]. Further examples of devices used for non-reciprocal energy flow have been created using a superlattice, comprised of two alternating linear media, attached to a strongly nonlinear medium, such as a suspension of microbubbles [5, 52]. The development of a one way energy flow device may be beneficial for biomedical ultrasound, energy harvesting, and non-destructive testing [5, 14].

1.4 Objective

This thesis presents an exploration and detailed analysis of the nonlinear behavior of one type of acoustic metamaterial inclusions, called a snapping acoustic metamaterial (SAMM). The SAMM inclusions of interest exhibit non-monotonic stress-strain behavior, which displays regimes of both positive and negative stiffness, giving rise to a hysteretic snapping due to the presence of cubic nonlinearities. The nonlinear constitutive behavior can be tuned depending on the physical and geometrical properties of the microstructure. Some background on the behavior of the specific element exists [21], but not with respect to the nonlinear acoustic or dynamic response. The overall intent of the present research is to characterize the quadratic and cubic acoustic nonlinearities of a SAMM inclusion when embedded in a continuous constraining material and to understand the nonlinear dynamics of the elements in an effort to quantify the stiffness and damping capacity. Although understanding the nonlinear acoustic and dynamic behavior is of interest for the SAMM inclu-

sion scale, it is also worthwhile to investigate the overall macroscopic response associated with a heterogeneous material comprised of a low volume fraction of the SAMM inclusions embedded in a nearly incompressible matrix material. Therefore, the objective of the present research is to develop a tool to understand the influence of the unique nonlinear behavior exhibited by the SAMM inclusions in an effort to design a composite with nonlinear macroscopic properties, which can be tuned using the microscale geometry to elicit the desired macroscopic response. The present focus is on the effort to begin understanding the behavior on both the microscale and macroscale from the standpoint of nonlinear acoustics by introducing physical models of sufficient complexity to capture the details of the multiscale phenomena leading to the unconventional material response.

1.5 Thesis Overview

This thesis is organized into three main chapters, all of which employ the response of the same representative SAMM inclusion inspired by the work of Klatt and Haberman [21]. Chapter 2 describes the SAMM inclusion and provides additional background useful to understand its nonlinear constitutive relationship. The constitutive behavior characterizing a representative SAMM inclusion is then examined through an overall pressure-strain relationship and local stiffness coefficients that vary as a function of an imposed pre-strain. The later chapters use the information from Chapter 2 to study two different nonlinear responses for the SAMM inclusion and a heterogeneous

material comprised of a small volume fraction of SAMM inclusions embedded in a nearly incompressible viscoelastic matrix. Characterizing the matrix as a nearly incompressible elastic solid, which corresponds to a Poisson's ratio near 0.5, is valid due to the quasi-static, long wavelength limit approximations in the models presented. This requires the radius of the SAMM inclusion, R_{I}, to be much smaller than the characteristic wavelength of the matrix material, such that $k_{\text{M}}R_{\text{I}} \ll 1$, where k_{M} is the acoustic wavenumber.

Chapter 3 explores the acoustic nonlinearity associated with a heterogeneous medium comprised of the SAMM inclusions embedded in a nearly incompressible elastic matrix. As a precursor to understanding the acoustic nonlinearity associated with the SAMM inclusions, several state equations are presented as a standard means of describing the nonlinearities of a fluid or solid in acoustics. Some examples of the acoustic nonlinearity found in the literature are presented for reasons of comparison. The nonlinearity parameters are then used to describe the SAMM inclusion and the matrix. In order to describe the nonlinearity of the effective medium, two quasi-static homogenization techniques are presented. The first focuses on obtaining effective nonlinearity parameters from the law for immiscible mixtures. However, this technique limits the analysis to a matrix with zero shear modulus. To account for shear stresses, typical homogenization methods from linear elasticity are extended to accommodate finite deformations and thus obtain effective nonlinear elastic parameters. The technique used in this work follows from the Hashin-Shtrikman bounds derived in linear elasticity and the moduli obtained

are related to the acoustic nonlinearity parameters. The overall macroscopic response of the representative element is then compared with conventional materials. The remainder of Chapter 3 focuses on modeling a propagating acoustic wave through the effective medium, which requires augmenting standard techniques used to describe nonlinear distortion of a time-harmonic plane wave to include both quadratic and cubic nonlinearity. Examples of distorted acoustic waveforms are presented to demonstrate how the presence of the SAMM inclusions affect the behavior of an acoustic wave.

The other interest, presented in Chapter 4, studies the large deformation dynamical behavior associated with the SAMM inclusion when embedded in a nearly incompressible viscoelastic matrix material. A nonlinear differential equation used to model the nonlinear oscillations of a bubble, called the Rayleigh-Plesset equation, has been adapted and modified to incorporate the behavior of the SAMM inclusion. A decoupled system that models the microscale and macroscale independently is presented. The dynamics of a single SAMM inclusion embedded in a nearly incompressible medium and the heterogeneous material containing the SAMM inclusion surrounded by the same matrix are solved in parallel. The intent is to capture the hysteretic snapping due to large deformations and provide a qualitative understanding of the damping associated with the effective medium.

The thesis is concluded with Chapter 5, which summarizes the work detailed in Chapters 2–4. Although the research presented here provides considerable detail about the nonlinear behavior associated with the SAMM in-

clusions, there is still more to be understood and some suggestions for future work is also highlighted.

Chapter 2

Governing Behavior of Snapping Acoustic Metamaterial Inclusions

The present research focuses on snapping acoustic metamaterial (SAMM) inclusions with large nonlinearities generated physically on the inclusion scale due to negative stiffness. One means of attaining the behavior of interest is through a sub-wavelength structure, designed specifically such that the geometrical features induce the desired negative stiffness response. Therefore, this negative stiffness is a structurally induced effect, as opposed to being a resonance dependent response.

The element in Fig. 2.1 is the SAMM inclusion of interest for the present research. The computational models presented in Section 2.3 and throughout Chapters 3 and 4 utilize data obtained from a plane strain, finite element model (FEM) reported by Klatt, and the diagram is obtained directly from the FEM [21, 53]. The foundation for the inclusion design comes from the field of microelectromechanical systems (MEMs), where the fabrication of tunable, bistable, buckled beams was investigated for use in devices such as relays or optical witches [54]. The influence from MEMs appears in the double beam element shown in Fig. 2.1. This component is the source of the buckling

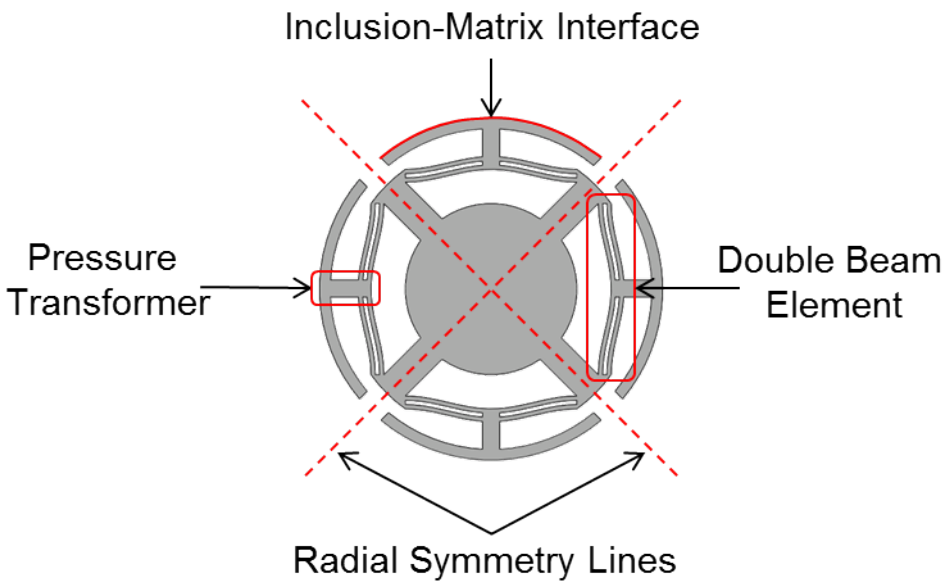

Figure 2.1: Diagram of the SAMM inclusion of interest.

instabilities that induce a snapping response. The instabilities are considered for an SAMM inclusion embedded within a surrounding elastic material, and the interface between the inclusion and matrix is clearly delineated in Fig. 2.1. The pressure imposed on the entire inclusion-matrix interface, either due to the matrix or some other external force, is localized at the pressure transformer. The concentrated force on the midpoint of each double element beam incites a mechanical response that is responsible for the snapping behavior under certain loading conditions. If the pressure incident upon the beam is not restricted to the center of the beam by the pressure transformer, the desired negative stiffness behavior may be significantly diminished or even eliminated due to the inclusions inability to snap-through.

The red dashed lines in Fig. 2.1 denote the symmetry axes for the inclusion and indicate that the element is spherically symmetric. Further, the SAMM inclusion is assumed to be much smaller than the acoustic wavelength, both with respect to the matrix it is embedded in and the effective medium that contains several SAMM inclusions. Therefore, the SAMM inclusion shown in Fig. 2.1 is modeled as a sphere.

The response from the FEM is easily scaled depending on the physical material that makes up the SAMM inclusion, as well as the curvature of the double beam component, corresponding to the ability to tune the structural instabilities to elicit a desired mechanical response. For additional details regarding the physical design and modeling of the SAMM inclusions, the reader is referred to Refs. [21] and [53].

2.1 Nonlinear Stiffness

The intent here is to characterize the linear and nonlinear stiffness of the SAMM inclusion in order to understand its constitutive behavior when acted upon by an external force. While the linear response of a material is fairly well understood, nonlinear behavior, which is the primary focus of the present work, is far more complicated. In order to provide a theoretical foundation for the study of the acoustic metamaterials of interest, it is worthwhile to provide a thorough understanding of the nonlinear behavior as related to nonlinear oscillators and nonlinear stress-strain response of hyper-elastic materials.

2.1.1 Nonlinear Springs

Mechanical systems are modeled using masses, springs and dampers. In many cases, one is only concerned with the dynamic response for small amplitude oscillations. In those cases, it is reasonable to model the system as a linearly oscillating system. However, for systems subjected to large amplitude vibrations or for those comprised of components with a very strong nonlinear response, a nonlinear oscillator more accurately describes the response. When the nonlinear component is the spring element, the reaction force generated as a result of an imposed displacement from its equilibrium position can be represented with a Taylor series expansion. The expansion is commonly considered up to third order with respect to position x, such that [55]

$$F = k_1 x + k_2 x^2 + k_3 x^3, \tag{2.1}$$

where the equilibrium position is assumed to be the $x_0 = 0$ position and k_i represent the linear and nonlinear stiffness terms. The second order term, k_2, is often assumed to be negligible.

The spring force as a function of an imposed displacement is shown in Fig. 2.2 for three spring types—a linear spring, a nonlinear hardening spring and a nonlinear softening spring. These three springs are of interest because they represent the canonical types of material responses that are commonly studied. The linear spring is plotted in blue and as expected, shows a straight line with constant slope over the entire range of displacements. The nonlinear hardening spring, modeled with $k_3 > 0$, is shown by the green curve and refers

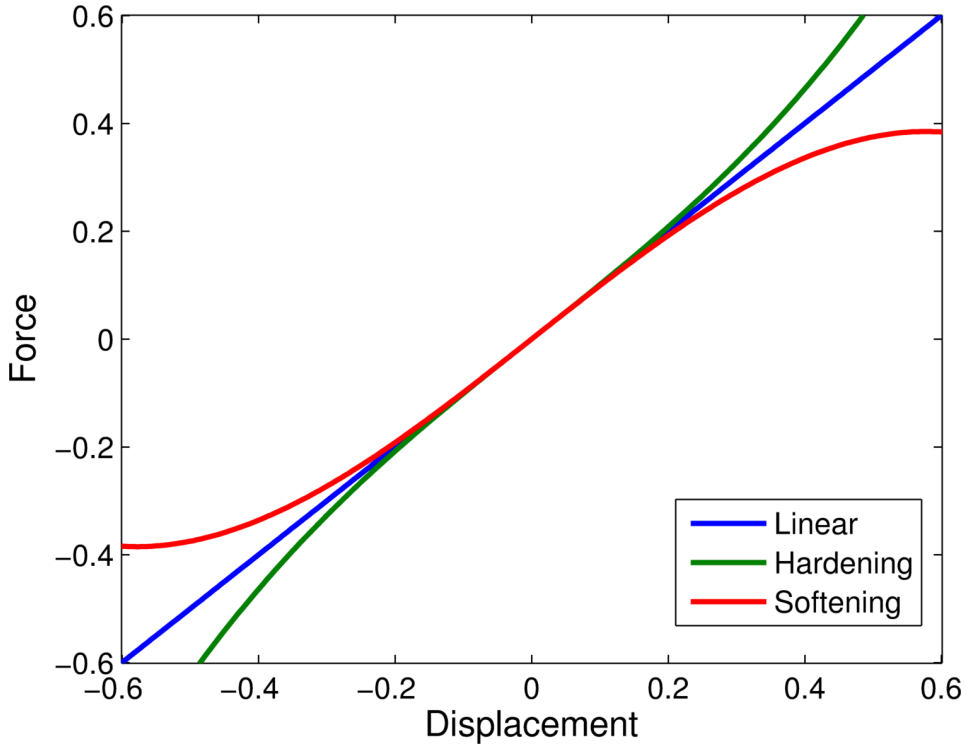

Figure 2.2: Force versus displacement for linear, hardening and softening springs.

to an increasing force for a given displacement increment as the displacement from the origin increases. The nonlinear softening spring, modeled with $k_3 < 0$, is given by the red curve and behaves conversely to the hardening spring. As the curve indicates, a softening spring is characterized by offering decreasing force per displacement increment as the overall displacement from the origin is increased [56].

The relatively simple nonlinear force-displacement constitutive relationships induces behavior such as the jump phenomena for a single degree of freedom mass-spring-damper system. Jump phenomena occur on frequency

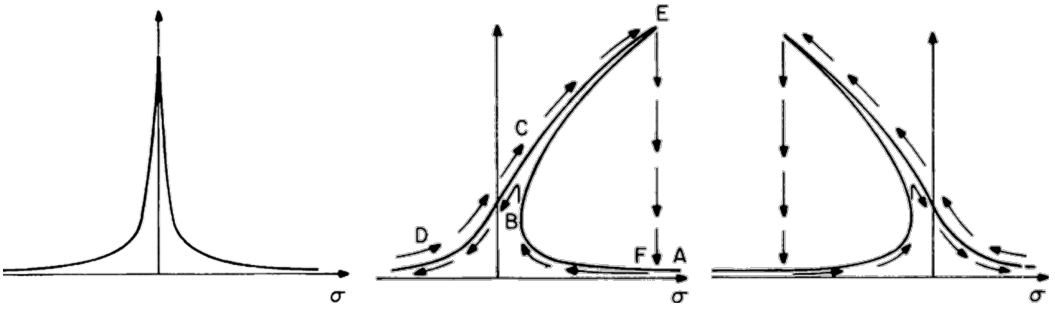

(a) Linear Spring (b) Hardening Spring (c) Softening Spring

Figure 2.3: Amplitude versus frequency for (a) linear spring, (b) hardening spring and (c) softening spring adapted from Ref. [56].

response curves that are multivalued at frequencies near the small-amplitude resonance frequency of the system. Such a response is exemplified in Fig. 2.3 adapted from Figure 1-5 in Ref. [56]. The amplitude versus frequency response for the linear spring, shown in Fig. 2.3(a), is single-valued with the peak centered at resonance. Figure 2.3(b) presents the hardening spring, with letters and arrows delineating the path on the multivalued amplitude-frequency response curve. Starting at point A, the response follows the curve for decreasing frequency to point B, and then jumps to the amplitude at point C on the upper half of the curve instead of following the bottom half of the to point E. The amplitude then follows the upper curve for decreasing frequency. Starting now at point D, the amplitude response as frequency increases follows the upper curve to point E and then jumps down to point F on the lower curve. The softening spring exhibits a similar response but in the opposite direction, as shown in Fig. 2.3(c) with the marked arrows.

The behavior shown in Fig. 2.3 corresponds to that of a Duffing os-

cillator, which is one of the most widely studied systems within the field of nonlinear dynamics. The third order constitutive response, such as the one given in Eq. (2.1), corresponds to a fourth order potential energy function. The ordinary differential equation used to describe forced oscillations of this system was first studied by Georg Duffing in the early twentieth century in order to understand the hardening spring response associated with some mechanical systems and is known as Duffing's equation [57]. The Duffing oscillator has since been the subject of a significant amount of theoretical and experimental studies, including a thorough introduction by Virgin as an illustrative example of principles associated with nonlinear vibrations [58]. Many of these studies involve a fourth order potential energy function with potential wells, characterized by local minimas, and focus on the motion within or between the potential wells. The SAMM inclusions of interest here exhibit similar behavior, which is briefly introduced in this chapter, with more information found in [21, 53]. The nonlinear dynamic response is considered in detail in Chapter 4.

2.1.2 Nonlinear Stress-Strain Response

Understanding the nonlinear stress-strain relationship is of fundamental importance for analyzing the structures of interest in this thesis. The nonlinear stress-strain behavior is analogous to the force-displacement response of nonlinear springs. Metrics of stiffness, however, are difficult to quantify when operating outside the limit of linear elasticity. For example, when a

material is subjected to large deformations, the subsequent response could be inelastic, where the strain energy when loading the system differs from unloading. Inelastic behavior occurs with pseudo-elasticity, e.g. stress softening, and plasticity, which induces an irreversible deformation [59]. While the overall response is not elastic in either case, elasticity theory, to an extent, can approximately describe the incremental deformation relative to the current configuration or strain state. Examples of such hyper-elastic material models are Neo-Hookean, Mooney-Rivlin [60], Varga and modified Varga [61] materials. One method of more accurately analyzing the deformation utilizes a strain energy approach, where local estimates of nonlinear stiffness characterize the deformation. Strain energy models are applied to the inclusions of interest in Section 2.2.

As a simple illustrative example, consider the nonlinear stress-strain constitutive relation depicted by the solid black curve in Fig. 2.4. The response is similar to that of a softening spring shown in Fig. 2.2. The linear regime of the constitutive curve in Fig. 2.4, approximately indicated by the response within the green box, corresponds to a straight line about a reference configuration of zero stress and zero strain. Stiffness is defined as the first derivative of stress with respect to strain [62]. In Fig. 2.4, the stiffness is therefore represented by the slope of the stress-strain curve, as denoted by the blue dashed line. Within the green box, the blue dashed line and the solid black curve predict nearly the same stress value for a given strain, indicating this section of the overall nonlinear response is well represented with a linear rela-

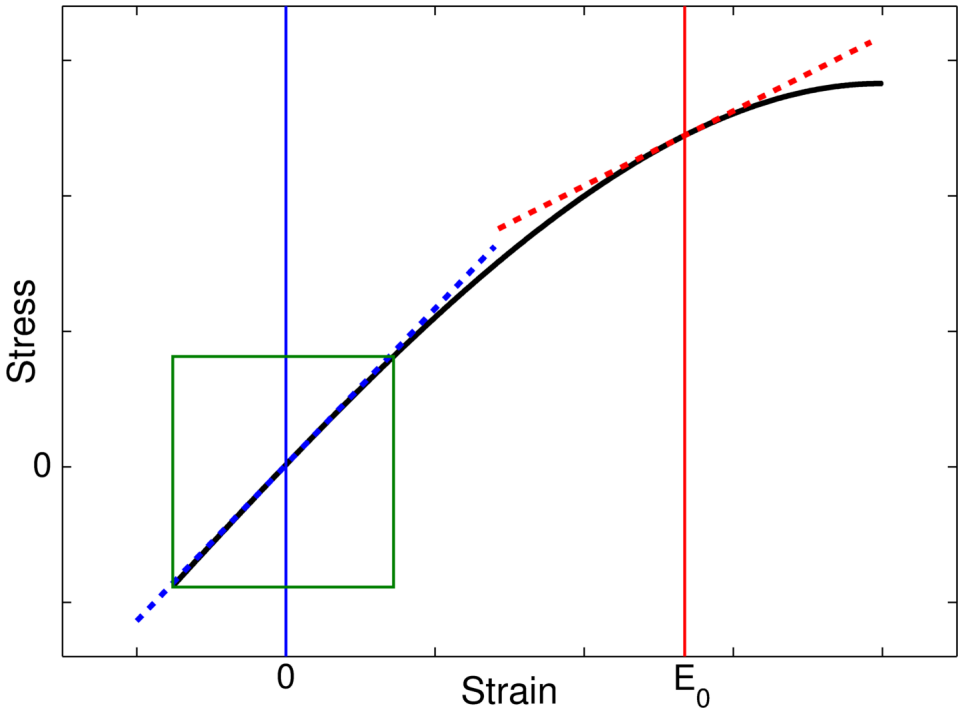

Figure 2.4: Example nonlinear stress-strain constitutive curve.

tionship between stress and strain. The blue dashed line diverges significantly from the black curve when outside the green box, indicating that the slope is a nonlinear function of strain, and the linear stiffness approximation within the green box is no longer valid outside of the box. This is clearly illustrated when one considers the red dashed line. The red dashed line is only tangent to a small portion of the black curve, centered about the vertical solid red line at E_0, and is less steep than the blue dashed line that corresponds to the linear regime centered at the zero strain configuration. The simple example illustrates that parameters used to describe the stiffness of a nonlinear elastic material are only valid within finite segments of the constitutive curve. To

more accurately model the response of the material around a give strain point, one can employ higher order, nonlinear terms with values that vary depending on the strain state. The strain dependent material stiffness parameters, both linear and nonlinear, are referred to in the present work as local stiffness parameters or local linear and nonlinear stiffness moduli. Describing an entire curve using local approximations is essentially a Taylor series expansion evaluated at the pre-strain, E_0, such that

$$\sigma - \sigma_0 = (E - E_0) \left.\frac{\partial \sigma}{\partial E}\right|_{E_0} + \frac{1}{2} (E - E_0)^2 \left.\frac{\partial^2 \sigma}{\partial E^2}\right|_{E_0} + \cdots , \tag{2.2}$$

where σ_0 is the stress evaluated at E_0. If the response corresponds only to the linear component of the black curve in Fig. 2.4, then the first term on the right hand side of Eq. (2.2) is sufficient to describe the behavior. The slope, as given by $\partial\sigma/\partial E$ evaluated at E_0, is effectively constant for all E_0 within the linear range and the higher order terms in Eq. (2.2) are negligible. As the constitutive relationship becomes more nonlinear, the higher order derivatives of stress with respect to strain must be accounted for. This is the underlying principle of the perturbation theory utilized in throughout the present work.

It is worth clarifying the concept of 'global' and 'local' parameters to describe an entire constitutive stress-strain response curve. In the present thesis, global parameters utilize one function and one set of parameters to uniquely define the entire behavior. The local description, on the other hand, are functions of another variable, such as strain [63]. Within the field of nonlinear elasticity, it is often unlikely that global parameters will correctly

characterize the entire constitutive stress-strain relationship. Instead, a global approximation is likely to diverge from the actual material response for increasingly nonlinear material behavior. For the example curve in Fig. 2.4, the nonlinearity associated with the change in curvature as the strain increases is most accurately described by local coefficients instead of global parameters.

2.2 Constitutive Relationship

In the present work, the strain energy density used to describe the nonlinear behavior of the SAMM inclusions is a fourth order power law expansion in strain, such that [62]

$$\begin{aligned}\mathscr{E} = \mathscr{E}_0 + B_{ij}E_{ij} + \frac{1}{2!}C_{ijkl}E_{ij}E_{kl} + \frac{1}{3!}D_{ijklmn}E_{ij}E_{kl}E_{mn} \\ + \frac{1}{4!}M_{ijklmnop}E_{ij}E_{kl}E_{mn}E_{op},\end{aligned} \tag{2.3}$$

where B_{ij}, C_{ijkl}, D_{ijklmn}, and $M_{ijklmnop}$ are components of the elastic stiffness tensors that describe the SAMM inclusion, E_{ij} are components of the strain tensor and $\mathscr{E}_0$ is the strain energy density of the undeformed state. The Cauchy stress corresponding to the deformation is found from the relation [62]

$$\sigma_{ij} = \frac{\partial \mathscr{E}}{\partial E_{ij}}. \tag{2.4}$$

Therefore, the stress tensor is

$$\sigma_{ij} = B_{ij} + C_{ijkl}E_{kl} + \frac{1}{2}D_{ijklmn}E_{kl}E_{mn} + \frac{1}{6}M_{ijklmnop}E_{kl}E_{mn}E_{op}. \tag{2.5}$$

From an acoustics standpoint, the pressure, not the stress, is of interest. The two are related by [62]

$$P = -\frac{1}{3}\sigma_{ii}. \tag{2.6}$$

From Eqs. (2.5) and (2.6), pressure, as a function of strain and the stiffness tensors, is

$$P = -\frac{1}{3}\left(B_{ii} + C_{iikl}E_{kl} + \frac{1}{2}D_{iiklmn}E_{kl}E_{mn} + \frac{1}{6}M_{iiklmnop}E_{kl}E_{mn}E_{op}\right) \tag{2.7}$$

The inclusion considered in the present work is assumed to be a sphere undergoing spherically symmetric deformation, where the radial displacement is given by [64]

$$u_r = a_{\text{I}} r, \tag{2.8}$$

with a_{I} being a constant that characterizes the deformation and r representing the distance from the origin, or radial coordinate, in the Lagrangian reference frame. In general, the Lagrangian strain tensor is related to the displacement field, u_i, through the relation

$$E_{ij} = \frac{1}{2}\left(u_{i,j} + u_{j,i} + u_{k,i}u_{k,j}\right), \tag{2.9}$$

where the index notation $u_{i,j}$ denotes the partial derivative of u_i with respect to x_j. The components of the strain tensor for the spherical SAMM inclusion is obtained from Eqs. (2.8) and (2.9), such that

$$E_{ij} = \left(a_{\text{I}} + \frac{3}{2}a_{\text{I}}^2\right)\delta_{ij}, \tag{2.10}$$

where δ_{ij} is the Kronecker delta, defined as

$$\delta_{ij} = \begin{cases} 1 \text{ if } i = j \\ 0 \text{ if } i \neq j \end{cases} . \tag{2.11}$$

Equation (2.8) describes locally a pure dilation of the inclusion [64]. The strain in Eq. (2.10) can therefore be expressed in terms of volumetric strain, or dilatation, denoted by ε_v. Volumetric strain is defined as change in volume, v, normalized by the equilibrium volume, V_0. The change in volume is the difference between the instantaneous volume, V, and the equilibrium volume, such that the volumetric strain is $\varepsilon_v = (V - V_0)/V_0$. Since the SAMM inclusion is modeled as a sphere, the volumetric strain depends on the instantaneous radius, R_{I} and the equilibrium radius R_{I_0},

$$\varepsilon_{v\text{I}} = \left(\frac{R_{\text{I}}}{R_{\text{I}_0}} \right)^3 - 1. \tag{2.12}$$

The equilibrium radius corresponds to a deformation-free configuration with no external forces imposed upon the system. The volumetric strain is simply related to the Lagrangian strain tensor, such that

$$\varepsilon_{v\text{I}} = E_{kk} = 3a_{\text{I}} + \frac{9}{2}a_{\text{I}}^2. \tag{2.13}$$

Therefore, $E_{ij} = \frac{1}{3}\varepsilon_{v\text{I}}\delta_{ij}$, and the expression for the pressure of the inclusion in Eq. (2.7) can be expressed as

$$\begin{aligned} P_{\text{I}} = &-\frac{1}{3}B_{ii} - \frac{1}{9}C_{iikl}\delta_{kl}\varepsilon_{v\text{I}} - \frac{1}{54}D_{iiklmn}\delta_{kl}\delta_{mn}\varepsilon_{v\text{I}}^2 \\ &- \frac{1}{486}M_{iiklmnop}\delta_{kl}\delta_{mn}\delta_{op}\varepsilon_{v\text{I}}^3, \end{aligned} \tag{2.14}$$

where the subscript I denotes that the variables refer to the inclusion. The first term in Eq. (2.14), $\frac{1}{3}B_{ii}$, corresponds to a pre-pressurization due to an external force imposed on the system when the strain in the reference configuration is zero. For the purpose of the present thesis, this term is considered to be the equilibrium hydrostatic pressure, defined as

$$P_{\text{I}_0} = -\frac{1}{3}B_{ii}. \tag{2.15}$$

The subscript 0 indicates that Eq. (2.15) refers to an equilibrium term. However, the pre-stress could be induced by other means, such as thermal or piezoelectric. The second term in Eq. (2.14) corresponds to linear elasticity. In the limit for a linear, isotropic, elastic solid, the stiffness tensor can be expressed as a function of the bulk modulus, K, and the shear modulus, μ, such that

$$C_{ijkl} = K\delta_{ij}\delta_{kl} + \frac{1}{3}\mu\left(3\delta_{ik}\delta_{jl} + 3\delta_{il}\delta_{jk} - 2\delta_{ij}\delta_{kl}\right). \tag{2.16}$$

From Eq. (2.16) and the properties of the Kronecker delta,

$$\frac{1}{9}C_{iijk}\delta_{jk} = K_{\text{I}}. \tag{2.17}$$

The quantity, K_{I}, is the bulk modulus of the SAMM inclusion. The third terms in Eq. (2.7) characterizes the second order stiffness, which is nonlinear. This term could be expressed as a function of the Landau coefficients [65], however, that is unnecessary for the purpose of the present work. Instead a nonlinear, second order stiffness modulus, K'_{I}, is defined as linear combinations of the higher order elastic terms, such that

$$K'_{\text{I}} = -\frac{1}{27}D_{iiklmn}\delta_{kl}\delta_{mn}. \tag{2.18}$$

Similarly, a nonlinear, third order stiffness modulus, K_{I}'', is defined to characterize the last term in Eq. (2.7),

$$K_{\text{I}}'' = \frac{1}{81} M_{iiklmnop} \delta_{kl} \delta_{mn} \delta_{op}. \tag{2.19}$$

The expressions in Eq. (2.15)–(2.19) are combined to provide a simplified equation for pressure as a function of the state variable, $\varepsilon_{v\text{I}}$,

$$P = P_{\text{I}_0} - K_{\text{I}} \varepsilon_{v\text{I}} + \frac{1}{2} K_{\text{I}}' \varepsilon_{v\text{I}}^2 - \frac{1}{6} K_{\text{I}}'' \varepsilon_{v\text{I}}^3. \tag{2.20}$$

As previously stated, defining global nonlinear stiffness parameters may not correctly capture the behavior of a nonlinearly deforming body. Therefore, the coefficients, K_{I}, K_{I}', and K_{I}'', are effective elastic constants that vary locally depending on the hydrostatic pressure, P_{I_0}, applied to the SAMM inclusion. Their values are obtained by considering small perturbations about the imposed pre-strain. It is also worth noting that the relationship between the Lagrangian strain tensor and the volumetric strain is an infinitesimal strain theory definition that is not valid for arbitrary finite strains, even if they are spherically symmetric [62]. However, by considering only small perturbations, the use of volumetric strain in defining the constitutive relationship between pressure and strain provides a reasonable approximation of the nonlinear response of the SAMM inclusions. Future work may consider more accurate models for large deformations using finite elasticity.

The small perturbations are considered about some volumetric pre-strain, denoted by $\bar{\varepsilon}_{v\text{I}}$, imposed on the SAMM inclusion. The pre-strain has

the same form as Eq. (2.12), and is defined as

$$\bar{\varepsilon}_{v\mathrm{I}} = \left(\frac{R_{\mathrm{I}}}{\bar{R}_{\mathrm{I}}}\right)^3 - 1. \tag{2.21}$$

In Eq. (2.21), the strain corresponds to a new equilibrium radius, $\bar{R}_{\mathrm{I}}$, instead of R_{I_0}. The governing constitutive relationship for the inclusion pressure can then be written as a function of both $\varepsilon_{v\mathrm{I}}$ and $\bar{\varepsilon}_{v\mathrm{I}}$,

$$P_{\mathrm{I}} = P_{\mathrm{I}_0} - K_{\mathrm{I}}\left(\varepsilon_{v\mathrm{I}} - \bar{\varepsilon}_{v\mathrm{I}}\right) + \frac{1}{2}K'_{\mathrm{I}}\left(\varepsilon_{v\mathrm{I}} - \bar{\varepsilon}_{v\mathrm{I}}\right)^2 - \frac{1}{6}K''_{\mathrm{I}}\left(\varepsilon_{v\mathrm{I}} - \bar{\varepsilon}_{v\mathrm{I}}\right)^3. \tag{2.22}$$

The values of the coefficients, K_{I}, K'_{I}, and K''_{I}, change as the hydrostatic pressure, P_{I_0}, forces the SAMM inclusion to different equilibrium volumetric strains.

2.3 Representative SAMM Inclusion Response

The data obtained from FEM are the displacement from the initial radius and the resulting strain energy density in the SAMM inclusion. The output from an example inclusion geometry is shown in Fig. 2.5. The FEM is implemented with displacement boundary conditions. This implies that the analysis represents displacement controlled behavior where the SAMM inclusion is subjected to incremental displacement and the FEM provides the corresponding strain energy resulting from that imposed deformation. All the curves presented in Sections 2.3.1 and 2.3.2, as well as the remainder of this thesis, correspond to the same representative SAMM inclusion.

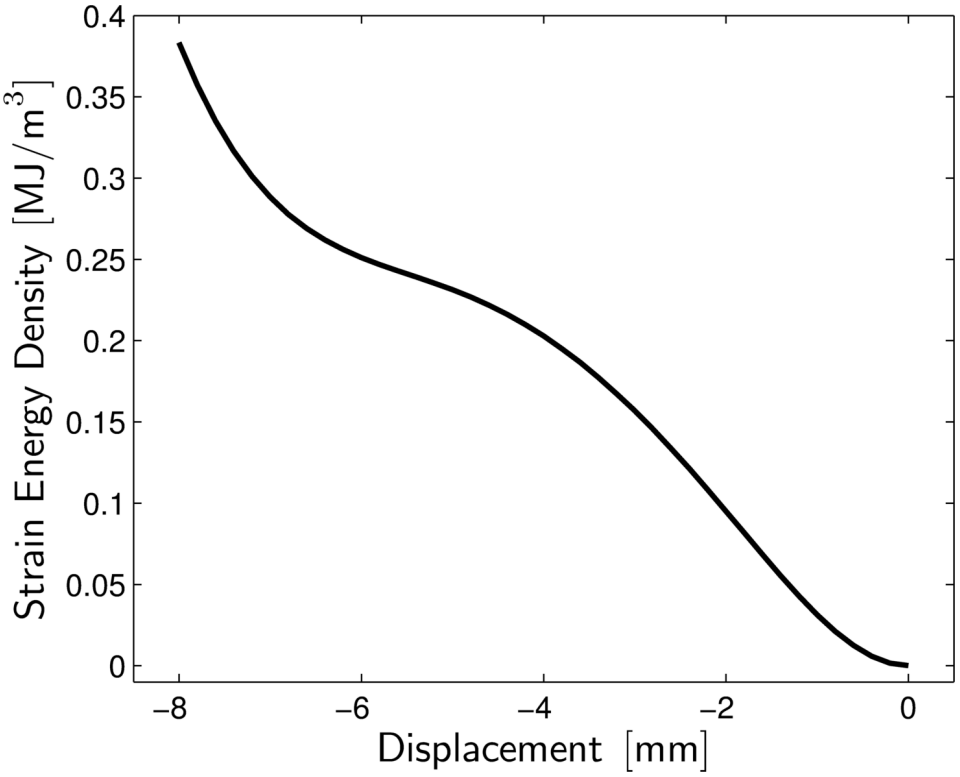

Figure 2.5: Fourth order strain energy density function versus displacement in mm for a single SAMM inclusion from FEM.

2.3.1 Overall Behavior

The strain energy density versus imposed displacement data has been transformed to pressure versus volumetric strain based on relationships in Section 2.2. The pressure in MPa is plotted as a function of the change in volume $V_{\text{I}} - V_{\text{I}0}$, normalized by the initial volume, $V_{\text{I}0}$, in Fig. 2.6. The negative values of $(V_{\text{I}} - V_{\text{I}0})/V_{\text{I}0}$ represent negative strain as the instantaneous volume, V_{I}, is smaller than the equilibrium volume. In the figure, the blue dots on the pressure-volumetric strain curve correspond to the diagrams with

the same letter located above and below the constitutive curve. Details regarding the loading condition are described below. The diagrams, which are obtained directly from the FEM, depict the deformed shape of the inclusion cross-section for various radial displacement values. Any perception that the inclusion components overlap is due to an exaggerated scaling of the deformation that allows the changes in the microstructure to be readily apparent. They are not from physical interference between the components. The strain magnitudes at different displacements from the equilibrium radius are reflected in the color gradient; minimum strain corresponds to the dark blue color and maximum strain is represented by dark red.

Since the FEM is displacement controlled, pressure is the dependent variable, allowing the subsequent pressure-volumetric strain curve to be non-monotonic. However, the loading conditions considered here are pressure, or stress, controlled. The volumetric strain is contingent upon the pressure response, which is now path dependent. The overall behavior of the SAMM inclusion follows the path delineated by the red arrows, instead of explicitly following the black curve.

Zero displacement, or zero strain, occurs at the position denoted by (a). The inclusion diagram is a solid, dark blue color. As the pressure increases, the inclusion deforms until it reaches the position denoted by (b). At this location, the inclusion is compressed more than in state (a) and the outer components therefore have a lighter blue color. An essential nonlinearity, where the linear stiffness is zero and only the nonlinear moduli characterize

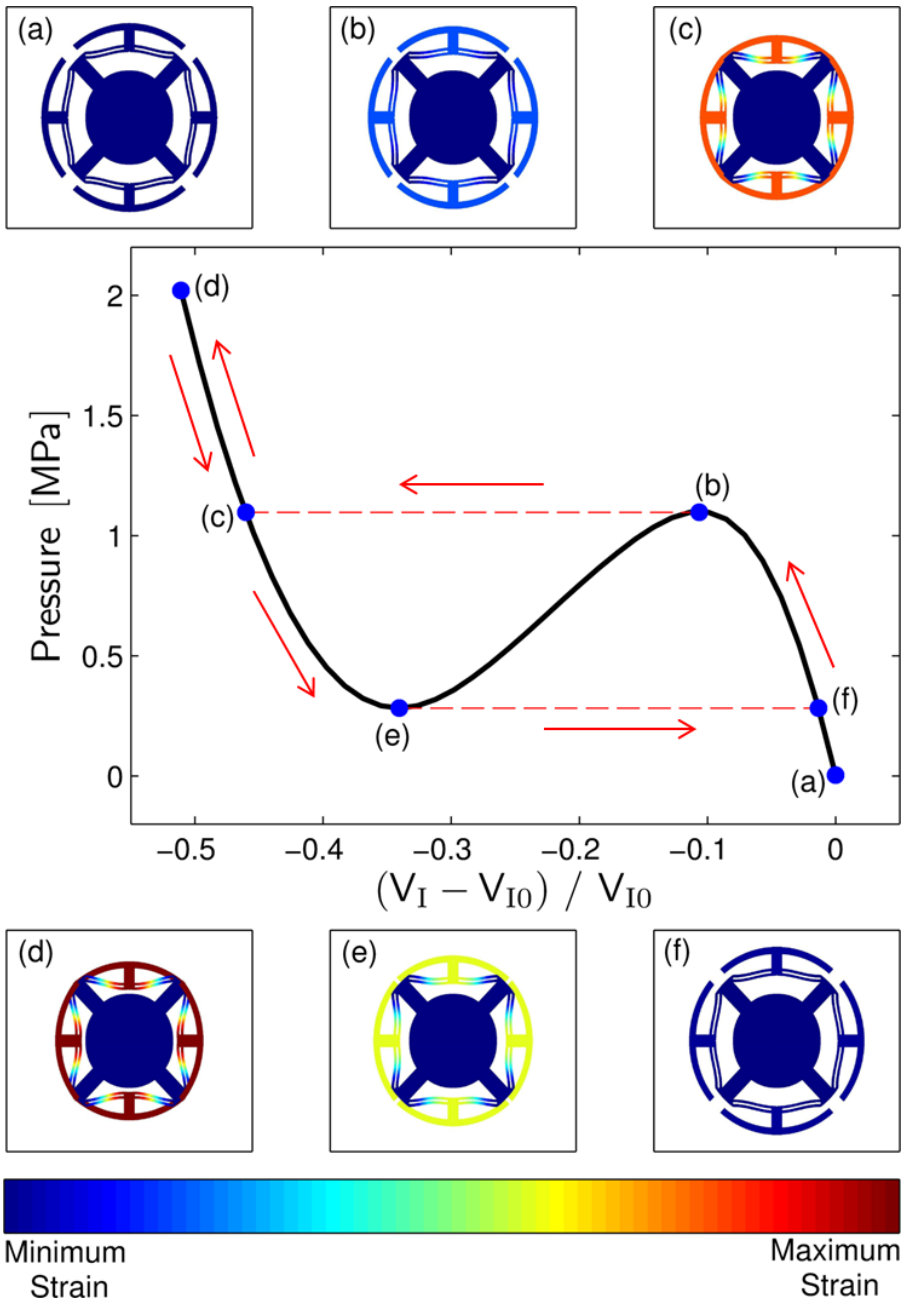

Figure 2.6: Pressure in MPa as a function of volume corresponding to six deformed states of SAMM inclusion that demonstrate the snapping response.

the response, occurs at position (b), also defined as a limit point [66]. When the inclusion is displaced to (b), any increase in pressure will require the inclusion to snap through to location (c), which has the same pressure magnitude but a much larger strain magnitude. At point (c), the inclusion is more compressed than in state (b) as indicated by the bright red color. As the SAMM inclusion is further deformed, it becomes continuously more compressed. At location (d), the inclusion is a dark red color, corresponding to the largest strain magnitude for this data.

A response similar to the behavior just described for loading the system occurs when unloading the system. Starting from state (d), a reduction in pressure allows the SAMM inclusion to expand along the pressure-volume curve until it reaches state (e), another limit point with an essential nonlinearity. The limit point at this position occurs for a lower pressure magnitude than the limit point at location (b). The microstructure at point (e) is now yellow. Once again, a small pressure decrement will force the SAMM inclusion to snap from position (e) to (f). The microstructure is now a dark blue color again, indicating that during unloading of the system, for the same pressure magnitude, the strain magnitudes are much smaller. The SAMM inclusion would then continue to expand back to state (a). Because the constitutive curve follows different paths when the system is loaded and unloaded, the path dependent behavior corresponds to an inelastic response that can be described locally using perturbation techniques of nonlinear elasticity for small-but-finite deformations about a given configuration.

The locally positive and negative stiffness regimes of the SAMM inclusion are readily apparent from Fig. 2.6. Since stiffness is the first derivative of stress with respect to strain, and pressure is negative stress, stiffness is proportional to the negative first derivative of pressure with respect to strain, $K \propto -\partial P/\partial \varepsilon_v$ [62]. For the displacement-controlled constitutive relationship depicted by the black curve in Fig. 2.6, the sections between points (a) and (b) and between (d) and (e) have a negative slope and thus correspond to positive stiffness, whereas the positive slope between points (b) and (e) is indicative of negative stiffness.

2.3.2 Local Coefficients

The hydrostatic pressure as a function of volumetric strain is shown in Fig. 2.7, and estimates of the effective elastic parameters, K_{I}, K'_{I} and K''_{I}, corresponding to P_{I_0} are shown in Figs. 2.8–2.10. The values are obtained by considering a pre-strain corresponding to the displacements shown in Fig. 2.5. The coefficients are then fitted to a fourth order strain energy density function for small perturbations about this pre-strain.

Figure 2.7 presents the hydrostatic pressure that will pre-strain the SAMM inclusions to these states. The constitutive relation shown in Fig. 2.6 is also plotted on Fig. 2.7 as the solid grey line. As expected, the two cubic non-monotonic curves are identical. This is because the coefficients are obtained through perturbation theory utilizing a Taylor series expansion. When evaluating the pressure response given by Eq. (2.22) at each pre-strain where

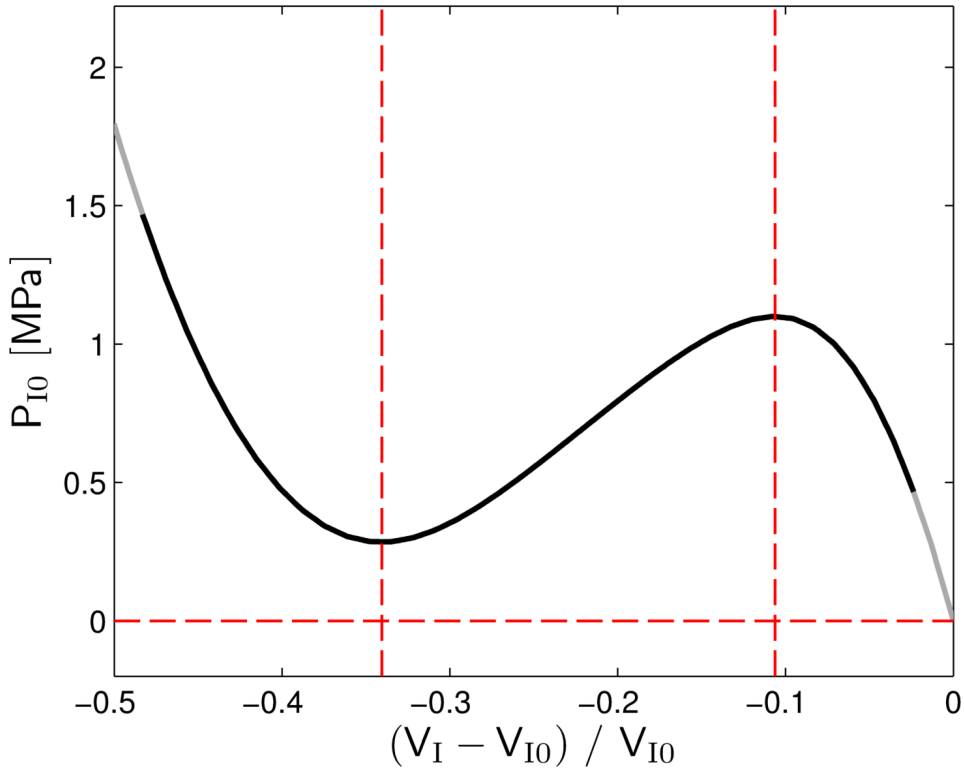

Figure 2.7: Hydrostatic pressure, P_{I_0}, for small perturbations about a volumetric pre-strain imposed on the SAMM incluison.

$\varepsilon_{v\mathrm{I}} = \bar{\varepsilon}_{v\mathrm{I}}$, $P_{\mathrm{I}} = P_{\mathrm{I}_0}$ must be true. The grey line extends to further volumetric strain magnitudes than the black curve because of how the coefficients are obtained. The fitting technique involves several data points on either side of the chosen pre-strain, and therefore, the hydrostatic pressure obtained from the fitting, as well as the coefficients presented in the following figures, encompasses a smaller range of volumetric strain values. Additionally, the vertical red dashed lines shown in Fig. 2.7 correspond to the limit points, positions (b) and (e) from Fig. 2.6, where the SAMM inclusion will snap through to a higher

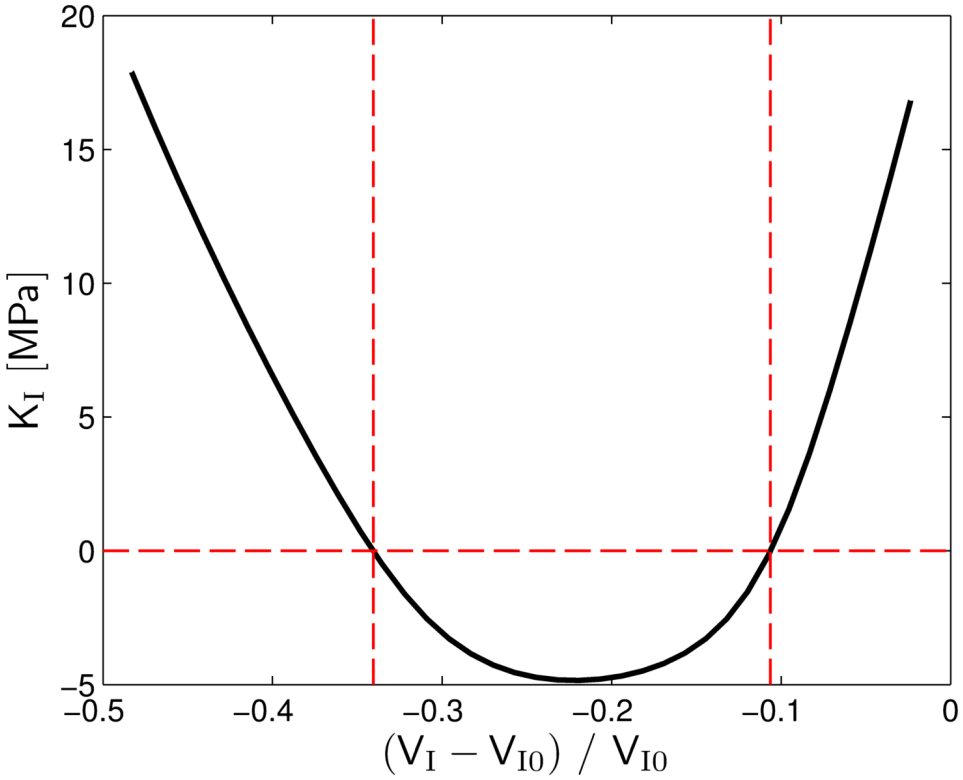

Figure 2.8: Local linear stiffness, K_{I}, for small perturbations about a volumetric pre-strain imposed on the SAMM inclusion.

or lower strain configuration, respectively, for the same imposed pressure as described in Section 2.3.1.

The local linear stiffness of the SAMM inclusion is attained for every volumetric pre-strain, as plotted in Fig. 2.8. The shape of the curve resembles that of a quadratic function. Because the linear bulk modulus is approximated as the negative first derivative of pressure, which is a cubic function, the quadratic shape is expected. It is not, however, a perfect quadratic, which will become more apparent with the higher order derivatives presented in Figs. 2.9

and 2.10. As the pre-strains move away from the essential nonlinearities within the positive stiffness regions of Fig. 2.8, K_{I} appears to follow fairly straight lines. These traits are attributed to how much curvature is present in the pressure curve shown in Fig. 2.7. Furthermore, the sign of K_{I} can either be positive or negative, which is the feature contributing to the high interest in the SAMM inclusions. As K_{I} transitions from the positive to negative region or vice versa, there exists a pre-strain with zero linear stiffness, or an essential nonlinearity. The essential nonlinearities occur at the intersection of the red dashed lines, explicitly delineating the locally positive and negative stiffness regimes.

Figure 2.9 shows the second order elastic modulus, K_{I}', as a function of the volumetric pre-strain. The curve is monotonic, spanning from negative to positive values as the magnitude of the volumetric strain increases. If the linear stiffness in Fig. 2.8 were a perfect quadratic function, then K_{I}' would show a straight line of constant slope. This is because the nonlinear, second order stiffness is approximated by taking the first derivative of K_{I} with respect to strain. Instead, there are finite, linear sections of K_{I}' connected to form the curve shown in Fig. 2.9. Because K_{I}' transitions from positive to negative, there exists a pre-strain where $K_{\text{I}} = 0$, which occurs within the negative linear stiffness regime.

Figure 2.10 shows the third order elastic modulus, K_{I}'', as a function of the volumetric pre-strain. The shape of the figure is less intuitive than that of the previous figures. Once again, if Fig. 2.8 depicted a perfect quadratic

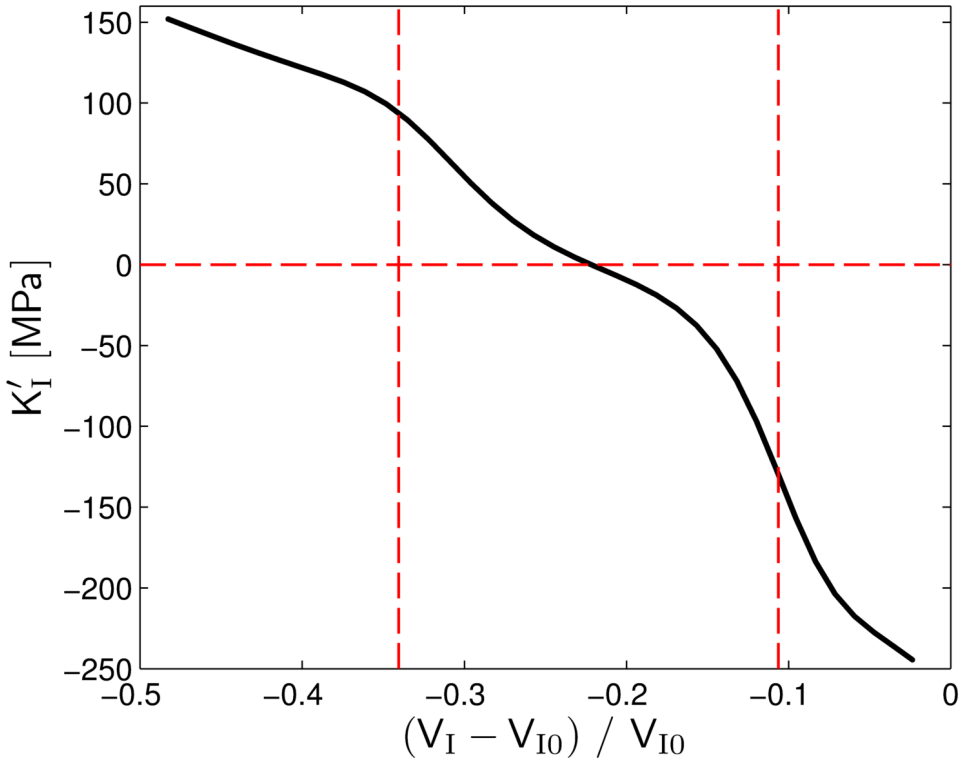

Figure 2.9: Local second order modulus, K_{I}', for small perturbations about a volumetric pre-strain imposed on the SAMM inclusion.

function, K_{I}'', which represents the negative first derivative of K_{I}' or the negative second derivative of K_{I}, would be constant. Although there are sections of Fig. 2.10 that are roughly constant horizontal lines, the magnitude of K_{I}'' fluctuates for different volumetric pre-strains. Figure 2.10 does, however, only reflect positive values of K_{I}'', due to the monotonic nature of K_{I}' in Fig. 2.9. Therefore, the nonlinear, third order stiffness modulus exists for every volumetric pre-strain. The strong nonlinearity will occur for any SAMM inclusion that obeys a quartic strain energy density function with potential wells, such

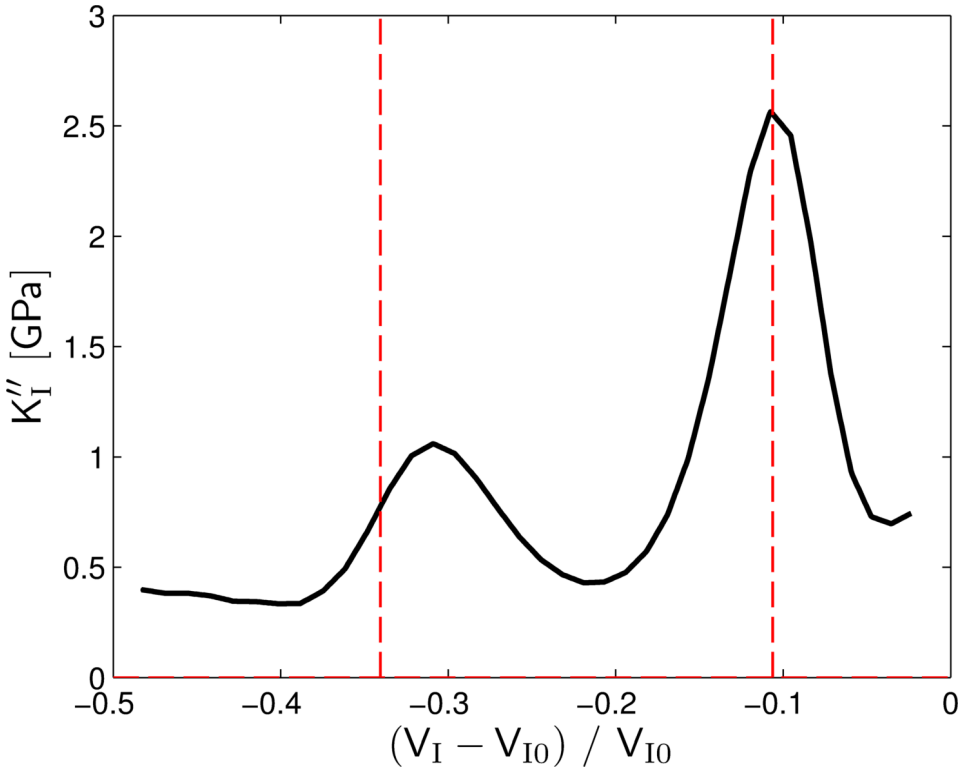

Figure 2.10: Local third order modulus, K_{I}'', for small perturbations about a volumetric pre-strain imposed on the SAMM inclusion.

as the one shown in Fig. 2.5.

The concept of relating the linear, quadratic, and cubic stiffness parameters through derivatives is routed in describing the system through a Taylor series expansion. For the representative SAMM element, this leads to K_{I}' being an order of magnitude larger than K_{I} and K_{I}'' reaching two orders of magnitudes larger K_{I}. Both Figs. 2.8 and 2.9 are presented in terms of MPa, while K_{I}'' is presented on the scale of GPa. The vertical red dashed lines indicating the pre-strains at zero linear stiffness in Fig. 2.8 are also present in both

Figs. 2.9 and 2.10. Although the presence of the red dashed lines does not offer any insight into the unique nonlinear behavior of the SAMM inclusions, the essential nonlinearities will be of particular interest in Chapter 3. Therefore, it is worth noting that at the essential nonlinearities, K_{I}' may assume either positive or negative values and that the magnitudes of both K_{I}' and K_{I}'' can vary. This will contribute to different macroscopic responses that are explored in detail in the following chapter.

2.4 Summary

Throughout the chapter, a fundamental understanding of the SAMM inclusions of interest are analyzed from the standpoint of nonlinear elasticity. This requires locally describing the deformation due to an imposed pressure through standard perturbation theory techniques involving Taylor series expansions. The data, originally obtained from an FEM approach, presents the response for one representative SAMM inclusion. All subsequent computational analysis will refer to the same SAMM inclusion presented in this chapter. The coefficients, K_{I}, K_{I}' and K_{I}'', are necessary to characterize a heterogeneous medium that contains some volume fraction of the SAMM inclusions. The following two chapters will apply the linear and nonlinear elastic moduli to standard formulations in acoustics to assist in understanding their response on both the microscale and macroscale from a nonlinear acoustical and dynamical standpoint.

Chapter 3

Acoustic Nonlinearity

This chapter focuses on the modeling tools necessary to describe the behavior of an acoustic wave propagating through a heterogeneous medium comprised of the SAMM inclusions embedded in an elastic matrix material. In order to gain an understanding of the overall macroscopic behavior, two homogenization techniques are considered. Both rely upon knowing the properties of a single SAMM inclusion, as given for the representative element presented in Section 2.3, and the surrounding matrix material. The nonlinear acoustical behavior of the inclusion is further considered here. The first homogenization approach, derived from a simple mixture law, is readily available from nonlinear acoustics and is more applicable to fluids. Thus a second method, which is based upon a Hashin-Shtrikman scheme and draws heavily from nonlinear elasticity, is applied to more accurately characterize the effective medium. In both cases, acoustical parameters of nonlinearity are presented to understand the response of the heterogeneous material and then utilized to determine the behavior of a propagating acoustic wave. While many aspects of the two methods are understood, applying them to composite materials containing SAMM inclusions provides a detailed description of the nonlinear multiscale physics with an overall material response that dif-

fers from that of conventional materials. The material models can therefore be used in conjunction with existing FEM of SAMM inclusion to generate a desired, nonlinear material response.

3.1 Acoustic Nonlinearities

Several equations of state used in nonlinear acoustics to relate pressure, density, and volume are presented here. The theory is extended to include cubic nonlinearities, which are negligibly small in comparison to quadratic nonlinearities for most materials and therefore reasonably discarded as insignificant. However, the higher order terms must be maintained with the SAMM inclusions because the constitutive relationship, introduced in Section 2.2, is a cubic function that has a strong dependence on a nonlinear, third order elastic modulus, K_{I}''. The significance of the cubic nonlinearity will be illustrated through comparisons with conventional materials.

3.1.1 State Equations

The standard isentropic equation of state utilized in nonlinear acoustics is derived from the Taylor series expansion of change in pressure as a function of change in density and assumes the following form [67]:

$$\frac{p}{\rho_0 c_0^2} = \left(\frac{\rho'}{\rho_0}\right) + \frac{B}{2A}\left(\frac{\rho'}{\rho_0}\right)^2 + \frac{C}{6A}\left(\frac{\rho'}{\rho_0}\right)^3 + \cdots , \tag{3.1}$$

where p is the acoustic pressure, ρ, ρ_0, and ρ' are instantaneous, ambient and excess density, respectively, such that $\rho = \rho_0 + \rho'$, and c_0 is the linear small

signal sound speed. The parameters of nonlinearity,B/A, C/A, etc., describe the degree of nonlinearity in the equation of state, and consequently also the deviation of the finite amplitude sound speed from its equilibrium, small signal value c_0 .

In Section 2.2, the SAMM inclusions were presented in terms of elasticity. In order to analyze them from a nonlinear acoustic standpoint, it is useful to relate the state equation in Eq. (3.1) as a function of other variables. One such relation expresses excess density, ρ', as a function of acoustic pressure, p. The form is derived by rearranging Eq. (3.1), such that the linear term in ρ' appears on the left-hand side,

$$\rho' = \frac{p}{c_0^2} - \frac{1}{\rho_0}\frac{B}{2A}\left(\rho'\right)^2 - \frac{1}{\rho_0^2}\frac{C}{6A}\left(\rho'\right)^3, \tag{3.2}$$

and then substituting the expansion of ρ' into the quadratic and cubic terms on the right-hand side of Eq. (3.2),

$$\begin{aligned}\rho' = \frac{p}{c_0^2} &- \frac{1}{\rho_0}\frac{B}{2A}\left[\frac{p}{c_0^2} - \frac{1}{\rho_0}\frac{B}{2A}\left(\rho'\right)^2 - \frac{1}{\rho_0^2}\frac{C}{6A}\left(\rho'\right)^3\right]^2 \\ &- \frac{1}{\rho_0^2}\frac{C}{6A}\left[\frac{p}{c_0^2} - \frac{1}{\rho_0}\frac{B}{2A}\left(\rho'\right)^2 - \frac{1}{\rho_0^2}\frac{C}{6A}\left(\rho'\right)^3\right]^3.\end{aligned} \tag{3.3}$$

Equation (3.2) is repeatedly substituted into the ρ' terms on the right-hand side of Eq. (3.3) until all terms up to third order are functions of p instead of ρ'. Any terms higher than third order are discarded. Regrouping like terms provides the desired density-pressure relation with ρ' expressed explicitly in terms of p,

$$\rho' = \frac{p}{c_0^2} - \frac{1}{\rho_0 c_0^4}\left(\frac{B}{2A}\right)p^2 - \frac{1}{\rho_0^2 c_0^6}\left[\frac{C}{6A} - \frac{1}{2}\left(\frac{B}{A}\right)^2\right]p^3. \tag{3.4}$$

Equation (3.4) is used in Appendix A.1 to derive the full three-dimensional wave equation that accounts for quadratic and cubic nonlinearities of the medium.

The effective behavior of the representative SAMM inclusion obtained from FEM is expressed in terms of pressure and volumetric strain in Section 2.2 [21]. It is therefore useful to rewrite Eq. (3.1) in terms of volume, or volumetric strain, using the relation [62]

$$\frac{\rho'}{\rho_0} = -\frac{v}{v + V_0} = -\frac{\varepsilon_v}{1 + \varepsilon_v} \tag{3.5}$$

in order to relate the effective stiffness of the SAMM inclusion to the acoustic parameters of nonlinearity. The desired expression is obtained by inserting the binomial expansion of the right-hand side of Eq. (3.5) up to third order into Eq. (3.1), which yields

$$\frac{p}{K} = -\varepsilon_v + \left(1 + \frac{B}{2A}\right)\varepsilon_v^2 - \left(1 + \frac{B}{A} + \frac{C}{6A}\right)\varepsilon_v^3, \tag{3.6}$$

where $K = \rho_0 c_0^2$ is the bulk modulus. Equation (3.6) is the stiffness form of the equation of state.

The compliance form of the state equation is also of interest here. The same recursive substitution method used to derive Eq. (3.4) is applied to Eq. (3.6). Retaining only terms up to third order in pressure yields

$$\varepsilon_v = -\frac{p}{K} + \left(1 + \frac{B}{2A}\right)\left(\frac{p}{K}\right)^2 + \left[\frac{C}{6A} - \frac{1}{2}\left(\frac{B}{A}\right)^2 - \frac{B}{A} - 1\right]\left(\frac{p}{K}\right)^3. \tag{3.7}$$

This form of the state equation will be useful in characterizing the effective parameters of a media containing SAMM inclusions.

Comparing Eqs. (2.20) and (3.6) permits one to relate the SAMM inclusions stiffness coefficients, K_{I}, K'_{I} and K''_{I}, to the parameters of nonlinearity to obtain values of B/A and C/A that pertain to one single inclusion,

$$\left(\frac{B}{A}\right)_{\text{I}} = \frac{K'_{\text{I}}}{K_{\text{I}}} - 2 \tag{3.8}$$

and

$$\left(\frac{C}{A}\right)_{\text{I}} = \frac{K''_{\text{I}}}{K_{\text{I}}} - 6\frac{K'_{\text{I}}}{K_{\text{I}}} + 6. \tag{3.9}$$

3.1.2 Parameters of Nonlinearity

The coefficient of nonlinearity β was introduced to characterize the quadratic nonlinearity in a progressive sound wave in a medium, where [67]

$$\beta = 1 + \frac{B}{2A}. \tag{3.10}$$

The "1" in Eq. (3.10) is a convection term due to geometric nonlinearity in the continuity equation, while the $B/2A$ accounts for material nonlinearity [68]. For elastic solids, the coefficient of nonlinearity is calculated using the Landau coefficients, $\mathcal{A}$, $\mathcal{B}$, and $\mathcal{C}$, which are referred to as third order elastic constants, the bulk modulus, K, and the shear modulus, μ, [67]

$$\beta = -\left(\frac{3}{2} + \frac{\mathcal{A} + 3\mathcal{B} + \mathcal{C}}{K + \frac{4}{3}\mu}\right). \tag{3.11}$$

The nonlinearity parameter for an elastic solid approaches the form for an inviscid fluid, where $K = A = \rho_0 c_l^2$, $\mathcal{A} = 0$, $\mathcal{B} = -A$ and $\mathcal{C} = (A - B)/2$, and thus Eq. (3.11) reduces to $\beta = 1 + B/2A$ [69]. Such an approximation

is applicable particularly to elastic solids characterized by $\mu/K \ll 1$. Elastic solid materials of this type are considered in the present research. Due to the nature of the derivation, the ratio B/A and Eq. (3.10) typically only describe the quadratic nonlinearity of liquids. However, by equating Eq. (3.10) and (3.11), an estimate of B/A for a solid material could be obtained.

In the same regard, the coefficient of nonlinearity γ is introduced here to characterize the nonlinearity at third order in a medium,

$$\gamma = \frac{3}{2}\left[\frac{C}{6A} - \frac{1}{2}\left(\frac{B}{A}\right)^2 - \frac{7B}{6A} - \frac{4}{3}\right]. \tag{3.12}$$

The form of Eq. (3.12) comes from the derivation of the one dimensional evolution equation for plane, progressive waves presented in Appendix A.2. Although coefficients of nonlinearity have been previously considered for cubic nonlinearity, e.g. Refs. [70, 71], the expressions include fourth-order elastic constants, which are difficult to obtain and rarely reported in the literature. Consideration of such coefficients describing cubic nonlinearity is therefore beyond the scope of the present work.

Table 3.1 shows estimates of the bulk modulus, K, in GPa, B/A, C/A, and C/B for some example fluids, solids, and mixtures containing bubbles obtained from the references cited in the table. The most common values of B/A are shown in the table for the organic and biological media in the first eleven rows; all are small and positive, falling within the range of 5 to 12. The exception is air, which has an even smaller B/A value of less than 1. However, it is possible to obtain large B/A, which is the case for rocks and bubbly liquids.

Material	$\boldsymbol{K}$ **[GPa]**	$\boldsymbol{B/A}$	$\boldsymbol{C/A}$	$\boldsymbol{C/B}$	**Ref.**
Air	1.21	0.4	–	–	[72]
Water	2.19	5	32	6.4	[73]
Ethanol	1.11	10.5[72]	165.9	15.8	[73]
Benzene	1.54	9[72]	89.99	10	[74]
Methanol	1.00	9.6[72]	98.96	10.3	[74]
Octane	1.01	11.3	159.44	14.1	[74]
Pig Liver	2.54	6.7[67]	116.5	17.4	[75]
Canine Spleen	2.48	6.8[67]	108.9	16	[75]
Canine Kidney	2.46	7.2[67]	112.8	15.7	[75]
Pig Fat	2.12	10.9[67]	102.2	9.4	[75]
Whole Porcine Blood	2.56	6.2[67]	42.1	6.8	[74]
Limestone 1083	29.6	1077.9	–	–	[76]
Westerly Granite	29.9	2469	–	–	[76]
Massilon Sandstone	6.1	5066.7	–	–	[76]
Pyrex Glass	31.0	-10.78	–	–	[77]
Fused Silica	78.39	-9.91	–	–	[78]
Water with $\phi = 1\%$ gas bubbles	0.01	236.9	–	–	[79]
Water with $\phi = 0.1\%$ gas bubbles	0.13	2116.8	–	–	[79]
Water with $\phi = 0.01\%$ gas bubbles	0.86	8836.4	–	–	[79]
Microspheres in Castor Oil at $P \simeq 75$ kPa	0.04	-6398	–	–	[80]
Microspheres in Castor Oil at $P \simeq 88$ kPa	0.13	-3000	–	–	[80]

Table 3.1: Bulk modulus, B/A, C/A and C/B for example fluids, solids, and mixtures containing bubbles from the references denoted in the last column unless otherwise noted in the table cells.

The parameters of nonlinearity for the three example rocks, Limestone 1083, Westerly Granite, and Massilon Sandstone, are determined from information provided from Ref. [76] using Eqs. (3.10) and (3.11). It is worth noting that the nonlinearity of rocks is rarely described using B/A notation, but is done so here as a convenience to compare the behavior of different materials. The results show that rock can have parameters of nonlinearity on the order of 10^3, due to inhomogeneities caused by micro-cracking, which is much greater than for the biological and organic materials. Bubbly liquids also enhance the nonlinearity parameters. The three examples of water containing air bubbles in Table 3.1 are determined using the information provided in Ref. [79] for three volume fractions of bubbles in water: $\phi = 1\%$, $\phi = 0.1\%$, and $\phi = 0.01\%$. Furthermore, it is possible to obtain negative values of B/A. Some materials, such as Pyrex glass [77] and fused silica [78], naturally have a negative parameter of nonlinearity. Other instances of negative have been reported in fluids in the proximity of a critical point during a phase transformation [81].

Phase transformation can lead to simultaneously large and negative parameters of nonlinearity. Such a response was measured by Trivett *et al.* for an increasing applied hydrostatic pressure to a heterogeneous media comprised of castor oil and encapsulated microspheres [80]. In the experiment, a hydrostatic pressure was imposed on the mixture of castor oil containing hollow microspheres and was increased until the thin elastic shells of the microspheres buckled. The result was an abrupt reduction in the stiffness of the microspheres and an associated decrement in the sound speed in the mixture,

which gave rise to large and negative values for B/A. Two values of hydrostatic pressure and the subsequent sound speed and parameter of nonlinearity measured from their experiment appear in Table 3.1, where $B/A = -6398$ is the peak value, occurring roughly when $P \simeq 75$ kPA. In terms of elastic energy, buckling phenomena display very similar behavior to phase transformation. Because the SAMM inclusions rely on buckling phenomena to generate their unique performance, it is therefore anticipated that the SAMM inclusions may enable the generation of large and negative values of B/A.

Values of C/A are less commonly reported in the literature and thus only appear in Table 3.1 for the organic and biological media. The largest value shown in the table is the value of C/A for ethanol, 165.9. The magnitudes of cubic nonlinearities are often small enough that their effects are negligible in comparison to quadratic nonlinearities [73]. At most, C/A is an order of magnitude larger than the values of B/A for that same material. As a point of reference for the quadratic and cubic nonlinearity to be considered in Section 3.2, the ratio C/B is also calculated in Table 3.1. The largest magnitude is 17.4, which is the ratio of C/B for pig liver. For the cubic nonlinearity to have a significant effect, the ratio C/B must be several orders of magnitude larger than the ones shown in Table 3.1.

3.2 Homogenization

The macroscopic behavior of a heterogeneous material containing subwavelength SAMM inclusions is one of the primary interests of the present re-

search. The effective properties of a heterogeneous material containing SAMM inclusions is explored in the following section using two different methods. A schematic of the multiscale model considered here is diagrammed in Fig. 3.1. Figure 3.1(a) depicts the macroscale, where the heterogeneous medium is a representative volume element with radius R_*, surrounded by some matrix material. The mesoscale, depicted in Fig. 3.1(b), is an intermediate scale between the microscale and macroscale showing a dilute concentration of randomly dispersed inclusions that are perfectly bonded to the matrix. The inclusions are assumed to be non-interacting. The microscale is then represented in Fig. 3.1(c) as one single inclusion of radius R_{I} embedded in the matrix. The scale of the inclusion is assumed to be much smaller than the wavelengths of an acoustic disturbance propagating in both the matrix and the effective medium, such that $k_* R_{\mathrm{I}} \ll 1$ and $k_{\mathrm{M}} R_{\mathrm{I}} \ll 1$, as well as the wavelength of the highest harmonic, where $k_{\mathrm{hrm}} R_{\mathrm{I}} \ll 1$. The subscripts on the acoustic wave number, k, refer to the effective medium, matrix, and highest harmonic of interest, respectively.

The volume fraction of SAMM inclusions within the effective medium at ambient pressure is given by

$$\phi = \frac{N V_{\mathrm{I}_0}}{V_{*_0}} = N \left(\frac{R_{\mathrm{I}_0}}{R_{*_0}} \right)^3, \tag{3.13}$$

where N is the number of inclusions, V_{I_0} and R_{I_0} correspond to the equilibrium volume and radius of one inclusion, and V_{*_0} and R_{*_0} refer to the equilibrium volume and radius of the entire effective medium. Throughout the remainder

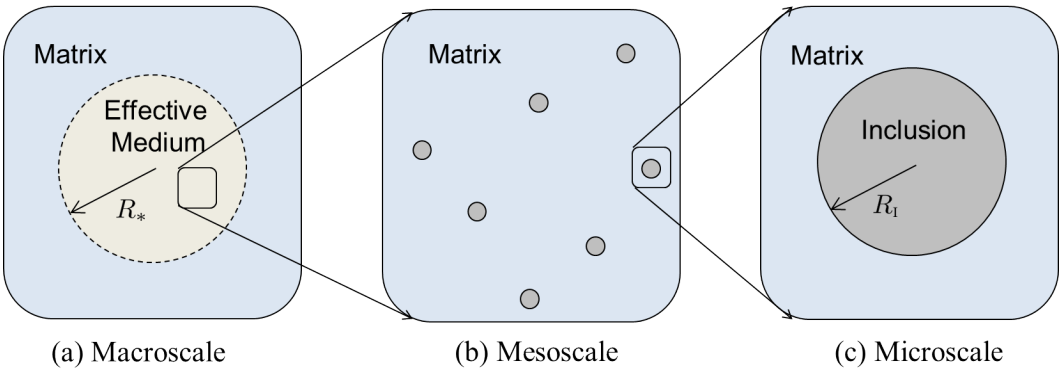

Figure 3.1: Multiscale model for an effective medium containing a dilute concentration of inclusions showing the macroscale, mesoscale and microscale.

of the thesis, the effective medium will always be denoted by an $*$, the SAMM inclusion by the subscript I, and the matrix material by the subscript M.

3.2.1 Mixture Law Homogenization Approach

An initial estimate of the effective coefficients of nonlinearity, denoted by β_* and γ_*, is obtained here using the immiscible mixture law. Originally developed by Apfel [82] and later corrected by Everbach *et al.* [83, 84], the mixture law provides a homogenization technique that has been applied to emulsions, defined as immiscible fluid mixtures, such as gas bubbles in water or oil. The approach is also applied to compositions of nearly incompressible biological tissues that can be modeled as fluid-like media. However, the method is only valid for $\mu/K \ll 1$, and is thus not as well suited for suspensions (solids suspended in a fluid) or composite elastic materials.

3.2.1.1 Theoretical Formulation

For a composite medium with n immiscible components, the mixture law relies upon the following assumptions: (i) both the homogenized medium and each of the n components undergo the same change in pressure p, and thus each individually obey Eq. (3.7); and (ii) the total change in volume of the homogenized medium, v_*, is the summation of the respective volume changes of each of the n components. The total change in volume of the effective medium, as given in Eq. (3.7), is expressed in terms of β_* and γ_* from Eqs. (3.10) and (3.12), such that

$$\frac{v_*}{V_0} = -\frac{p}{K_*} + \frac{\beta_* p^2}{K_*^2} + \frac{(2\gamma_* + \beta_*)\, p^3}{3K_*^3}. \tag{3.14}$$

The second assumption requires

$$\frac{v_*}{V_{*_0}} = -p \sum_{h=1}^{n} \frac{\phi_h}{K_h} + p^2 \sum_{h=1}^{n} \frac{\phi_h \beta_h}{K_h^2} + p^3 \sum_{h=1}^{n} \frac{\phi_h \,(2\gamma_h + \beta_h)}{3K_h^3}, \tag{3.15}$$

where ϕ_h is the volume fraction of each component of the heterogeneous medium. The two assumptions dictate that Eq. (3.14) be equal to Eq. (3.15). The effective medium of interest has $n = 2$ components: the SAMM inclusions and the matrix material. Equating like terms of the same order of pressure for the two phase medium provides the following expressions for the effective bulk modulus, K_*,

$$K_*^{\mathrm{ML}} = \frac{K_{\mathrm{M}}}{1 + \phi \left(\dfrac{K_{\mathrm{M}}}{K_{\mathrm{I}}} - 1 \right)}, \tag{3.16}$$

and coefficients that characterizes quadratic nonlinearity,

$$\beta_*^{\mathrm{ML}} = \left(\frac{K_*^{\mathrm{ML}}}{K_{\mathrm{I}}}\right)^2 \beta_{\mathrm{I}}\phi + \left(\frac{K_*^{\mathrm{ML}}}{K_{\mathrm{M}}}\right)^2 \beta_{\mathrm{M}}\left(1-\phi\right), \tag{3.17}$$

and cubic nonlinearity,

$$\gamma_*^{\mathrm{ML}} = \frac{1}{2}\left[\left(\frac{K_*^{\mathrm{ML}}}{K_{\mathrm{I}}}\right)^3 \phi\left(2\gamma_{\mathrm{I}}+\beta_{\mathrm{I}}\right) + \left(\frac{K_*^{\mathrm{ML}}}{K_{\mathrm{M}}}\right)^3 \left(1-\phi\right)\left(2\gamma_{\mathrm{M}}+\beta_{\mathrm{M}}\right) - \beta_*^{\mathrm{ML}}\right]. \tag{3.18}$$

For these estimates of the effective material properties, the superscript ML indicates that the parameters are obtained using the mixture law approach. Equations (3.16)–(3.18) are equivalent to those that appear in Ref. [84], which expresses the effective parameters in terms of B/A and C/A. Equations (3.17) and (3.18) are related to B/A and C/A through the expressions

$$\left(\frac{B}{A}\right)_* = 2\left(\beta_* - 1\right) \tag{3.19}$$

and

$$\left(\frac{C}{A}\right)_* = 2\left(2\gamma_* + 3\beta_*^2 - 5\beta_* + 3\right). \tag{3.20}$$

3.2.1.2 Mixture Law Homogenization Results

The nonlinearity of an effective medium containing the SAMM inclusions is now explored. The expressions for the effective $(B/A)_*^{\mathrm{ML}}$ and $(C/A)_*^{\mathrm{ML}}$ are obtained from β_*^{ML} and γ_*^{ML} through Eqs. (3.17)–(3.20). For simplicity, the matrix material is taken to be water, and the values of K_{M}, $\left(B/A\right)_{\mathrm{M}}$ and $\left(C/A\right)_{\mathrm{M}}$ are given in Table 3.1. The coefficients of nonlinearity of the representative SAMM inclusion, β_{I} and γ_{I}, as given by Eqs. (3.8)–(3.10) and (3.12),

depend on local stiffness parameters, K_{I}, K'_{I}, and K''_{I}. In Section 2.3.2, K_{I}, K'_{I}, and K''_{I} were obtained from the FEM data, as shown in Figs. 2.8–2.10. The nonlinear elastic parameters for the SAMM inclusion, which vary with strain, and the parameters describing the matrix, which are constant, are then used to obtain K_*^{ML}, $(B/A)_*^{\mathrm{ML}}$, and $(C/A)_*^{\mathrm{ML}}$ in Figs. 3.2–3.5. Because the parameters of stiffness and nonlinearity of the SAMM inclusion rely heavily on their strain state, the effective parameters of nonlinearity and bulk modulus also depend on the volumetric pre-strain of the SAMM inclusion. For the example effective medium, the volume fraction of SAMM inclusions in the matrix is $\phi = 1\%$.

The computed values for the effective B/A are plotted in Fig. 3.2 as a function of the change in volume on the SAMM inclusion scale. The x-axis represents the pre-strain from the equilibrium volume, V_{I_0}, when no external forces are applied. As the applied pre-strains approach the states corresponding to zero linear stiffness on the microscale, denoted by the vertical red dashed lines, the macroscale nonlinearity parameter, $(B/A)_*$, approaches positive or negative infinity. The vertical black lines that line up with the red dashed lines at the essential nonlinearities are asymptotes that indicate the value of $(B/A)_*$ flipping from negative to positive values, or vice versa. The exact magnitudes at the essential nonlinearities are dependent on how close the magnitude of K_{I} is to 0.

The behavior is similar to the buckling of the encapsulated microspheres from Ref. [80] that was discussed in Section 3.1.2. As the pre-strain on the SAMM inclusions increases, like the hydrostatic pressure on the microspheres,

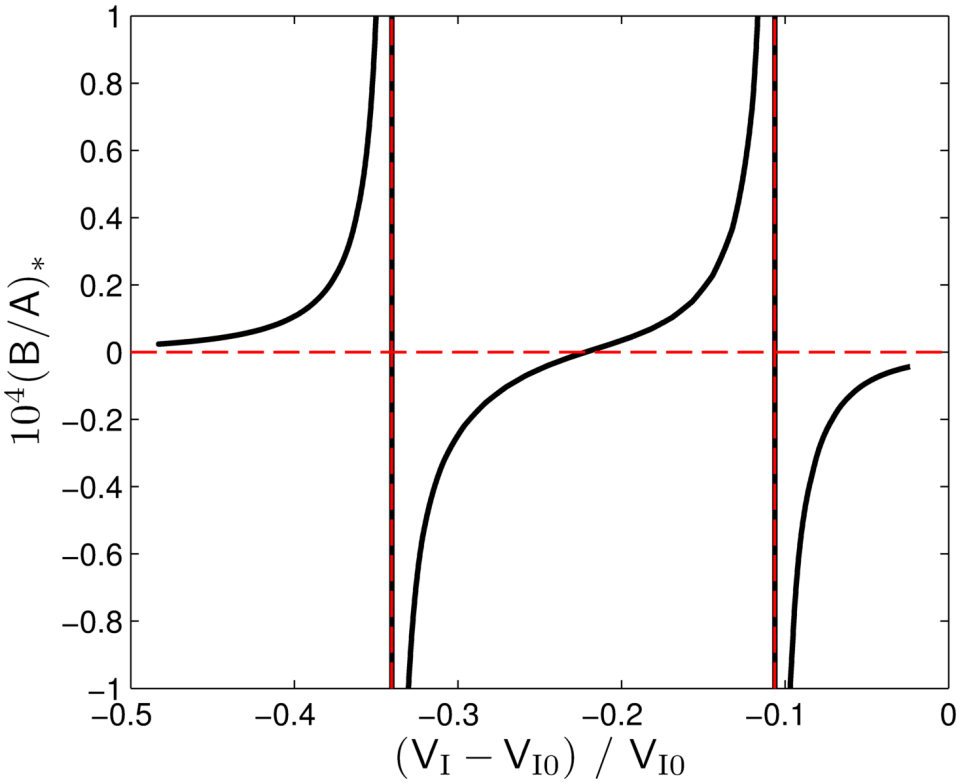

Figure 3.2: $(B/A)_*$ derived from the mixture law with $\phi = 1\%$ SAMM inclusions in water.

the stiffness changes. The magnitude of $(B/A)_*$ becomes very large for both the SAMM inclusion and the encapsulated microspheres as the imposed external forces approach the pre-strained state that will induce buckling. It is worth noting that the SAMM inclusion undergoes a perfectly recoverable deformation. Although Trivett *et al.* also described the process of the buckling of the microspheres as "reversible and repeatable" unless the hydrostatic pressure is imposed for an extended time frame [80], microspheres are more likely to get destroyed due to a hydrostatic loading process than the SAMM inclu-

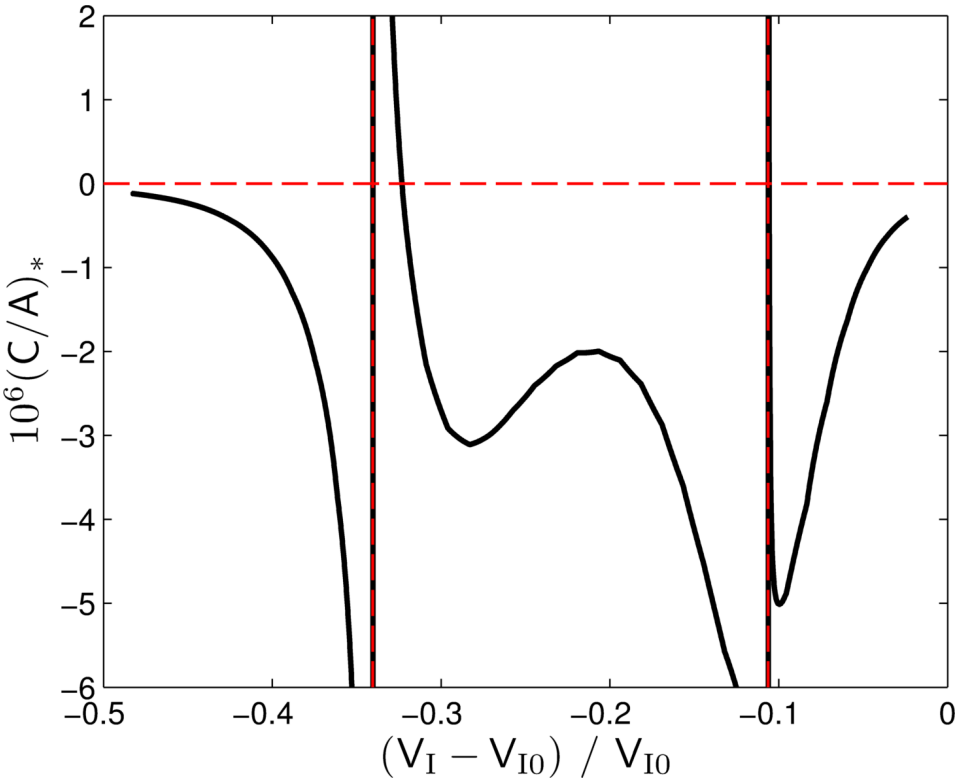

Figure 3.3: $(C/A)_*$ derived from the mixture law with $\phi = 1\%$ SAMM inclusions in water.

sions. Furthermore, the SAMM inclusions exhibit a large response for multiple pre-strains, corresponding to the two limit points where the snapping will occur. Even at pre-strains away from the essential nonlinearities, the values of $(B/A)_*$ are still significantly larger than B/A for organic and biological media given in Table 3.1.

Figure 3.3 shows a similar behavior for computed values of $(C/A)_*$. Once again, as the SAMM inclusion approaches a configuration that corresponds to zero linear stiffness, the magnitudes of $(C/A)_*$ become larger. In

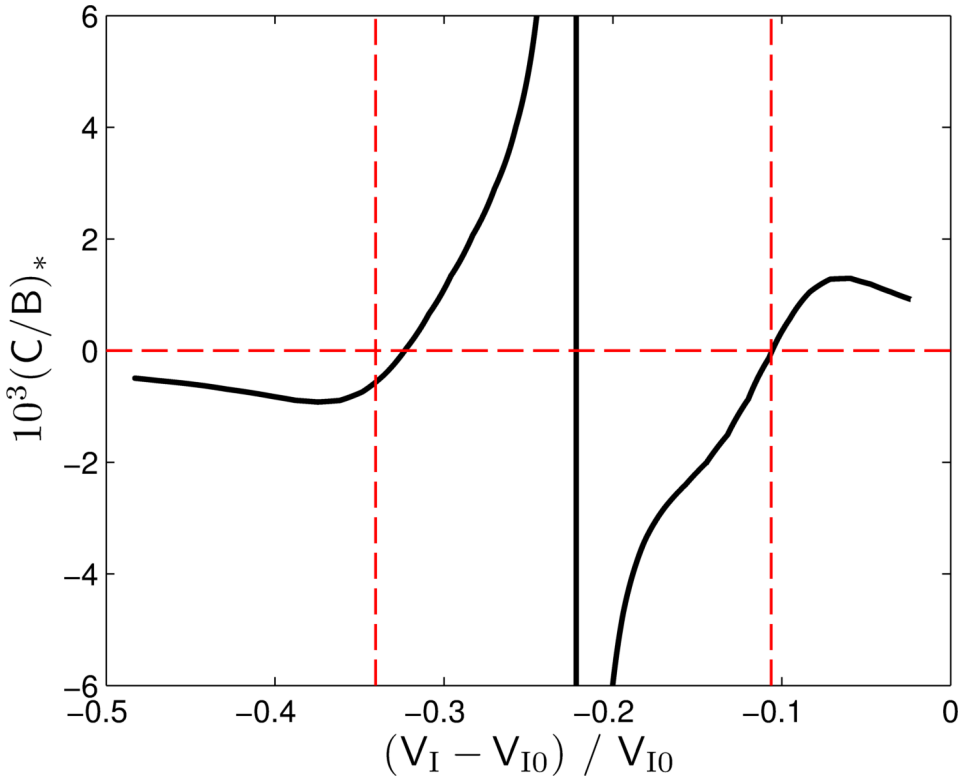

Figure 3.4: $(C/B)_*$ derived from the mixture law with $\phi = 1\%$ SAMM inclusions in water.

order to emphasize the significance of the cubic nonlinearity, the ratio $(C/B)_*$ is shown as a function of volumetric strain. For the range of imposed pre-strains considered in Fig. 3.4, there are volumetric strains that correspond to $(C/B)_* \sim 0$. Thus, $(C/A)_*$ is much smaller than $(B/A)_*$ at these volumetric strains because the zero of $(B/A)_*$ does not coincide with the zeros of $(C/A)_*$. The magnitude of $(C/B)_*$ becomes the largest within negative stiffness regime of the SAMM inclusion, occurring for the volumetric strains between the vertical red dashed lines. Recall from Table 3.1 that the largest ratio of C/B

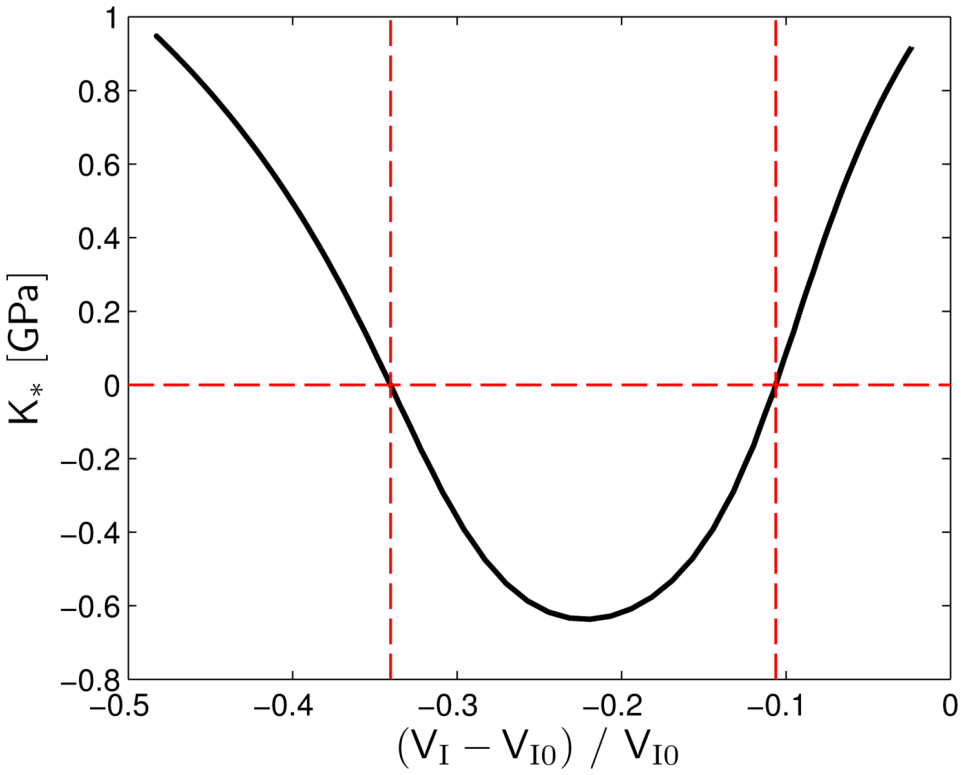

Figure 3.5: K_* derived from the mixture law with $\phi = 1\%$ SAMM inclusions in water.

for conventional materials currently reported was only 17.4. The ratios of $(C/B)_*$ in Fig. 3.4 obtain much larger magnitudes. Therefore, one expects the macroscopic response of the heterogeneous medium to exhibit strong cubic nonlinearities due to the SAMM inclusions.

Qualitatively, the behavior shown in Figs. 3.2–3.4 is exactly as expected; as pre-strain approaches zero linear inclusion stiffness, the nonlinearity of the SAMM inclusion and subsequently, the effective medium, increases. However, the behavior of the effective bulk modulus, as presented in Fig. 3.5, does not

completely describe the system of interest. The effective bulk modulus in Eq. (3.16) is also obtained from the volume average of a Reuss composite in continuum mechanics, which is known to underestimate the effective bulk modulus of composites for all but a few very specific cases [2].

The effective bulk modulus plotted in Fig. 3.5 indicates that for certain ranges of pre-strain, the negative values of the effective linear stiffness of the SAMM inclusions, K_{I}, induces a negative effective bulk modulus of the heterogeneous medium. The vertical red dashed lines once again correspond to the essential nonlinearities of the SAMM inclusions. However, as evident in Fig. 3.5, K_* becomes negative for the pre-strains between the vertical red dashed lines and thus the signs of K_{I} and K_* are the same. A negative value of the effective medium implies that the medium is unstable for these strain values [62]. Such a medium will not support wave motion because it leads to a purely imaginary sound speed (i.e., evanescent waves). For a fluid, the mixture law is a reasonable description of the effective behavior, but for certain properties of the surrounding elastic matrix, an element with a negative stiffness phase can be stably constrained to generate an overall, positive effective stiffness of the composite [6]. Upon reviewing the assumptions made for the mixture law approach, it is clear that conservation of volume holds for any material regardless of the constituents, but the requirement of continuity of pressure in all materials does not account for an elastic body's ability to resist shearing deformation. It is therefore of interest to derive a model for the effective behavior of an elastic medium containing SAMM inclusions. Any

such model must account for the shear modulus in the elastic matrix material in order to stabilize the SAMM materials when $K_{\text{I}} < 0$. Section 3.2.2 presents the adoption of a Hashin-Shtrikman scheme to describe a nonlinear inclusion up to third order within an elastic matrix with a non-zero shear modulus.

3.2.2 Hashin-Shtrikman Approach

Hashin and Strikman rigorously derived bounds, termed the Hashin-Shtrikman bounds, for the effective elastic moduli for a heterogeneous material, which, along with its constituents, obeys linear elasticity [85]. For a two-phase medium, the composite is modeled as a sphere surrounded by a shell. The upper and lower bounds can be obtained simply by applying continuity of normal displacement and normal stress at the inclusion-shell and shell-effective medium boundaries, providing four equations and four unknowns that give rise to an expression for the effective bulk modulus [2]. The Hashin-Shtrikman approach is adapted here for a SAMM inclusion embedded in a matrix and extends the model to include nonlinear elasticity.

Consider the representative volume element shown in Fig. 3.6. In Fig. 3.6(a), a nonlinear inclusion with known elastic parameters and radius R_{I_0} is embedded in some infinite matrix with known elastic parameters. The dashed circle of radius R_{*_0} is an representative volume element encompassing the entire inclusion and some of the matrix that is homogenized as an effective medium surrounded by the matrix, as shown in Fig. 3.6(b). The effective elastic parameters, K_*, K'_* and K''_*, are the unknowns obtained from

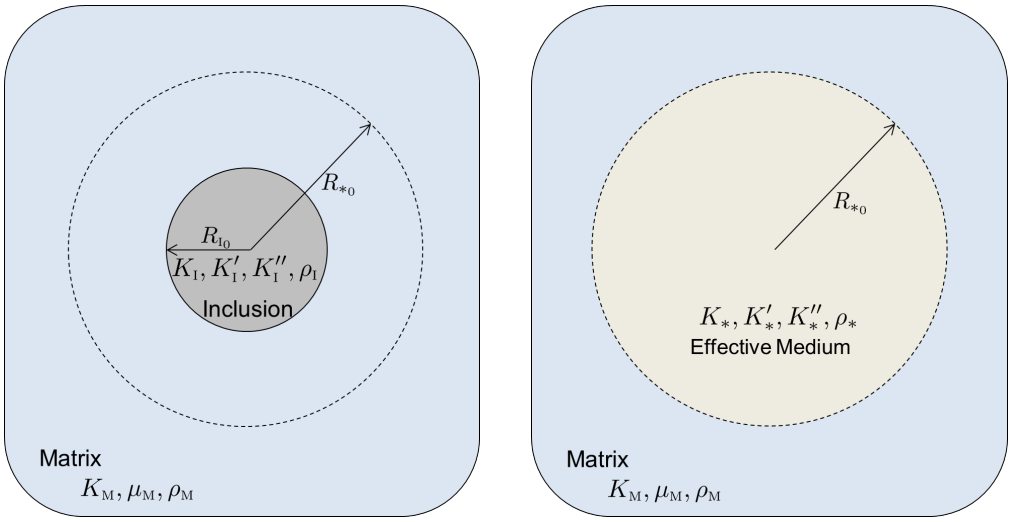

(a) Matrix-Inclusion (b) Matrix-Effective Medium

Figure 3.6: Schematic of homogenization using a Hashin-Shtrikman homogenization scheme.

this derivation.

3.2.2.1 Theoretical Formulation

The SAMM inclusion, matrix material, and effective medium are assumed to undergo large deformations. Therefore, the geometrical nonlinearities of the deformation must be described using finite elasticity. However, nonlinear deformations are more complicated than the behavior modeled by linear elasticity because few closed-form solutions exist for general cases of finite deformations. One simplifying assumption utilized here is that all deformations are spherically symmetric. A summary of six classes of elastic materials with closed form solutions for spherically symmetric deformations are presented in Ref. [86] with more details available in the references therein.

The simplest model is Class I, which describes harmonic materials that deforms such that the deformation gradient is always symmetric [87]. The radial displacement for a harmonic material is given by

$$u_r^{\mathrm{M}} = a_{\mathrm{M}} r + \frac{b_{\mathrm{M}}}{r^2}, \tag{3.21}$$

where a_{M} and b_{M} are constants describing the deformation in the matrix and r is the Lagragian radial coordinate. Even though the deformation is nonlinear, the strain energy density and subsequent stress-strain constitutive relationship can still be linear. From Ref. [6], the strain energy density for a linear harmonic material can be expressed as

$$\begin{aligned} \mathscr{E}^{\mathrm{M}} = &\frac{1}{2}\left(K_{\mathrm{M}} + \frac{4}{3}\mu_{\mathrm{M}}\right)\lambda_{rr}^2 + 2\left(K_{\mathrm{M}} - \frac{1}{3}\mu_{\mathrm{M}}\right)\lambda_{\theta\theta}^2 \\ &+ 2\left(K_{\mathrm{M}} - \frac{2}{3}\mu_{\mathrm{M}}\right)\lambda_{rr}\lambda_{\theta\theta} - 3K_{\mathrm{M}}\left(\lambda_{rr} + 2\lambda_{\theta\theta}\right), \end{aligned} \tag{3.22}$$

where λ_{rr}, $\lambda_{\theta\theta}$, and $\lambda_{\phi\phi}$ are the invariants of the deformation gradient, with $\lambda_{\theta\theta} = \lambda_{\phi\phi}$ for the case of a spherically symmetric deformation. The invariants are given by

$$\lambda_{rr} = 1 + a_{\mathrm{M}} - \frac{2b_{\mathrm{M}}}{r^3}, \qquad \lambda_{\theta\theta} = 1 + a_{\mathrm{M}} + \frac{b_{\mathrm{M}}}{r^3}. \tag{3.23}$$

The relationship for Cauchy stress in terms of strain energy density and the invariants of the deformation gradient are given by [86]

$$\sigma_{ij} = \frac{\lambda_{ij}}{\lambda_{rr}\lambda_{\theta\theta}\lambda_{\phi\phi}}\frac{\partial \mathcal{E}}{\partial \lambda_{ij}}, \tag{3.24}$$

where the repeated indices, ij, do not indicate a summation. Differentiating Eq. (3.22) with respect to λ_{rr} and substituting the relations given in Eq. (3.23)

into Eq. (3.24) reduces the radial component of the Cauchy stress to

$$\sigma_{rr}^{\mathrm{M}} = \left(a_{\mathrm{M}} + \frac{b_{\mathrm{M}}}{r^3} + 1\right)^{-2} \left(3K_{\mathrm{M}}a_{\mathrm{M}} - 4\mu_{\mathrm{M}}\frac{b_{\mathrm{M}}}{r^3}\right). \tag{3.25}$$

Additional information regarding the derivation of the radial displacement and radial Cauchy stress for the harmonic material is in Appendix B.

The effective elastic moduli are obtained by satisfying continuity conditions at the inclusion-matrix and matrix-effective medium interfaces. Expressions for the radial displacement and radial Cauchy stress describing the SAMM inclusion and effective medium are therefore necessary. The behavior of the SAMM inclusion was described in Section 2.2. The radial displacement is given in Eq. (2.8). From Eqs. (2.5), (2.10), and (2.17)–(2.19), the radial Cauchy stress of the SAMM inclusion is expressed as

$$\sigma_{rr}^{\mathrm{I}} = 3\left[K_{\mathrm{I}}\left(a_{\mathrm{I}} + \frac{3}{2}a_{\mathrm{I}}^2\right) - \frac{3}{2}K_{\mathrm{I}}'\left(a_{\mathrm{I}} + \frac{3}{2}a_{\mathrm{I}}^2\right)^2 + \frac{3}{2}K_{\mathrm{I}}''\left(a_{\mathrm{I}} + \frac{3}{2}a_{\mathrm{I}}^2\right)^3\right], \tag{3.26}$$

where the pressure offset P_{I_0} is taken to be zero.

The expressions describing the deformation of the effective medium have the same form as those of the SAMM inclusion. Therefore, the radial displacement is

$$u_r^* = a_* r, \tag{3.27}$$

and the radial Cauchy stress is

$$\sigma_{rr}^* = 3\left[K_*\left(a_* + \frac{3}{2}a_*^2\right) - \frac{3}{2}K_*'\left(a_* + \frac{3}{2}a_*^2\right)^2 + \frac{3}{2}K_*''\left(a_* + \frac{3}{2}a_*^2\right)^3\right]. \tag{3.28}$$

Continuity of radial displacement at the interface between the SAMM inclusion and the matrix, $u_r^{\mathrm{I}}(r = R_{\mathrm{I}_0}) = u_r^{\mathrm{M}}(r = R_{\mathrm{I}_0})$, yields

$$\frac{b_{\mathrm{M}}}{R_{\mathrm{I}_0}^3} = a_{\mathrm{I}} - a_{\mathrm{M}}. \tag{3.29}$$

Similarly, continuity of radial displacement at the interface between the effective medium and the matrix, $u_r^*(r = R_{*_0}) = u_r^{\mathrm{M}}(r = R_{*_0})$, provides

$$\frac{b_{\mathrm{M}}}{R_{*_0}^3} = a_* - a_{\mathrm{M}}. \tag{3.30}$$

Combining Eqs. (3.29) and (3.30), and using the definition of volume fraction from Eq. (3.13) with $N = 1$ gives rise to the expression

$$a_* = \phi a_{\mathrm{I}} + (1 - \phi)\, a_{\mathrm{M}}. \tag{3.31}$$

Continuity of radial stress at the interface between the SAMM inclusion and matrix, $\sigma_{rr}^{\mathrm{I}}(r = R_{\mathrm{I}_0}) = \sigma_{rr}^{\mathrm{M}}(r = R_{\mathrm{I}_0})$, provides

$$\begin{aligned} K_{\mathrm{I}} \left(a_{\mathrm{I}} + \frac{3}{2} a_{\mathrm{I}}^2 \right) - \frac{3}{2} K_{\mathrm{I}}' \left(a_{\mathrm{I}} + \frac{3}{2} a_{\mathrm{I}}^2 \right)^2 + \frac{3}{2} K_{\mathrm{I}}'' \left(a_{\mathrm{I}} + \frac{3}{2} a_{\mathrm{I}}^2 \right)^3 \\ = \left(1 + 2a_{\mathrm{I}} + a_{\mathrm{I}}^2\right)^{-1} \left[\left(K_{\mathrm{M}} + \frac{4}{3} \mu_{\mathrm{M}} \right) a_{\mathrm{M}} - \frac{4}{3} \mu_{\mathrm{M}} a_{\mathrm{I}} \right]. \end{aligned} \tag{3.32}$$

The term b_{M} is eliminated in Eq. (3.32) through the use of Eq. (3.29). Since the radial stress of the SAMM inclusion is a third order expansion, the effective parameters only require the retention of terms to third order with respect to a_{I},

$$\begin{aligned} \left(K_{\mathrm{I}} + \frac{4}{3} \mu_{\mathrm{M}} \right) a_{\mathrm{I}} + \frac{1}{2} \left(7K_{\mathrm{I}} - 3K_{\mathrm{I}}' \right) a_{\mathrm{I}}^2 + \frac{1}{2} \left(8K_{\mathrm{I}} - 15K_{\mathrm{I}}' + 3K_{\mathrm{I}}'' \right) a_{\mathrm{I}}^3 \\ \simeq \left(K_{\mathrm{M}} + \frac{4}{3} \mu_{\mathrm{M}} \right) a_{\mathrm{M}}. \end{aligned} \tag{3.33}$$

At the matrix-effective medium interface, continuity of radial stress must once again be satisfied, such that $\sigma^{*}_{rr}(r = R_{*_0}) = \sigma^{\mathrm{M}}_{rr}(r = R_{*_0})$. By retaining terms only up to cubic order of a_*, the relation for continuity of normal stress reduces to

$$\left(K_* + \frac{4}{3}\mu_{\mathrm{M}}\right) a_* + \frac{1}{2}\left(7K_* - 3K'_*\right) a_*^2 + \frac{1}{2}\left(8K_* - 15K'_* + 3K''_*\right) a_*^3 \simeq \left(K_{\mathrm{M}} + \frac{4}{3}\mu_{\mathrm{M}}\right) a_{\mathrm{M}}. \tag{3.34}$$

The right-hand side of Eqs. (3.33) and (3.34) are identical, and thus one can equate their left-hand sides. In order to derive expressions for the effective elastic moduli, a_* must be expressed as a function of the unknown a_{I} and the known inclusion and matrix parameters. First, an expression for a_{M} as a function of a_{I} is derived from Eq. (3.33), such that

$$a_{\mathrm{M}} = \frac{\left(K_{\mathrm{I}} + \frac{4}{3}\mu_{\mathrm{M}}\right) a_{\mathrm{I}} + \frac{1}{2}\left(7K_{\mathrm{I}} - 3K'_{\mathrm{I}}\right) a_{\mathrm{I}}^2 + \frac{1}{2}\left(8K_{\mathrm{I}} - 15K'_{\mathrm{I}} + 3K''_{\mathrm{I}}\right) a_{\mathrm{I}}^3}{\left(K_{\mathrm{M}} + \frac{4}{3}\mu_{\mathrm{M}}\right)}. \tag{3.35}$$

Substituting Eq. (3.35) into Eq. (3.31) provides the desired expression for a_*,

$$a_* = \left(K_{\mathrm{M}} + \frac{4}{3}\mu_{\mathrm{M}}\right)^{-1} \left\{ \left[\phi\left(K_{\mathrm{M}} - K_{\mathrm{I}}\right) + \left(K_{\mathrm{I}} + \frac{4}{3}\mu_{\mathrm{M}}\right)\right] a_{\mathrm{I}} + \frac{1}{2}\left(1 - \phi\right)\left[\left(7K_{\mathrm{I}} - 3K'_{\mathrm{I}}\right) a_{\mathrm{I}}^2 + \left(8K_{\mathrm{I}} - 15K'_{\mathrm{I}} + 3K''_{\mathrm{I}}\right) a_{\mathrm{I}}^3\right] \right\}. \tag{3.36}$$

The desired expression is obtained by combing Eq. (3.33) with Eq. (3.34) while making use of the expression for a_* given by Eq. (3.36). If terms higher than a_{I}^3 are discarded when taking the square and cube of Eq. (3.36), then the result is a function of the known SAMM and matrix moduli, unknown coefficients a_{I}

and unknown effective elastic moduli:

$$\begin{aligned}
&\left(K_{\mathrm{I}}+\frac{4}{3}\mu_{\mathrm{M}}\right)a_{\mathrm{I}}+\frac{1}{2}\left(7K_{\mathrm{I}}-3K_{\mathrm{I}}'\right)a_{\mathrm{I}}^{2}+\frac{1}{2}\left(8K_{\mathrm{I}}-15K_{\mathrm{I}}'+3K_{\mathrm{I}}''\right)a_{\mathrm{I}}^{3}\\
&\quad=\left(K_{*}+\frac{4}{3}\mu_{\mathrm{M}}\right)\left(K_{\mathrm{M}}+\frac{4}{3}\mu_{\mathrm{M}}\right)^{-1}\left\{\left[\phi\left(K_{\mathrm{M}}-K_{\mathrm{I}}\right)+\left(K_{\mathrm{I}}+\frac{4}{3}\mu_{\mathrm{M}}\right)\right]a_{\mathrm{I}}\right.\\
&\qquad\left.+\frac{1}{2}\left(1-\phi\right)\left[\left(7K_{\mathrm{I}}-3K_{\mathrm{I}}'\right)a_{\mathrm{I}}^{2}+\left(8K_{\mathrm{I}}-15K_{\mathrm{I}}'+3K_{\mathrm{I}}''\right)a_{\mathrm{I}}^{3}\right]\right\}\\
&\qquad+\frac{1}{2}\left(7K_{*}-3K_{*}'\right)\left(K_{\mathrm{M}}+\frac{4}{3}\mu_{\mathrm{M}}\right)^{-2}\left\{\left[\phi\left(K_{\mathrm{M}}-K_{\mathrm{I}}\right)+\left(K_{\mathrm{I}}+\frac{4}{3}\mu_{\mathrm{M}}\right)\right]^{2}a_{\mathrm{I}}^{2}\right.\\
&\qquad\left.+\left(1-\phi\right)\left(7K_{\mathrm{I}}-3K_{\mathrm{I}}'\right)\left[\phi\left(K_{\mathrm{M}}-K_{\mathrm{I}}\right)+\left(K_{\mathrm{I}}+\frac{4}{3}\mu_{\mathrm{M}}\right)\right]a_{\mathrm{I}}^{3}\right\}\\
&\qquad+\frac{1}{2}\left(8K_{*}-15K_{*}'+3K_{*}''\right)\left(K_{\mathrm{M}}+\frac{4}{3}\mu_{\mathrm{M}}\right)^{-3}\\
&\qquad\qquad\times\left[\phi\left(K_{\mathrm{M}}-K_{\mathrm{I}}\right)+\left(K_{\mathrm{I}}+\frac{4}{3}\mu_{\mathrm{M}}\right)\right]^{3}a_{\mathrm{I}}^{3}. \qquad (3.37)
\end{aligned}$$

If $a_{\mathrm{I}}=0$, Eq. (3.37) is trivially satisfied. Thus to avoid the trivial solution, all terms at each respective order of a_{I} must equal zero. The effective bulk modulus is obtained by equating all terms at first order, such that

$$K_{*}=\frac{K_{\mathrm{M}}\left(K_{\mathrm{I}}+\frac{4}{3}\mu_{\mathrm{M}}\right)-\frac{4}{3}\mu_{\mathrm{M}}\phi\left(K_{\mathrm{M}}-K_{\mathrm{I}}\right)}{\left(K_{\mathrm{I}}+\frac{4}{3}\mu_{\mathrm{M}}\right)+\phi\left(K_{\mathrm{M}}-K_{\mathrm{I}}\right)}. \qquad (3.38)$$

The expression in Eq. (3.38) is identical to the effective bulk modulus derived from the Hashin-Shtrikman bounds in linear elasticity and is restricted to values that range from K_{M} and K_{I} as the volume fraction spans 0 to 1 [85]. The bounds are obtained by assuming that each material in the composite has positive stiffness, and the overall effective medium is therefore stable when unconstrained. However, since it has been show that it is possible to achieve

a stable composite by constraining the SAMM inclusions within the negative stiffness regime, the effective bulk modulus given by Eq. (3.38) may fall outside the expected Hashin-Shtrikman bounds, providing enhanced stiffness [6].

By equating all terms at second order, it is found that the effective modulus K'_* is given by

$$K'_* = \frac{7}{3}K_* - \frac{(7K_\mathrm{I} - 3K'_\mathrm{I})\left(K_\mathrm{M} + \frac{4}{3}\mu_\mathrm{M}\right)\left[\phi\left(K_* + \frac{4}{3}\mu_\mathrm{M}\right) + (K_\mathrm{M} - K_*)\right]}{3\left[\phi\left(K_\mathrm{M} - K_\mathrm{I}\right) + \left(K_\mathrm{I} + \frac{4}{3}\mu_\mathrm{M}\right)\right]^2}. \quad (3.39)$$

Similarly, the third order effective modulus is

$$\begin{aligned} K''_* = 5K'_* - \frac{8}{3}K_* - \frac{(1-\phi)(7K_* - 3K'_*)\left(K_\mathrm{M} + \frac{4}{3}\mu_\mathrm{M}\right)(7K_\mathrm{I} - 3K'_\mathrm{I})}{3\left[\phi\left(K_\mathrm{M} - K_\mathrm{I}\right) + \left(K_\mathrm{I} + \frac{4}{3}\mu_\mathrm{M}\right)\right]^2} \\ + \frac{(8K_\mathrm{I} - 15K'_\mathrm{I} + 3K''_\mathrm{I})\left(K_\mathrm{M} + \frac{4}{3}\mu_\mathrm{M}\right)^2\left[\phi\left(K_* + \frac{4}{3}\mu_\mathrm{M}\right) + K_\mathrm{M} - K_*\right]}{3\left[\phi\left(K_\mathrm{M} - K_\mathrm{I}\right) + \left(K_\mathrm{I} + \frac{4}{3}\mu_\mathrm{M}\right)\right]^3}. \end{aligned} \quad (3.40)$$

Because the constitutive relationships for the SAMM inclusion and effective medium have the same form, the acoustic nonlinearities, $(B/A)_*$ and $(C/A)_*$, are similar to those shown in Eqs. (3.8) and (3.9):

$$\left(\frac{B}{A}\right)_* = \frac{K'_*}{K_*} - 2 \quad (3.41)$$

and

$$\left(\frac{C}{A}\right)_* = \frac{K''_*}{K_*} - 6\frac{K'_*}{K_*} + 6. \quad (3.42)$$

3.2.2.2 Nonlinear Hashin-Shtrikman Homogenization Results

The effective bulk modulus and nonlinearity parameters are plotted in Figs. 3.7–3.9 comparing the response for an effective medium containing

$\phi = 1\%$ SAMM inclusions embedded in an elastic matrix with bulk modulus $K_{\text{M}} = 2$ GPa and four different Poisson's ratios: $\nu_{\text{M}} = 0.5$, $\nu = 0.4995$, $\nu_{\text{M}} = 0.4991$, and $\nu_{\text{M}} = 0.4989$. The values are obtained by first finding the effective stiffness moduli, K_*, K'_*, and K''_*, given by Eqs. (3.38)–(3.40). The effective parameters depend on the local SAMM inclusion linear and nonlinear stiffness moduli, K_{I}, K'_{I}, and K''_{I}, given in Figs. 2.8–2.10. Then, K_*, K'_*, and K''_*, which are functions of the imposed microscopic pre-strain, are used in Eqs. (3.41) and (3.42).

In Figs. 3.7–3.9, the intersection of the black dashed lines correspond to the location of the essential nonlinearities of an unconstrained SAMM inclusion and the area within the two vertical black dashed lines represents the locally negative stiffness regime on the microscale. The blue curves represent the limit of no shear stress. For that case, the effective parameters of nonlinearity and bulk modulus approximated by the mixture law shown in Figs. 3.5–3.3 are very similar to their analogous coefficients determined with the Hashin-Shtrikman approach, but they are not identical. The difference is anticipated because the mixture law is equivalent to the Reuss bound, which is derived by assuming equality of stress in all constituent materials. The Reuss bound is known to underestimate the effective bulk modulus when compared to the Hashin-Shtrikman method and therefore, it is expected that the computed values of $(B/A)_*$ and $(C/A)_*$ differ between the two methods.

The green lines represent a Poisson's ratio of $\nu_{\text{M}} = 0.4995$, which corresponds to $\mu_{\text{M}} = 1.9$ MPa. K_* still becomes negative for some values when

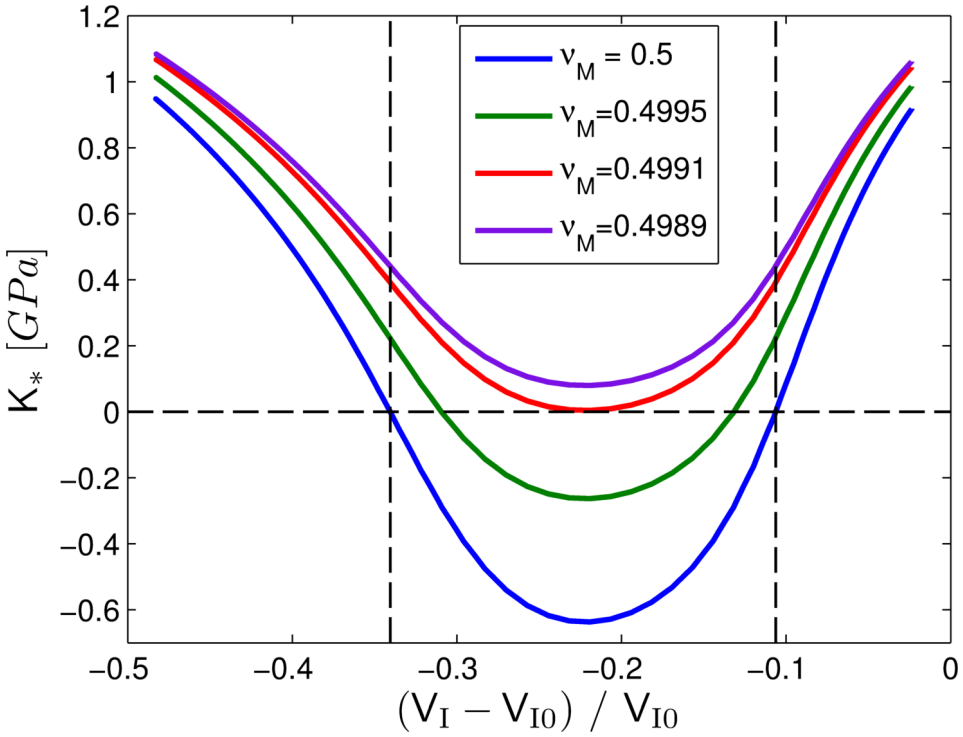

Figure 3.7: K_* derived from the Hashin-Shtrikman approach with $\phi = 1\%$ SAMM inclusions for $K_{\text{M}} = 2$ GPa and $\nu_{\text{M}} = 0.5$, $\nu = 0.4995$, $\nu_{\text{M}} = 0.4991$, and $\nu_{\text{M}} = 0.4989$.

K_{I} is negative, as shown in Fig. 3.7, but there are also positive values of K_* when K_{I} is negative. The positive values of K_* between the two vertical black dashed lines indicate that the matrix is capable of constraining the representative SAMM inclusion with negative stiffness behavior for some, but not all, microscopic pre-strains. Decreasing the Poisson's ratio to $\nu_{\text{M}} = 0.4991$ increases the shear modulus to $\mu_{\text{M}} = 3.7$ MPa, as denoted by the red lines. The matrix is now stiff enough to constrain the SAMM inclusion within the entire microscopic negative stiffness regime. Therefore, the effective bulk modulus

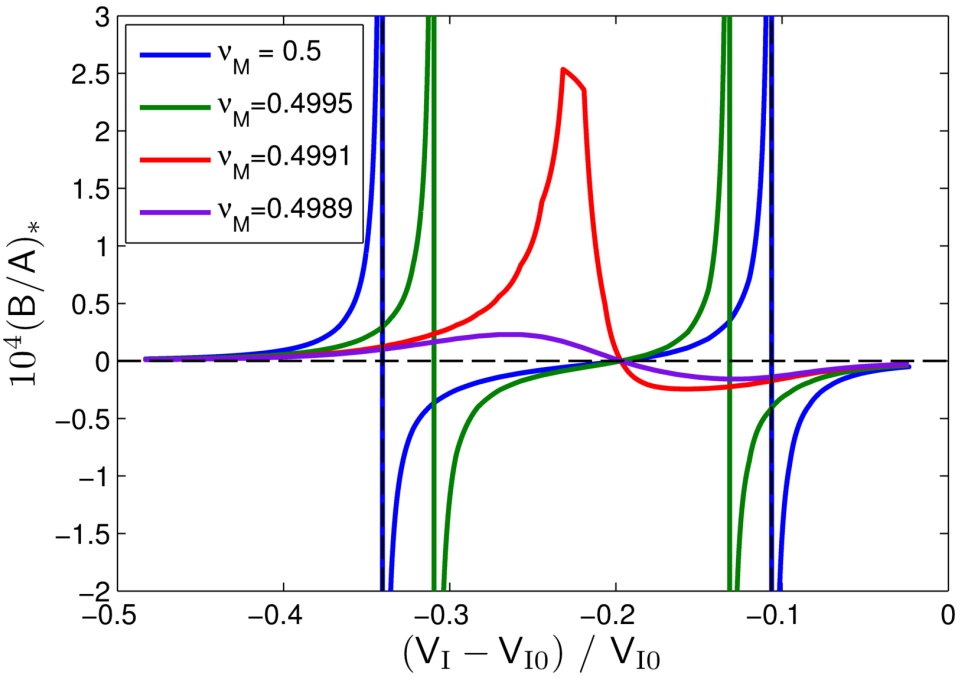

Figure 3.8: $(B/A)_*$ derived from the Hashin-Shtrikman approach with $\phi = 1\%$ SAMM inclusions for $K_{\text{M}} = 2$ GPa and $\nu_{\text{M}} = 0.5$, $\nu = 0.4995$, $\nu_{\text{M}} = 0.4991$, and $\nu_{\text{M}} = 0.4989$.

given by the red curve in Fig. 3.7 is always positive and the effective medium will be stable over all ranges of inclusion pre-strain. The value $\nu_{\text{M}} = 0.4991$ represents a threshold for which the Poisson's ratio is small enough to obtain $K_* > 0$ for all pre-strains. Further decreasing the Poisson's ratio to $\nu_{\text{M}} = 0.4989$, which corresponds to $\mu_{\text{M}} = 4.3$ MPa, causes the minimum values of K_* to shift upwards. This is shown via the purple curve.

Computed values of $(B/A)_*$ for the same four Poisson's ratios are plotted as a function of SAMM inclusion pre-strain in Fig. 3.8, while values of $(C/A)_*$ are shown in Fig. 3.9. Both effective parameters of nonlinearity can

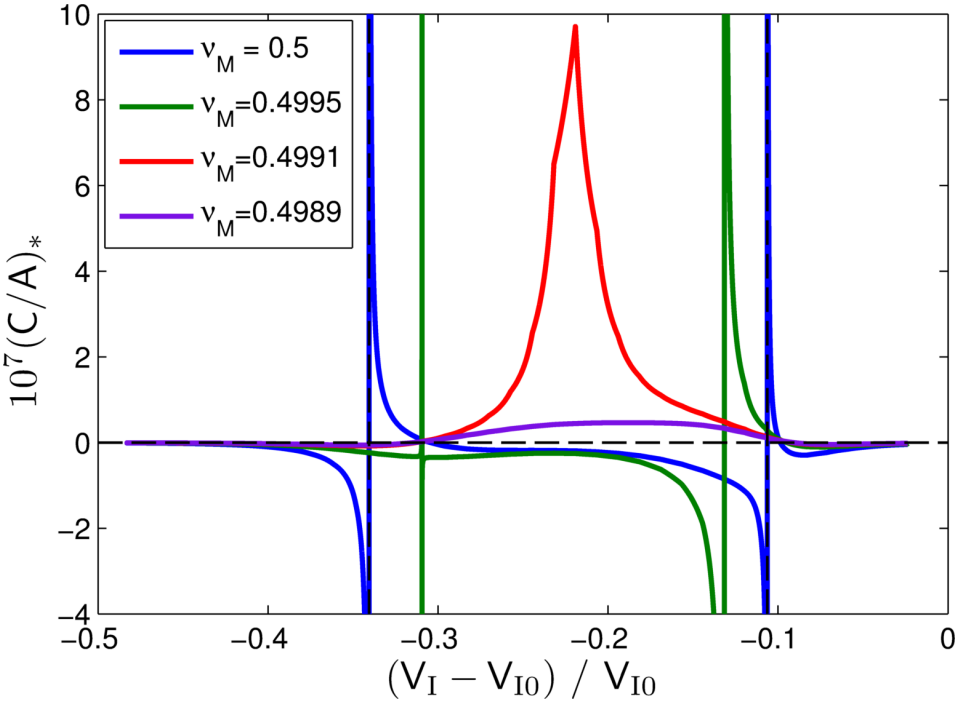

Figure 3.9: $(C/A)_*$ derived from the Hashin-Shtrikman approach with $\phi = 1\%$ SAMM inclusions for $K_{\text{M}} = 2$ GPa and $\nu_{\text{M}} = 0.5$, $\nu = 0.4995$, $\nu_{\text{M}} = 0.4991$, and $\nu_{\text{M}} = 0.4989$.

attain positive and negative values. The blue and green curves, corresponding to $\nu_{\text{M}} = 0.5$ and $\nu_{\text{M}} = 0.4995$, respectively, become very large, approaching positive or negative infinity as the pre-strain approaches values when $K_* = 0$. For $\nu_{\text{M}} = 0.5$, the asymptotic behavior occurs at the essential nonlinearities of the SAMM inclusion, as described in Section 3.2.1.2. However, when the SAMM inclusion is in the negative stiffness regime, the essential nonlinearities of K_* shift towards each other until the shear modulus is large enough to constrain the SAMM inclusion for any pre-strain. The behavior results from the fact that $(B/A)_*$ and $(C/A)_*$ are proportional to K_*^{-1} as shown in

Eqs. (3.41) and (3.42), respectively. The pre-strains for which the parameters of nonlinearity become very large differ for $\nu_{\mathrm{M}} = 0.5$ and $\nu_{\mathrm{M}} = 0.4995$, and thus the larger magnitudes of $(B/A)_*$ and $(C/A)_*$ correspond to the essential nonlinearity of the effective medium. As the Poisson's ratio becomes large enough to constrain the entire negative stiffness regime of the SAMM inclusion, the ratio $(B/A)_*$ becomes bounded, as indicated by the red curve, for $\nu_{\mathrm{M}} = 0.4991$, and the purple curve, with $\nu_{\mathrm{M}} = 0.4989$ in Fig. 3.8. The peak magnitude of $(B/A)_*$ therefore decreases for decreasing Poisson's ratio. A similar boundedness for $(C/A)_*$ is apparent in Fig. 3.9. This is a prime example of the ability to tune the response of the SAMM inclusion. The values of ν_{M} required to stably constrain the entire microscopic, negative stiffness regime will vary depending on the material properties and geometry of the SAMM inclusion. The microstructure can therefore be optimally designed to achieve large nonlinearity for a specific matrix material.

Figure 3.10, which shows the ratio $(C/B)_*$ for the same four Poisson's ratios versus the microscopic volumetric strain, clearly illustrates the significance of the cubic nonlinearity in comparison with the quadratic nonlinearity. The three curves are very similar and become nearly identical for some pre-strains while diverging for others. It is worth noting that the vertical lines near $\varepsilon_{v\mathrm{I}} = -0.2$ that correspond to $(C/B)_*$ asymptotically approaching positive or negative infinity also occur at this volumetric strain for $(C/B)_*^{\mathrm{ML}}$ in Fig. 3.4. This volumetric strain corresponds to the location of the local minima in both the microscopic and macroscopic stiffness curves, which clearly occurs at the

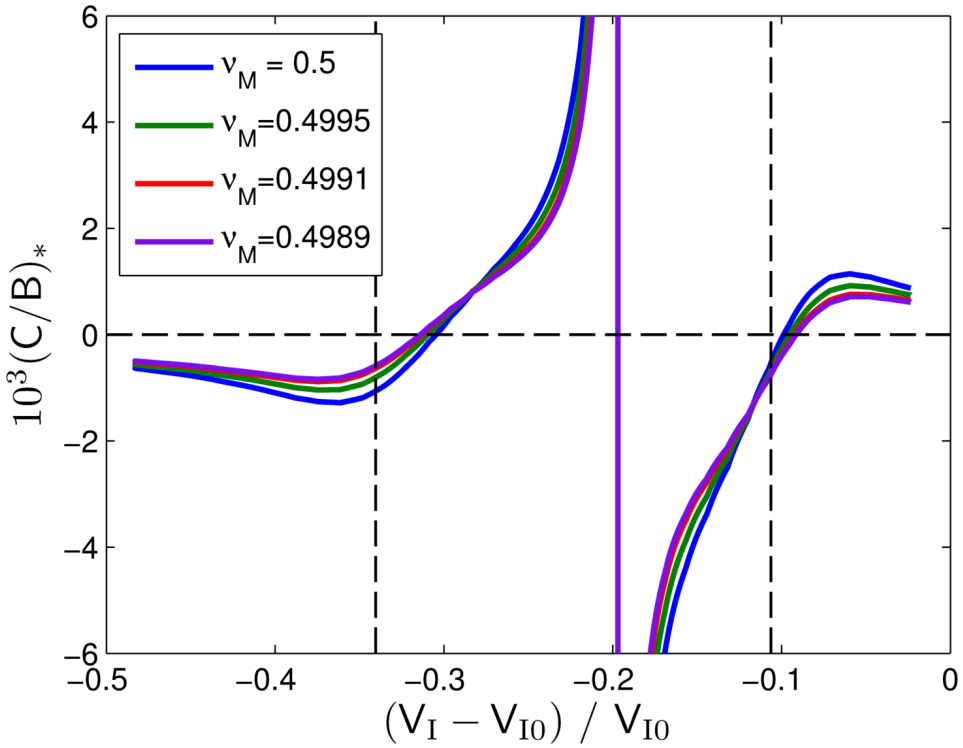

Figure 3.10: $(C/B)_*$ derived from the Hashin-Shtrikman approach with $\phi = 1\%$ SAMM inclusions for $K_M = 2$ GPa and $\nu_M = 0.5$, $\nu = 0.4995$, $\nu_M = 0.4991$, and $\nu_M = 0.4989$.

same microscopic pre-strain regardless of the properties of the surrounding matrix. Therefore, when the matrix is stiff enough to stably constrain the SAMM inclusion, the cubic nonlinearity for the effective medium are much more significant than the cubic nonlinearity for the conventional material presented in Table 3.1.

3.3 Nonlinear Macroscopic Behavior

In the previous section, the macroscopic parameters of nonlinearity were expressed as a function of change in volume on the microscale. The macroscopic strain is highly contingent upon its constituents and by instead using the microscopic strain, the previous analysis allows both homogenization methods to be compared on the same scale. However, the strain magnitudes on the macroscale are of interest to describe the overall effective behavior of the heterogeneous medium. In Section 2.2 it was found that the volumetric strain and coefficient 'a_{I}' for the SAMM inclusion are related via the expression $\varepsilon_{v\text{I}} = 3a_{\text{I}} + \frac{9}{2}a_{\text{I}}^2$. Since the constitutive relationship for the effective medium is of the same form as the SAMM inclusion, the volumetric strain, ε_{v_*}, and coefficient, a_*, on the macroscale will obey the same relation, $\varepsilon_{v_*} = 3a_* + \frac{9}{2}a_*^2$.

Through the method of recursive substitution used to derive the state equations in Section 3.1.1, one finds

$$a_{\text{I}} = \frac{1}{3}\left(\varepsilon_{v\text{I}} - \frac{1}{2}\varepsilon_{v\text{I}}^2 + \frac{1}{2}\varepsilon_{v\text{I}}^3\right), \tag{3.43}$$

where terms are retained only up to third order with respect to $\varepsilon_{v\text{I}}$. An expression for a_{M} is obtained as a function of $\varepsilon_{v\text{I}}$ and the inclusion and matrix elastic constants, all of which are known quantities, by following the same derivation from Section 3.2.2.1. This function of a_{M} is substituted into Eq. (3.31) to obtain an expression for a_* in terms of known parameters. Using the relation $\varepsilon_{v_*} = 3a_* + \frac{9}{2}a_*^2$, the macroscopic volumetric strain to third order in $\varepsilon_{v\text{I}}$ is found

to be

$$\begin{aligned}\varepsilon_{v*} = (3K_{\mathrm{M}} + 4\mu_{\mathrm{M}})^{-2} \Bigg\{ & \left[3\phi\left(K_{\mathrm{M}} - K_{\mathrm{I}}\right) + 3K_{\mathrm{I}} + 4\mu_{\mathrm{M}}\right](3K_{\mathrm{M}} + 4\mu_{\mathrm{M}})\,\varepsilon_{v\mathrm{I}} \\ & + \frac{1}{2}\Big\{ \left[\phi\left(3K_{\mathrm{I}}' - 4K_{\mathrm{I}} - 3K_{\mathrm{M}}\right) - K_{\mathrm{I}}' + 4K_{\mathrm{I}} - 4\mu_{\mathrm{M}}\right](3K_{\mathrm{M}} + 3\mu_{\mathrm{M}}) \\ & \qquad + \left[3\phi\left(K_{\mathrm{M}} - K_{\mathrm{I}}\right) + 3K_{\mathrm{I}} + 4\mu_{\mathrm{M}}\right]^2 \Big\}\varepsilon_{v\mathrm{I}}^2 \\ & + \frac{1}{6}\Big\{ \left[3\phi\left(3K_{\mathrm{I}} + 4K_{\mathrm{I}} - 3K_{\mathrm{M}}\right) + K_{\mathrm{I}}^2 - 4K_{\mathrm{I}} + 4\mu_{\mathrm{M}}\right]\left[3\phi\left(K_{\mathrm{M}} - K_{\mathrm{I}}\right)\right. \\ & \qquad \left. +3K_{\mathrm{I}} + 4\mu_{\mathrm{M}}\right] + \left[\phi\left(9K_{\mathrm{M}} - 3K_{\mathrm{I}}'' + 6K_{\mathrm{I}} - 4K_{\mathrm{I}}\right)\right. \\ & \qquad \left. + 3K_{\mathrm{I}}'' + 6K_{\mathrm{I}}'' + 4K_{\mathrm{I}}' + 12\mu_{\mathrm{M}}\right](3K_{\mathrm{M}} + 4\mu_{\mathrm{M}}) \Big\}\varepsilon_{v\mathrm{I}}^3 \Bigg\}. \end{aligned} \tag{3.44}$$

As expected, the effective volumetric strain depends on the constitutive properties of the matrix, as well as local coefficients that describe the SAMM inclusion for each pre-strain. The overall constitutive curve for the effective medium is described using an equation equivalent to Eq. (2.22) that instead describes the macroscale,

$$P_* = P_{*0} - K_*\left(\varepsilon_{v*} - \bar{\varepsilon}_{v*}\right) + \frac{1}{2}K_*'\left(\varepsilon_{v*} - \bar{\varepsilon}_{v*}\right)^2 - \frac{1}{6}K_*''\left(\varepsilon_{v*} - \bar{\varepsilon}_{v*}\right)^3. \tag{3.45}$$

Similar to the microscale response, there exists a pre-strain that is imposed on the heterogeneous material, denoted by $\bar{\varepsilon}_{v*}$, due to an external hydrostatic pressure, P_*. The value of $\bar{\varepsilon}_{v*}$ is obtained form Eq. (3.44) by replacing $\varepsilon_{v\mathrm{I}}$ with $\bar{\varepsilon}_{v\mathrm{I}}$.

An overall constitutive curve for the macroscopic response of the heterogeneous medium can be constructed from Eq. (3.45). Figure 3.11 shows the macroscopic response predicted for the same four values of Poisson's ratio considered in Section 3.2.2.2: $\nu = 0.5$, $\nu = 0.4995$, $\nu = 0.4991$, and $\nu = 0.4989$,

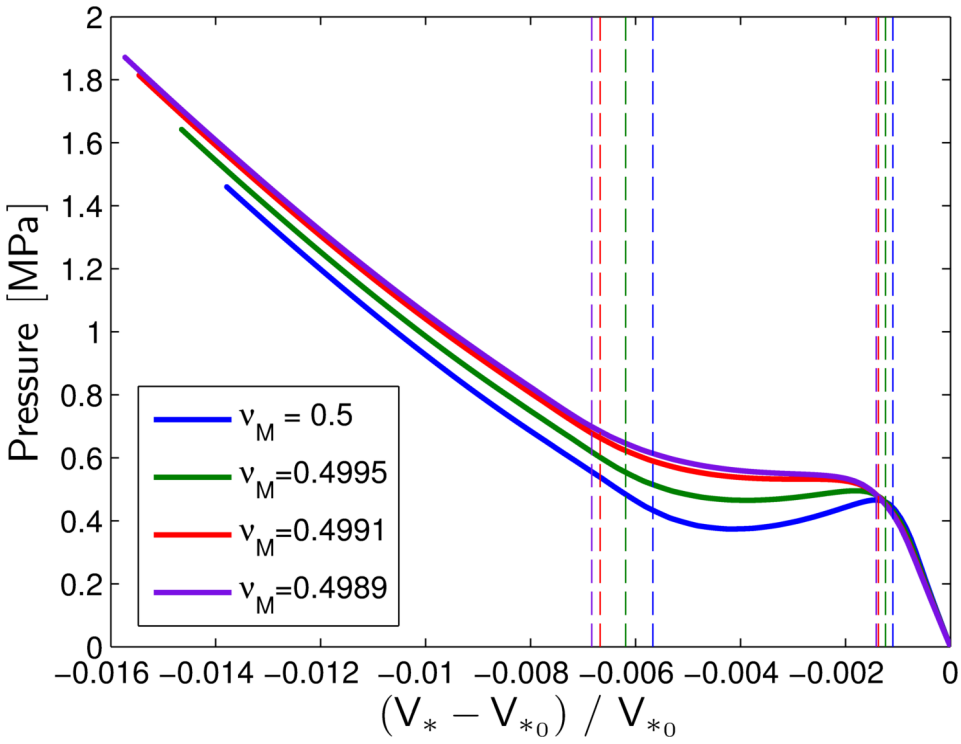

Figure 3.11: Pressure-volume relationship for the overall macroscopic response as a function of the local perturbations on the microscale with $\phi = 1\%$ SAMM inclusions for $K_{\text{M}} = 2$ GPa and $\nu_{\text{M}} = 0.5$, $\nu = 0.4995$, $\nu_{\text{M}} = 0.4991$, and $\nu_{\text{M}} = 0.4989$.

which are shown in blue, green, red and purple, respectively. The region between the two vertical dashed lines of the same color indicate the microscopic negative stiffness regime of the SAMM inclusion for the constitutive curve of the same color. Near zero strain, the four curves appear very similar; all four are very linear and the differences between them are nearly indistinguishable on this scale. The response is more clearly seen in Fig. 3.12, which zooms in to show the pressure-volume relationship near zero strain. There is a visible, albeit marginal, difference in the slopes of the four curves. The blue curve is

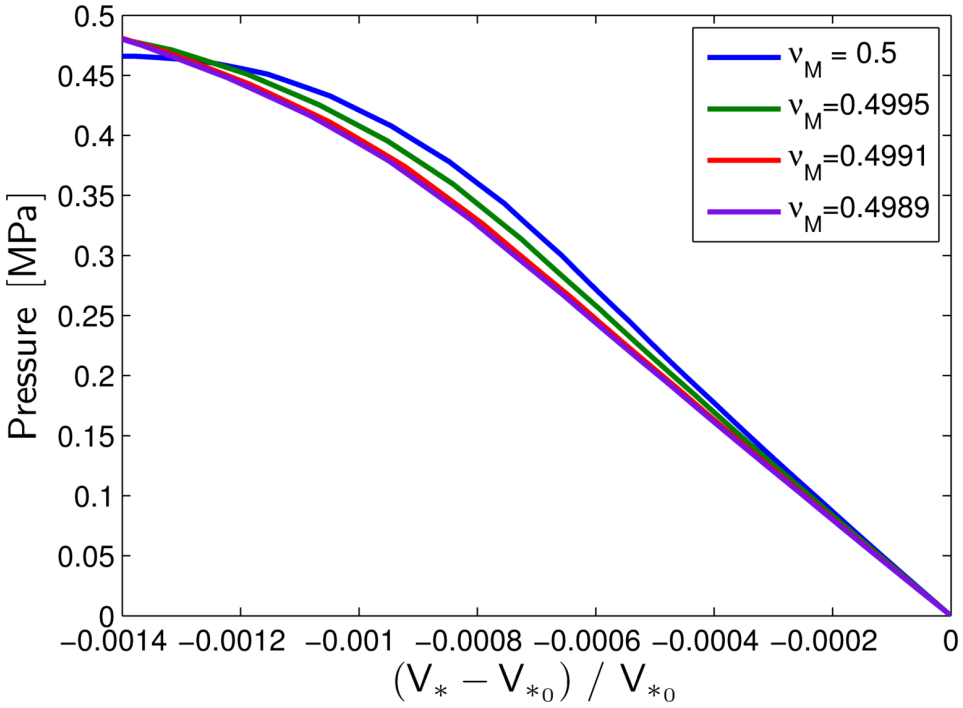

Figure 3.12: Pressure-volume relationship near zero strain for the overall macroscopic response as a function of the local perturbations on the microscale with $\phi = 1\%$ SAMM inclusions for $K_{\text{M}} = 2$ GPa and $\nu_{\text{M}} = 0.5$, $\nu = 0.4995$, $\nu_{\text{M}} = 0.4991$, and $\nu_{\text{M}} = 0.4989$.

the steepest, representing a matrix with $\nu_{\text{M}} = 0.5$. Although it is the softest matrix material considered here, the response becomes nonlinear more quickly than for the matrix materials with smaller Poisson's ratio, as evident by the curvature of the blue curve in Fig. 3.12. The cause is the larger magnitudes of the nonlinear terms for $\nu_{\text{M}} = 0.5$ than for the other three Poisson's ratios when considering the same volumetric strain, as demonstrated by $(B/A)_*$ and $(C/A)_*$ in Figs. 3.8 and 3.9, respectively. The larger nonlinearities, therefore, contribute to the steeper slope near zero strain even though the effective

medium is the least stiff. The purple curve for $\nu_{\text{M}} = 0.4989$ has the least steep slope, but remains linear over a larger range of strain values due to the smaller magnitudes of the nonlinear terms. The red curve, for $\nu_{\text{M}} = 0.4991$ is only slightly more steep than the purple curve. The green curve, for $\nu_{\text{M}} = 0.4995$, falls within the blue and red curves.

The four curves diverge more rapidly as the strain magnitudes increase, as evident in Fig. 3.12. The blue curve shows the highest degree of non-monotonicity, corresponding to a negative stiffness regime on the macroscale that cannot constrain the SAMM inclusions. The green curve is also non-monotonic with a range of macroscopic strain where the response displays negative stiffness. The red and purple curves, however, are monotonic because the matrix fully constrains the SAMM inclusions within the negative stiffness regime. The behavior displayed in Fig. 3.11 is consistent with that described in Section 3.2.2.2. It is also important to note that for larger strain magnitudes, the response of the effective medium is once again linear, but with reduced stiffness for all four Poisson's ratios when compared to the behavior near the zero pre-strain configuration.

The magnitudes of the strain for the effective medium in Fig. 3.11 are more than an order of magnitude smaller than those of a single SAMM inclusion shown in Figs. 3.7–3.9. For the matrix with $\nu = 0.4989$, the former peaks at $\varepsilon_{v_*} \sim -0.016$, while the latter peaks at $\varepsilon_{v\text{I}} \sim -0.5$. The difference in magnitudes indicates that the macroscopic strain necessary to induce a cubically nonlinear response on the microscale is not that large. For the

representative SAMM inclusion constrained in a matrix with $\nu = 0.4989$, it is less than -1.6%, where the negative stiffness regime for the SAMM inclusion occurring for a macroscopic strain range of less than -1%. Therefore, it is reasonable to be able to physically induce the increased nonlinear response in a heterogeneous medium that contains SAMM inclusions.

3.3.1 Comparison with Conventional Materials

Ashby charts are used in mechanical design for material selection because they provide a direct comparison of materials for a desired property space. The charts are scatter plots for wide a range of materials, e.g. metals, polymers, and composites, with two different properties, such as stiffness and density, represented by the two axes. The material maps are adopted in the present work for presentation of the acoustic nonlinearities as a function of stiffness. Figures 3.13 and 3.14 are Ashby charts for $|B/A|$ and $|C/A|$, respectively, plotted on a log-log scale as a function of stiffness. The $|B/A|$ and $|C/A|$ values for the conventional materials—organic and biological media, pyrex glass, fused silica, rock, and bubbly liquids—are obtained from Table 3.1 and are represented by the solid circles. From Section 3.2.2.2, the magnitude and sign of B/A and C/A for composites containing SAMM inclusions can vary drastically. Representative values of the nonlinearity parameters, denoted with $\times$, are taken from the curves in Figs. 3.8 and 3.9 for $\nu_{\text{M}} = 0.4991$. The positive values of B/A or C/A are shown in black, while the negative values are in red. It is worth emphasizing that both the sign and the magnitude

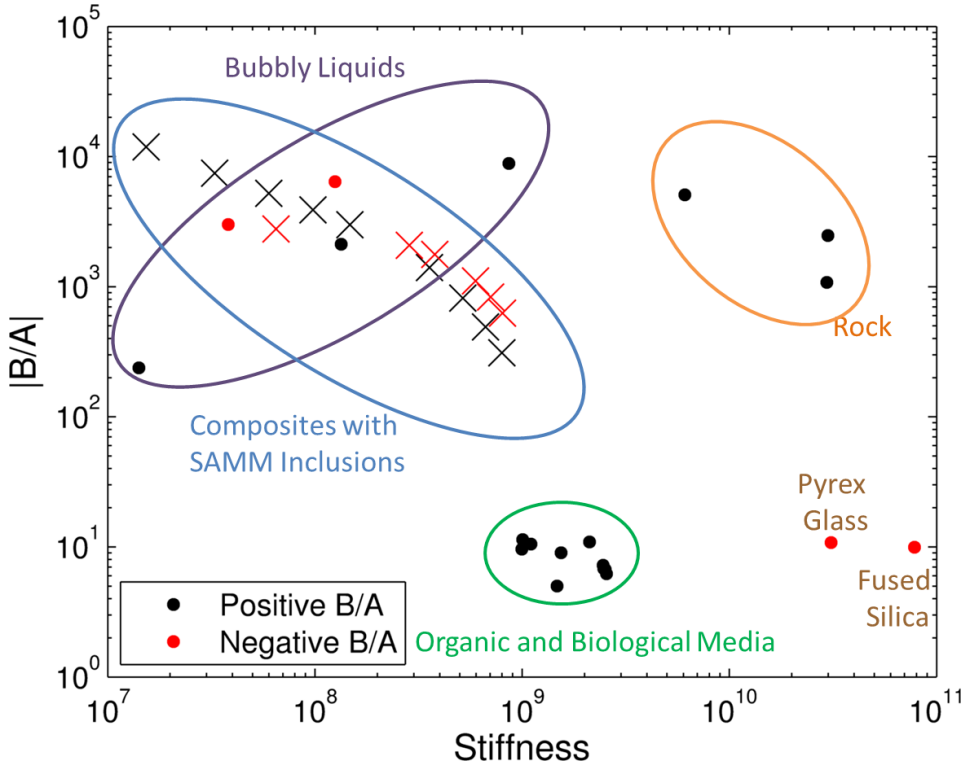

Figure 3.13: Ashby plot for various $|B/A|$ parameters.

of the parameters of nonlinearity and the corresponding stiffness magnitudes rely heavily on the properties of the matrix and the inclusion. Therefore, a wide range of effective properties may be achievable by considering various matrix or inclusion materials. The composites with SAMM inclusions shown in Figs. 3.8 and 3.9 represent one limited example.

For the example, the stiffness and quadratic nonlinearity associated with the SAMM inclusions are very similar to those of the bubbly liquids as illustrated by the overlapping regions of interest in Fig. 3.13. However, the gas bubbles have a finite life span and are unstable [88]. On the other hand,

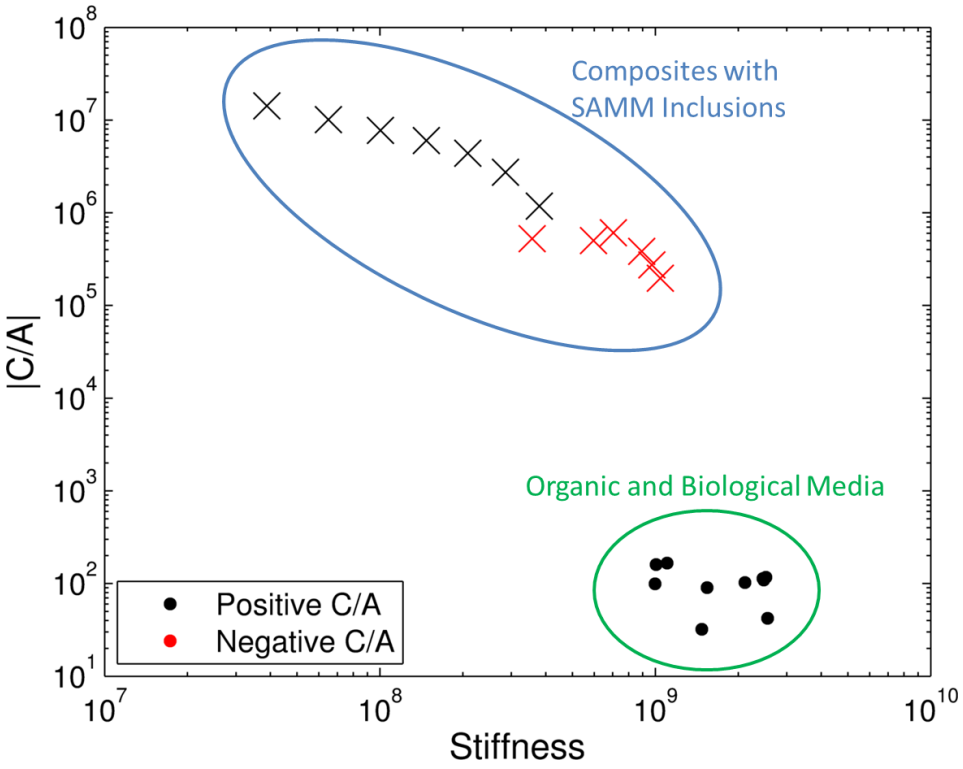

Figure 3.14: Ashby plot for various $|C/A|$ parameters.

the heterogeneous material with SAMM inclusions can be stabilized and offer the ability to tune the system for a desired response.

The significance of the cubic nonlinearities are highly apparent in Fig. 3.14 because there are so few measurements of C/A in conventional materials. Although the example composite containing SAMM inclusions is not as stiff as the organic and biological media in the strain range where cubic nonlinearities are prominent, the magnitude of the parameter C/A is increased by 3 to 5 orders of magnitude. Tuning the initial SAMM inclusion behavior may lead to a stiffer composite that still possess enhanced nonlinearities. Further-

more, the values of C/A can also be negative, which the author has yet to find reported in the limited literature that discusses values of C/A.

3.4 Propagation Model

A wave equation that accounts for cubic nonlinearities is necessary to model propagation in the heterogeneous media of interest. A lossless form of the wave equation that accounts for both quadratic and cubic nonlinearity is found in [89]. For a lossy medium, the terms accounting for absorption are the same as for the Westervelt equation. The one-dimensional wave equation for plane, progressive waves that accounts for viscous loss, and quadratic and cubic nonlinearity is therefore given by

$$\frac{\partial^2 p}{\partial x^2} - \frac{1}{c_0^2}\frac{\partial^2 p}{\partial t^2} = -\frac{\delta}{c_0^4}\frac{\partial^3 p}{\partial t^3} - \frac{\beta}{\rho_0 c_0^4}\frac{\partial^2 p^2}{\partial t^2} - \frac{2\gamma}{3\rho_0^2 c_0^6}\frac{\partial^2 p^3}{\partial t^2}, \tag{3.46}$$

where δ is the diffusivity of sound, and β and γ are defined in Eqs. (3.10) and (3.12). The derivation of Eq. (3.46) is provided in Appendix A.1.

3.4.1 Evolution Equation

It is also useful to derive a one dimensional evolution equation for progressive waves similar to the Burgers equation, but that accounts for cubic nonlinearity. In nonlinear acoustics, small terms are additive at leading order, and thus the evolution equation desired can be expressed as three separate differential equations, one corresponding to each term on the right-hand side of Eq. (3.46). All three equations have the d'Alembertian operator on the

left-hand side [3]. The evolution equation is derived by introducing a retarded time frame, $\tau = t - x/c_0$, where the coordinate frame now moves with the evolving wave. Only terms at the lowest order, as determined by transforming the x-coordinate to a slow scale corresponding to τ, for each respective equation is retained. See Appendix A.2 for the derivation of the following three separate evolution equations.

The evolution equation for a lossy, linear wave equation characterizing thermoviscous absorption is given by [90]

$$\frac{\partial p}{\partial x} = \frac{\delta}{2c_0^3}\frac{\partial^2 p}{\partial \tau^2}. \tag{3.47}$$

The diffusivity of sound, δ, is related to the thermoviscous attenuation coefficient, α, through the relation $\alpha = \delta\omega^2/2c_0^3$.

The evolution equation accounting for quadratic nonlinearity is [90]

$$\frac{\partial p}{\partial x} = \frac{\beta p}{\rho_0 c_0^3}\frac{\partial p}{\partial \tau}. \tag{3.48}$$

Including both the effects of thermoviscous absorption and quadratic nonlinearity in the derivation of an evolution equation yields the well known Burgers equation.

The evolution equation involving only cubic nonlinearity is [71]

$$\frac{\partial p}{\partial x} = \frac{\gamma p^2}{\rho_0^2 c_0^5}\frac{\partial p}{\partial \tau}. \tag{3.49}$$

Since the time scale is the same for each of the three separate evolution equations, the right-hand sides of Eqs. (3.47), (3.48) and (3.49) are added together

to create one evolution that can be equation used to model the combined effects of absorption and quadratic and cubic nonlinearity on the propagation of plane progressive waves:

$$\frac{\partial p}{\partial x} = \frac{\delta}{2c_0^3}\frac{\partial^2 p}{\partial \tau^2} + \left(\frac{\beta p}{\rho_0 c_0^3} + \frac{\gamma p^2}{\rho_0^2 c_0^5}\right)\frac{\partial p}{\partial \tau}. \tag{3.50}$$

Higher orders of nonlinearity (quartic, etc.) in the equation of state appear simply as higher powers of p within the parentheses. In the absence of losses, for any order of nonlinearity, the resulting simple wave is described by an augmented form of the Poisson solution.

3.4.2 Shock Formation Distance

The shock formation distance is the location where a vertical tangent first forms in a finite-amplitude wave propagating in a lossless fluid [3]. The infinite vertical tangent is expressed mathematically by $\partial p/\partial \tau = \infty$. The shock formation distance can be found using the following form of the Poisson solution:

$$p = f\left(\tau - \frac{\beta x p}{\rho_0 c_0^3} - \frac{\gamma x p^2}{\rho_0^2 c_0^5}\right). \tag{3.51}$$

The derivative of Eq. (3.51) with respect to retarded time is

$$\frac{\partial p}{\partial \tau} = \frac{f' \rho_0 c_0^3}{\rho_0 c_0^3 - x\left(\beta f' + \dfrac{2\gamma f f'}{\rho_0 c_0^2}\right)}, \tag{3.52}$$

where f' is the derivative of f with respect to its argument. A vertical tangent occurs at the location x for which the denominator equals zero, and thus

$$x = \frac{\rho_0 c_0^3}{\beta f' + \dfrac{2\gamma f f'}{\rho_0 c_0^2}}. \tag{3.53}$$

Depending on the source waveform f, different parts of the distorted waveform may develop a vertical tangent at different locations. The shock formation distance, $\bar{x}$, is defined to be the location of the first vertical tangent, which occurs when the denominator of Eq. (3.53) is at a maximum:

$$\bar{x} = \frac{\rho_0 c_0^3}{\left(\beta f' + \dfrac{2\gamma f f'}{\rho_0 c_0^2}\right)_{\max}}. \tag{3.54}$$

For illustration we calculate the shock formation distance of an initially sinusoidal source waveform, $f = p_0 \sin \omega\tau$. The relations

$$f' = p_0 \omega \cos \omega\tau$$

and

$$f f' = p_0^2 \omega \sin \omega\tau \cos \omega\tau = \frac{1}{2} p_0^2 \omega \sin 2\omega\tau$$

are used in conjunction with Eq. (3.54) to obtain the shock formation distance for a sinusoidal source function given as

$$\bar{x} = \frac{1}{\left[\beta M k \cos \omega\tau + \gamma M^2 k \sin 2\omega\tau\right]_{\max}}. \tag{3.55}$$

Here, $M = p_0/\rho_0 c_0^2$ is the acoustic Mach number and $k = \omega/c_0$ is the wavenumber at the source frequency. The shock formation distance is easily obtained

if either quadratic or cubic nonlinearity is negligible. First consider the case of pure quadratic nonlinearity, which is obtained with $\gamma = 0$. The extrema of the denominator occur for $\omega\tau = n\pi$. If $\beta > 0$, then the maxima occur for all odd multiples of n, and $\bar{x} = 1/\beta Mk$. Conversely, when $\beta < 0$, the denominator is a maximum for all even multiples of n, and thus $\bar{x} = -1/\beta Mk$. Since $\beta < 0$, the shock formation distance is still positive. Thus, for only quadratic nonlinearity,

$$\bar{x}_{\text{quad}} = \frac{1}{|\beta| Mk}. \tag{3.56}$$

Equation (3.56), without the absolute value notation, is the traditional expression for the shock formation distance in fluids. The behavior of an initially sinusoidal waveform at the shock formation distance is shown in Fig. 3.15. The source waveform appears in black and the distorted shape at $x = \bar{x}$ is shown in blue for a purely positive quadratic nonlinearity. At $\omega\tau/2\pi = \pm 1/2$, a vertical tangent appears in the blue curve. If the nonlinearity is negative, the waveform will become multivalued at different $\omega\tau$.

Unlike the case for purely quadratic nonlinearity, a waveform will become multivalued at two points in the waveform (per fundamental cycle) when propagating through a medium with purely cubic nonlinearity. If only cubic nonlinearity is considered, extrema of the denominator of Eq. (3.55) occur at $\omega\tau = \pi\left(2n+1\right)/4$. If $\gamma > 0$, then the denominator is a maximum for all even n, which yields $\bar{x} = 1/\gamma M^2 k$. For $\gamma < 0$, the maximum of the denominator occurs at all odd n, and thus $\bar{x} = -1/\gamma M^2 k$, where $\bar{x}$ is once again still positive.

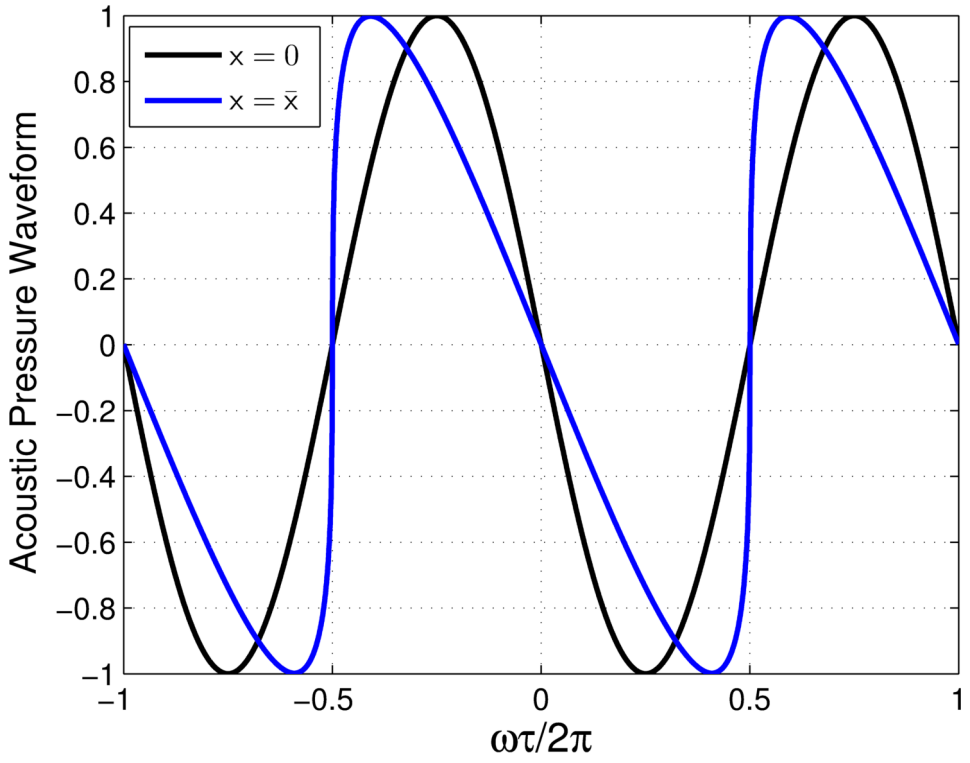

Figure 3.15: The distorted waveform at $x = \bar{x}$ for an initially sinusoidal source waveform due to purely positive quadratic nonlinearity.

Therefore, the shock formation distance for only cubic nonlinearity is

$$\bar{x}_{\text{cubic}} = \frac{1}{|\gamma| M^2 k}. \tag{3.57}$$

An expression similar to Eq. (3.57) appears in Ref. [71] to characterize the shock formation distance of nonlinear shear waves. Figure 3.16 shows the initially sinusoidal source waveform, denoted by the black curve, and the distorted waveform at the shock formation distance due to purely positive cubic nonlinearity. The vertical tangents occur at $\omega\tau/2\pi = (m\pi/4 + 1/2)/2\pi$ for $m = 1, 5, -3, 7$. If the cubic nonlinearity is negative, the two shocks will form

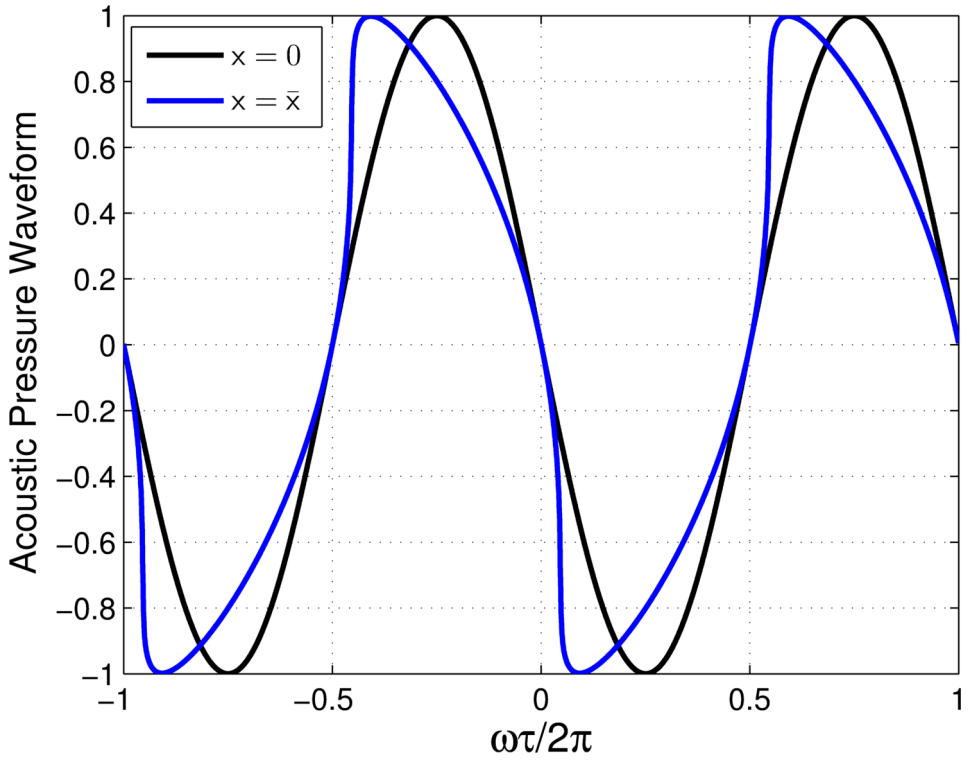

Figure 3.16: The distorted waveform at $x = \bar{x}$ for an initially sinusoidal source waveform due to purely positive cubic nonlinearity.

at different $\omega\tau$.

The expression for the shock formation distance is not as simple as the limiting cases when accounting for both quadratic and cubic nonlinearity. The maximum of the denominator in Eq. (3.55) occurs when the derivative of the expression in the denominator with respect to time is equal to zero:

$$kM\omega\left[-\beta\sin\omega\tau + 2M\gamma\cos 2\omega\tau\right] \equiv 0. \tag{3.58}$$

or

$$\frac{\sin \omega\tau}{\cos 2\omega\tau} = 2\frac{M\gamma}{\beta}. \tag{3.59}$$

Note that the right-hand side of Eq. (3.59) depends upon the ratio of the shock formation distances for the purely cubic and purely quadratic cases, such that

$$\frac{M\gamma}{\beta} = \frac{\bar{x}_{\text{cubic}}}{\bar{x}_{\text{quad}}}. \tag{3.60}$$

Thus, if the right-hand side of Eq. (3.59) is equal to ± 2, then the medium is characterized by equal parts quadratic and cubic nonlinearity.

In Fig. 3.17, the left-hand side of Eq. (3.59) is shown in black and two example values of the right-hand side are plotted, the blue is for $2M\gamma/\beta = 2$ and the red is for $2M\gamma/\beta = -2$. This example therefore corresponds to equal contributions of quadratic and cubic nonlinearity. The blue dashed line, for which $\beta = M\gamma$, corresponds to both positive or both negative nonlinearity, whereas the red dashed line, with $\beta = M\gamma$, represents a positive cubic but negative quadratic nonlinearity, or vice versa. For both of the limiting cases, the maxima occur at every other extrema given by the denominator in Eq. (3.55). The same is true here. Consider first the intercepts between the black curve and blue dashed line, which are labeled 1 though 4 from left to right in blue. The maximum values for the case $\beta = M\gamma$ occur for point 1, where $\omega\tau = -0.3404$ and point 3, where $\omega\tau = 0.101$; the other two points are local minima. The intercepts between the red dashed line and the black curve, which corresponds to $\beta = -M\gamma$, are labeled 1 through 4 in red from left to

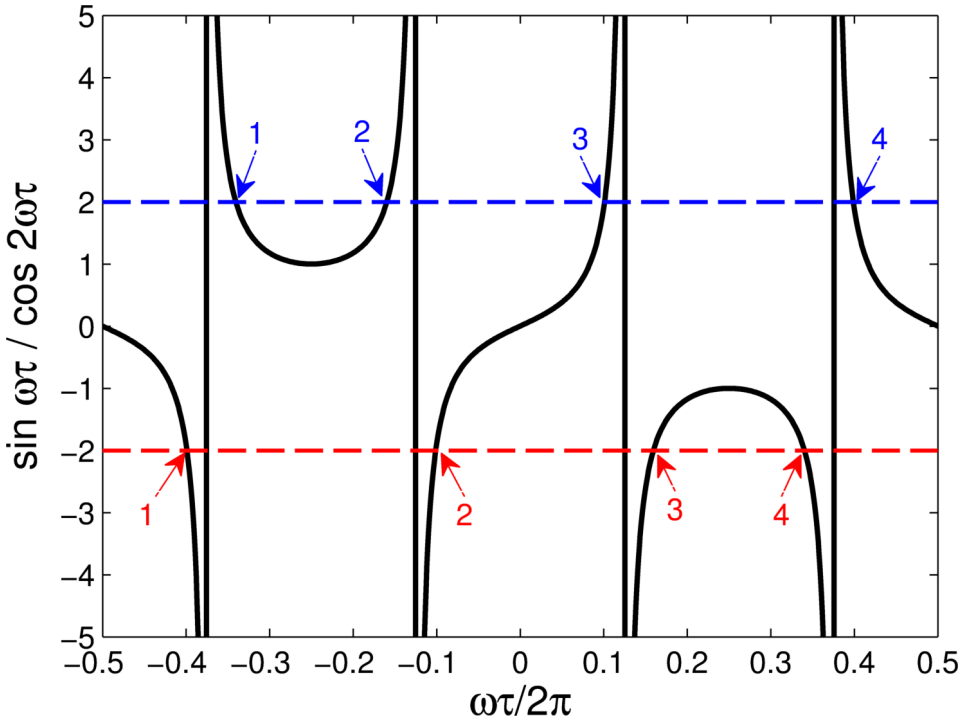

Figure 3.17: The left-hand side of Eq. (3.59) plotted as a function of $\omega\tau$ and two example values of for the right-hand side of Eq. (3.59), $2M\gamma/\beta = \pm 2$.

right. The maximum for this case occur at point 2, for which $\omega\tau = -0.101$, and point 4, where $\omega\tau = 0.3404$.

Because there are two maximum values that satisfy Eq. (3.55), two points on the initially sinusoidal waveform will become multivalued. This was the case for purely cubic nonlinearity. However, unlike the purely cubic nonlinearity case, when the two maximum values obtained from Fig. 3.17 are substituted into Eq. (3.55), two different values of $\bar{x}$ could be obtained. Thus, the two components of the waveform that become multivalued do so at different distances from the source. The shock formation distance refers to the shortest dis-

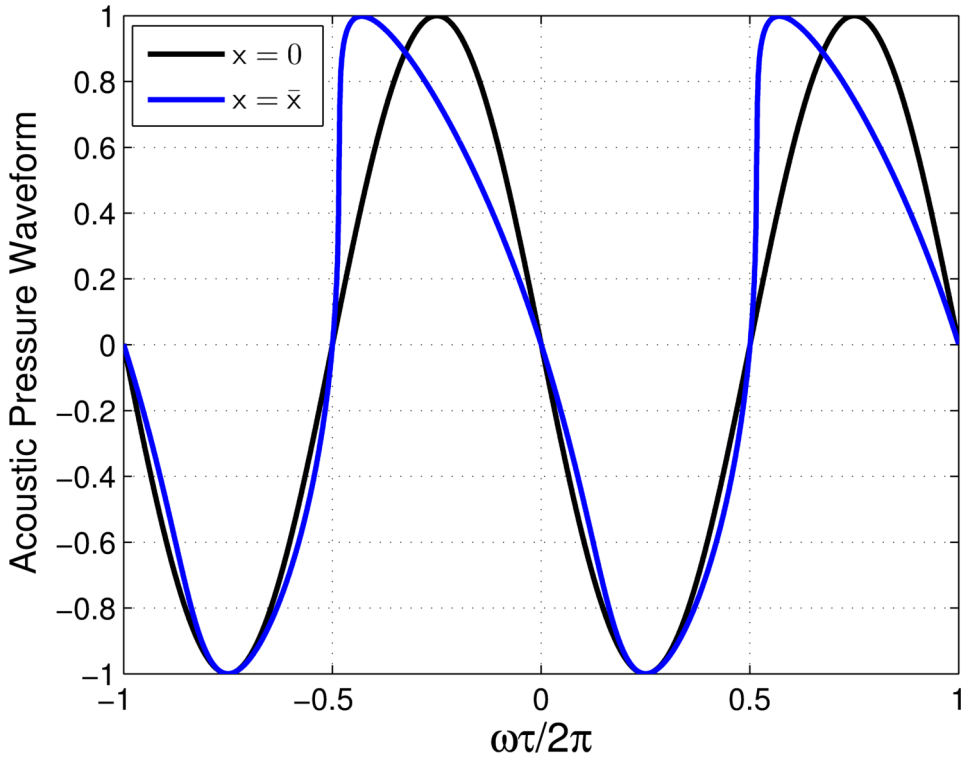

Figure 3.18: The distorted waveform at $x = \bar{x}$ for an initially sinusoidal source waveform due to equal contributions of quadratic and cubic nonlinearity ($\beta = M\gamma$).

tance that will result in a multi-valued waveform. Therefore, for both $\beta = M\gamma$ and $\beta = -M\gamma$, the shock formation distance is given by $\bar{x} = 0.5681/\beta MK$. The second shock is formed at distance $\bar{x}_2 = 2.710/\beta Mk = 4.77\bar{x}$. Figure 3.18 shows the behavior of the mixed order nonlinearity given by the blue dashed line in Fig. 3.17. Only one point on the waveform (per fundamental cycle) is forming a shock at $x = \bar{x}$. If the wave were to propagate further from the source, part of the negative pressure amplitude would also become multivalued. A similar response is expected for the case denoted by the red dashed

line, but a different point on the waveform becomes multivalued due to the waveform steepening in the opposite direction.

Shock formation distance is an important metric of understanding the nonlinearity associated with a medium. When absorption is accounted for, attenuation will damp the waveform before it becomes multivalued, but the qualitative dependence on $\bar{x}$ still applies to a lossy, nonlinear medium.

3.4.3 Dimensionless Evolution Equation

In order to model the propagation of an incident acoustic wave, an algorithm for solving the wave equation must be implemented. The computational methods utilized here requires a dimensionless wave equation. Typical means of non-dimensionalizing Eq. (3.50) employ dimensionless pressure $P \equiv p/p_0$, distance $\sigma \equiv x/\bar{x}$ and time $\theta \equiv \omega\tau$, where x is the distance from a source located at $x = 0$, p_0 is the acoustic pressure amplitude at the source, and ω is the angular frequency of the source. Equation (3.50) can now be converted to a dimensionless form,

$$\frac{\partial P}{\partial \sigma} = \alpha\bar{x}\frac{\partial^2 P}{\partial \theta^2} + \left(\frac{\beta p_0 \omega \bar{x} P}{\rho_0 c_0^3} + \frac{\gamma p_0^2 \omega \bar{x} P^2}{\rho_0^2 c_0^5}\right)\frac{\partial P}{\partial \theta}. \tag{3.61}$$

The fraction multiplying the second time derivative on the right-hand side of Eq. (3.61) is the reciprocal of the Gol'dberg number, Γ. The Gol'dberg number is a measure of the nonlinear effects relative to thermoviscous effects and is defined as [3]

$$\Gamma = \frac{1}{\alpha\bar{x}}. \tag{3.62}$$

The terms inside the parentheses in Eq. (3.61) account for the nonlinear distortion. For simplicity, the following coefficients N_1 and N_2 are defined as

$$N_1 = \beta M k\bar{x} = \frac{1}{\left[\cos\omega\tau + \gamma M/\beta \sin 2\omega\tau\right]_{\max}} \tag{3.63}$$

and

$$N_2 = \gamma M^2 k\bar{x} = \frac{1}{\left[\beta/\gamma M \cos\omega\tau + \sin 2\omega\tau\right]_{\max}}. \tag{3.64}$$

The magnitudes of N_1 and N_2 dictate the distorted shape of the propagating wave due to the nonlinearity, while the signs of N_1 and N_2, which directly relate to the signs of β and γ, respectively, correspond to the direction in which different portions of the wave distort. In the absence of cubic nonlinearity, $\gamma = 0$ and $N_2 = 0$, while $N_1 = \pm 1$ depending on whether β is positive of negative. Conversely, if $\beta = 0$ (no quadratic nonlinearity), then $N_1 = 0$ and $N_2 = \pm 1$ depending on the sign of γ.

The following dimensionless evolution equation is obtained by combining Eqs. (3.61)–(3.64):

$$\frac{\partial P}{\partial \sigma} = \left(N_1 P + N_2 P^2\right) \frac{\partial P}{\partial \theta} + \frac{1}{\Gamma} \frac{\partial^2 P}{\partial \theta^2}. \tag{3.65}$$

3.4.4 Simulations of Waveform Distortion

Equation (3.65) is solved computationally via a time domain code originally developed by Lee and Hamilton [91, 92] to solve the Burgers equation and the Khohklov-Zabolotskaya-Kuznetsov (KZK) equation. See also Cleveland *et al.* for further discussion of this approach [93]. The previously developed code

is augmented in the present work to account for cubic nonlinearities as described in Appendix C. Representative values of N_1 and N_2 are explored in Figs. 3.19–3.24 to illustrate the effects nonlinearity on a propagating acoustic wave. Some attenuation must be present in the code for it to correctly capture the distortion of the propagating acoustic waves beyond the shock formation distance and therefore a Gol'dberg number of $\Gamma = 100$ is chosen. For $\Gamma \gg 1$, the effects of dissipation near the shock formation distance are small. Thus, $\Gamma = 100$ corresponds to a small amount of absorption that allows the code to model the nonlinear response correctly. Each plot shows two cycles of a sinusoidal pressure wave at the source, $\sigma = 0$, and at three dimensionless distances from the source, $\sigma = 1$, $\sigma = 3$, and $\sigma = 5$. Note that $\sigma = 1$ depicts the distorted waveform at the shock formation distance. The vertical black dashed lines indicate the zero crossings of the initial sinusoidal pressure wave.

Figure 3.19 shows the distortion of the acoustic wave for $N_1 = 1$ and $N_2 = 0$ and represents the behavior typically studied with propagation through a nonlinear medium possessing only positive, quadratic nonlinearity. As the wave propagates away from the source, the component of the wave with a positive amplitude has a higher propagation speed and conversely the component of the wave with a negative amplitude has a lower propagation speed. The waveform has developed into a sawtooth profile for $\sigma \geq 3$. Attenuation in the medium reduces the amplitude of the wave. In Fig. 3.20, the distortion of the acoustic wave for $N_1 = -1$ and $N_2 = 0$ is plotted. The sinusoid steepens into a sawtooth wave in the opposite direction from that observed in Fig. 3.19. The

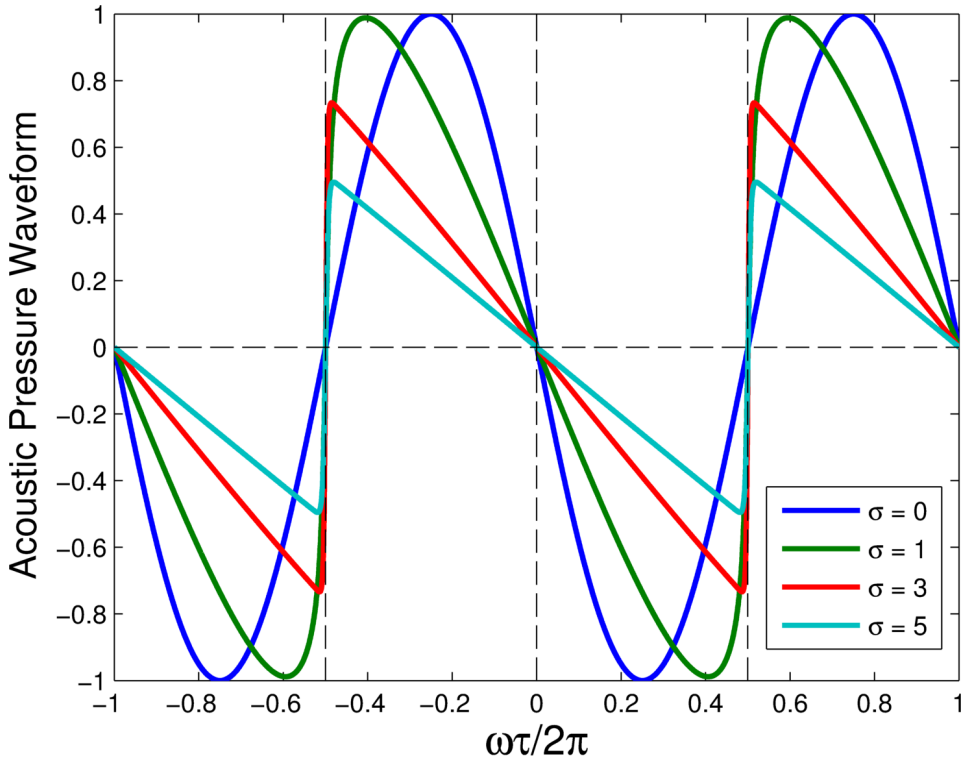

Figure 3.19: Positive, purely quadratic nonlinear distortion of an initially sinusoidal propagating wave with $N_1 = 1, N_2 = 0$ and $\Gamma = 100$.

behavior in Fig. 3.20 depicts a rarefaction shock, as opposed to the compression shocks in Fig. 3.19. Rarefaction shocks with quadratic nonlinearity are studied in detail in the literature in, for example, Refs. [81] and [94].

Figures 3.21 and 3.22 illustrate the distortion when cubic nonlinearity dominates. The distortion of compressions shocks is extensively analyzed in Ref. [95]. Unlike with quadratic nonlinearity, the distorted wave with cubic nonlinearity is no longer symmetric. In addition, one observes two shocks per cycle, as noted in Section 3.4.2. When $N_1 = 0$ and $N_2 = 1$, as in Fig. 3.21,

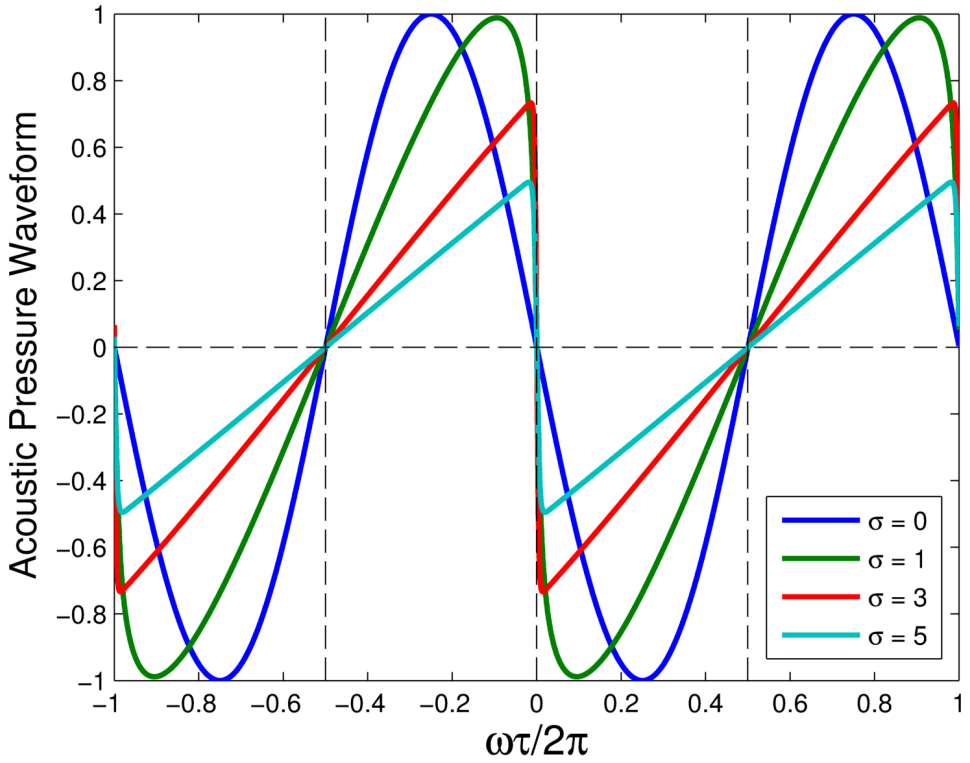

Figure 3.20: Negative, purely quadratic nonlinear distortion of an initially sinusoidal propagating wave for $N_1 = -1, N_2 = 0$ and $\Gamma = 100$.

the zero crossings of the waveform shift to the left as the wave steepens with increasing distance from the source. If $N_1 = 0$ and $N_2 = -1$, as shown in Fig. 3.22, the waveforms steepen in the opposite direction and the zero crossings of the rarefaction shocks now shift to the right. The amplitude of the acoustic wave is reduced as it propagates due to attenuation, as it was the case for purely quadratic nonlinearity.

In nonlinear acoustics, the propagation of an acoustic wave is typically limited to purely quadratic or purely cubic nonlinearity. For example,

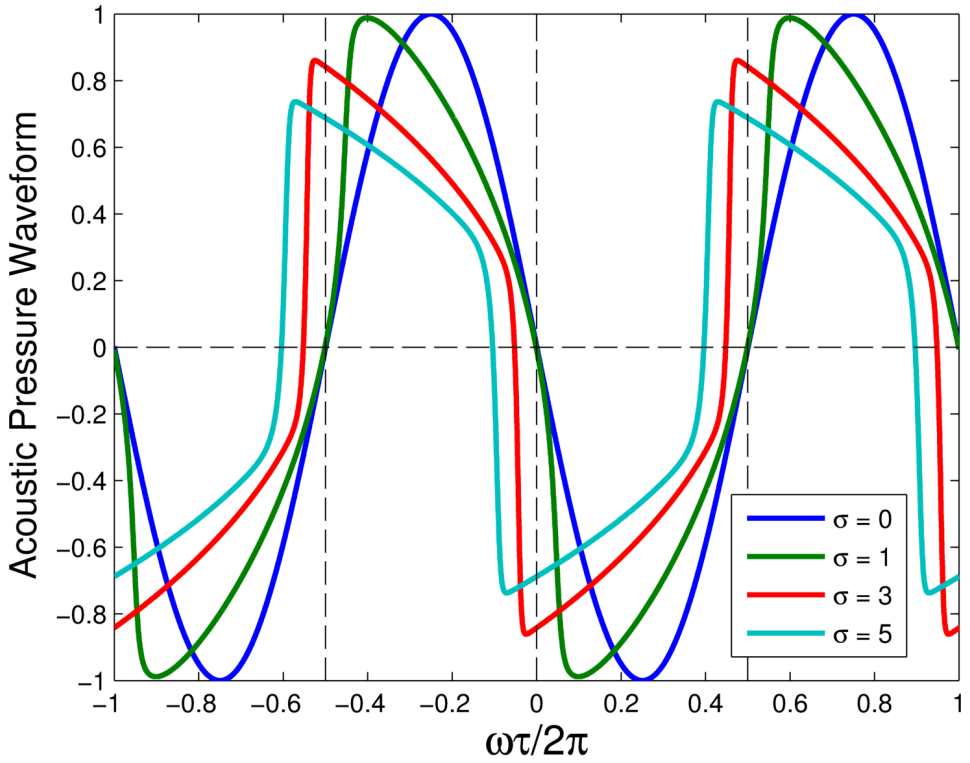

Figure 3.21: Positive, purely cubic nonlinear distortion of an initially sinusoidal propagating wave for $N_1 = 0, N_2 = 1$ and $\Gamma = 100$.

distortion of a propagating wave in a fluid usually requires only quadratic nonlinearity to describe the behavior [73]. Conversely, the distortion of shear waves in an elastic body correspond to a medium with only cubic nonlinearity [95]. Analysis of the distortion of an acoustic wave that has a combination of quadratic and cubic nonlinearity is therefore limited with respect to traditional materials. It was of interest, however, in the study of superfluid ^{3}He-B by Garrett [96]. Garrett shows waveforms for purely positive quadratic nonlinearity, purely negative cubic nonlinearity, and a mixture of the two. The SAMM inclusions offer the possibility to generalize the distortion to any com-

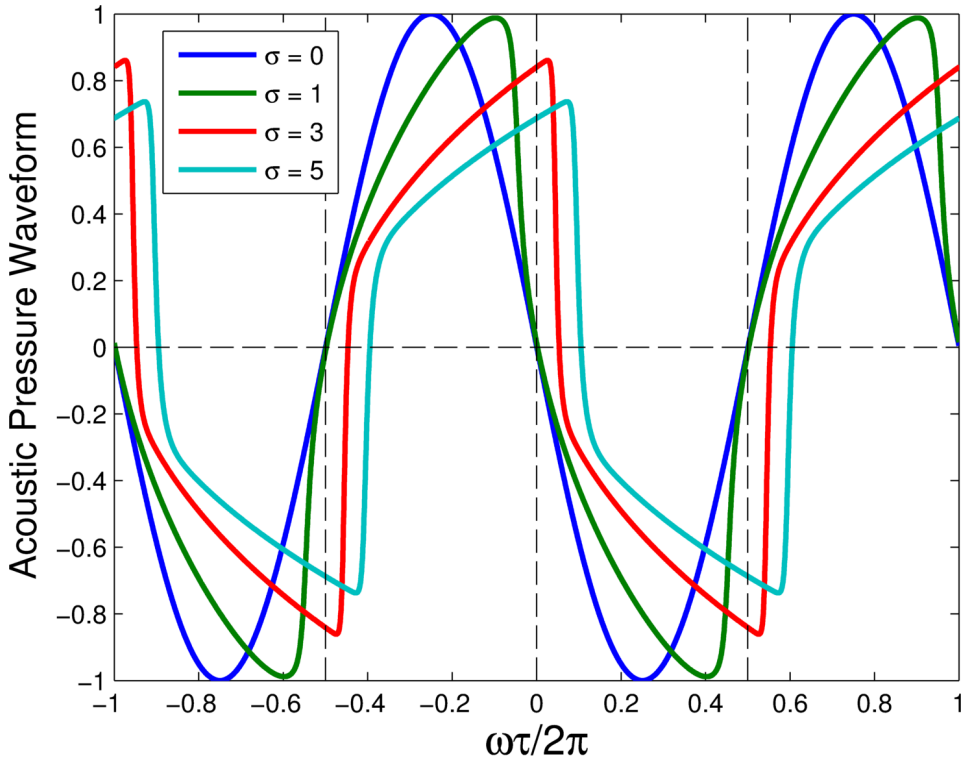

Figure 3.22: Negative, purely cubic nonlinear distortion of an initially sinusoidal propagating wave for $N_1 = 0, N_2 = -1$ and $\Gamma = 100$.

bination of positive or negative quadratic and cubic nonlinearities. Examples of two of possible combinations are shown in Figs. 3.23 and 3.24.

Different points on the same initial waveform form shocks depending on the relative magnitudes and signs of N_1 and N_2. For example, Fig. 3.23 shows the distorted waveform for $N_1 = 0.4$ and $N_2 = 0.6$. The waveform is still non-symmetric, but only the zero crossing with positive slope shifts, in this case to the left. The zero crossing of the initial waveform is at $\omega\tau/2\pi = \pm n/2$ for any integer n and is represented by the vertical black dashed lines. The

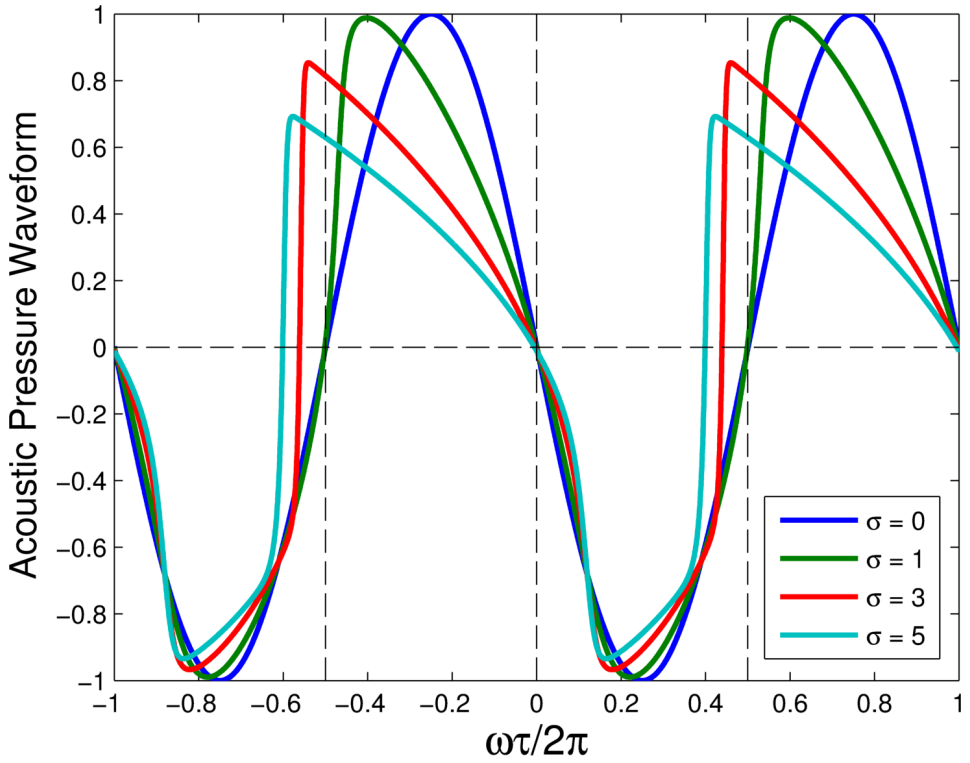

Figure 3.23: Positive, mixed order nonlinear distortion of an initially sinusoidal propagating wave for $N_1 = 0.4, N_2 = 0.6$ and $\Gamma = 100$.

positive slope of the waveform steepens into one shock for $\sigma > 1$, but as the wave propagates further from the source, the negative amplitude of the negative slope component also begins to steepen, near $\omega\tau/2\pi = 0.1, -0.9$, due to the cubic nonlinearity. The second shock will not develop until the wave propagates beyond the second shock formation distance. Figure 3.24 shows waveforms for $N_1 = 0.6$ and $N_2 = -0.4$. The zero crossings shift to the right because N_2 is negative, but only one nearly multivalued shock forms for the chosen σ. Another shock will form once the wave propagates to the second shock formation distance, which is greater than $x = 5\bar{x}$ for this case.

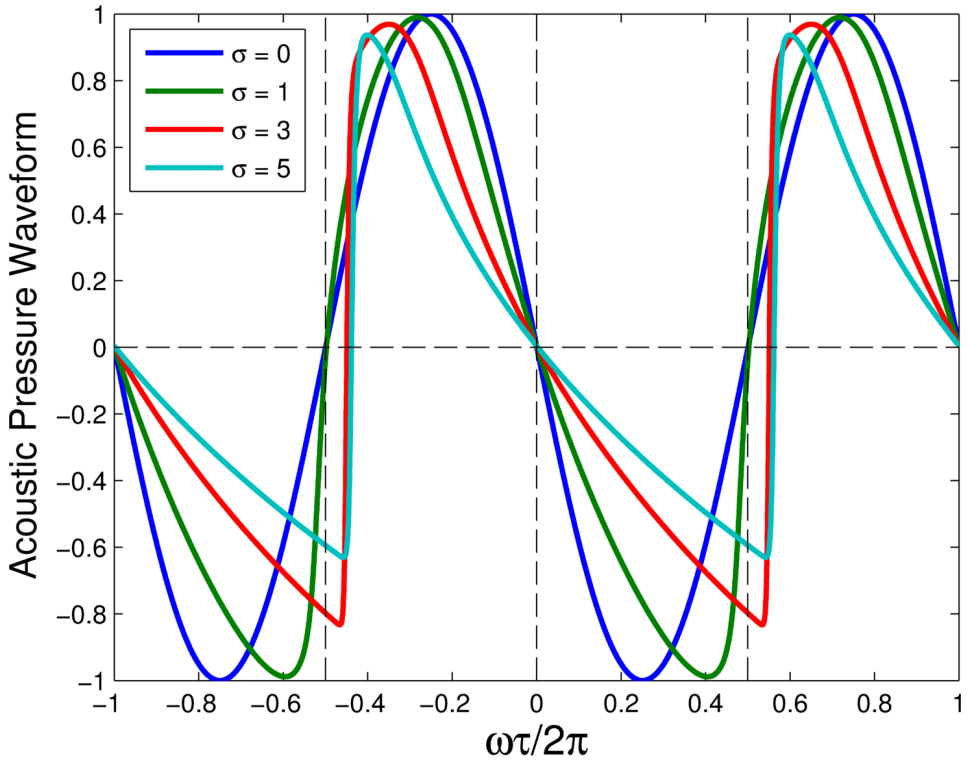

Figure 3.24: Positive and negative, mixed order nonlinear distortion of an initially sinusoidal propagating wave for $N_1 = 0.6, N_2 = -0.4$ and $\Gamma = 100$.

If either N_1 or N_2 is negative, for $N_2 \neq 0$, the zero crossings will shift to the right but if both are positive, they will shift to the left. Therefore, a wide variety of distorted waveforms are achievable due to combinations of signs and magnitudes of N_1 and N_2.

The purpose of presenting these examples of waveform distortion is to emphasize that the SAMM inclusions can be designed and tuned with an imposed macroscopic pre-strain to elicit a wide range of desired nonlinear responses. Embedding the SAMM inclusions within a matrix results in a

composite material that has enhanced nonlinearity that may be useful for a variety of wave manipulations applications. It is also worth noting that the attenuation associated with the effective medium was arbitrarily chosen as a small value. Although doing so is important to understand the nonlinear response, the actual damping associated with this effective medium is also unknown. Chapter 4 lays the foundation for developing a metric to quantify how energy is dissipated from a propagating acoustic wave in a heterogeneous material containing SAMM inclusions. The additional knowledge of knowing about material damping will provide a higher physical understanding of the heterogeneous material and allow the model presented in this chapter to be more readily used as a design tool for the fabrication of physically realizable SAMM inclusions for a desired application.

Chapter 4

Nonlinear Dynamics

The nonlinear dynamics associated with the snapping behavior of the SAMM inclusions when subjected to an external forcing acoustic pressure are presented here. The primary objective is to generate a model capable of capturing the response of a single SAMM inclusion, as well as a heterogeneous material that contains a dilute concentration of these inclusions. The approximate multiscale model, presented in detail in Section 3.2, decouples the equations of motion on each scale. Understanding the resulting nonlinear dynamic response of both the microscale and macroscale will allow for characterization of the damping associated with the entire effective medium.

4.1 Dissipation of Energy

The concept of energy dissipation is well understood within linear elasticity and is illustrated in Fig. 4.1. The red curve in Fig. 4.1(a) represents the amplitude, normalized by its maximum value, for an imposed sinusoidal strain field as a function of time. The resulting stress field is also a sinusoid, but is out of phase with the strain by some phase lag, δ. Figure 4.1(a) shows the amplitude of the time harmonic stress for two different phase lags. The blue

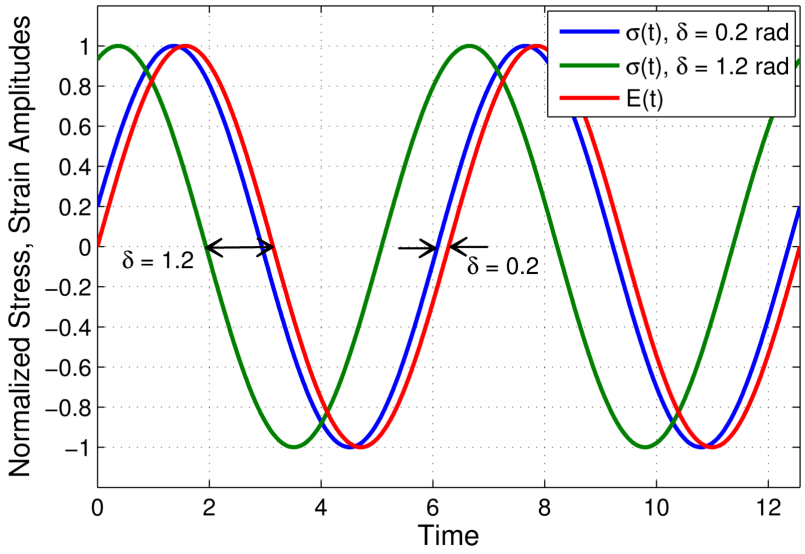

(a) Stress and strain amplitudes versus time

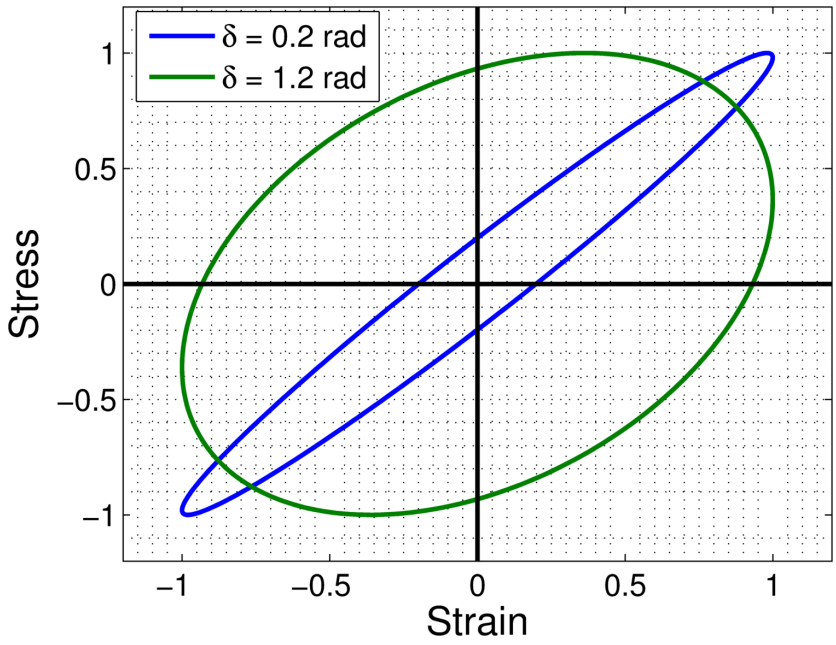

(b) Stress versus strain

Figure 4.1: Linear stress-strain relationships for a sinusoidal strain and stress for two different phase lags, $\delta = 0.2$ rad and $\delta = 1.2$ rad.

curve is the stress for $\delta = 0.2$ rad, indicating a small delay between the imposition of the strain, E, and the resulting stress, σ. The stress curve shown in green with $\delta = 1.2$ rad is shifted further from the strain curve than the stress with the smaller phase lag. The phase lag creates a hysteresis loop when the stress is plotted as a function of strain. The elliptic Lissajous figure is shown in the stress-strain curve in Fig. 4.1(b). The blue curve represents $\delta = 0.2$ rad, whereas the green curve is for $\delta = 1.2$ rad. The area outlined by the curves is related to the energy dissipated per cycle [97]. The green curve encloses a larger area, thus dissipating more energy.

Conventional materials found in nature cannot achieve both high stiffness and high loss and thus there exists a trade-off between the two material features. Acoustic metamaterials with negative elastic moduli, however, have the ability to enhance both the stiffness of and the energy dissipated within the composite material as highlighted in Section 1.3.1.2 [6]. Although stiffness and damping are more difficult to quantify with nonlinear elasticity, the area traced out in stress-strain space, or pressure-volumetric strain space, provides a metric of the energy dissipated by the nonlinear medium, while the stiffness is approximated using a tangent or secant approximation of the slope of the stress-strain response around a local configuration, as described in Section 2.1.2. The present chapter develops approximations of the two metrics for a heterogeneous medium consisting of SAMM inclusions embedded in a continuous host material.

4.2 Inclusion Dynamics of Rayleigh-Plesset Form

The dynamics of bubbles entrained in a fluid medium has been widely studied in the field of acoustics to understand important phenomena in research areas such as underwater sound propagation [79] and biomedical ultrasonics [88]. In most cases, the configuration of interest consists of a gas bubble, either free or encapsulated with a thin shell, within a fluid or fluid-like solid. When an external pressure is applied to the bubble, the internal pressure required to keep the bubble in quasi-static equilibrium must change, causing the radius to expand or contract [98]. The same occurs for the SAMM inclusions of interest. The internal pressure required to maintain equilibrium for a forced SAMM inclusion corresponds to the location on the constitutive pressure-volumetric strain curve. The dynamic response of a bubble is most simply modeled as a forced nonlinear oscillator through the Rayleigh-Plesset equation. A modified version of this nonlinear differential equation is adapted here to describe the change in volume of the SAMM inclusions.

The general dynamical system considered is shown in Fig. 4.2. The schematic represents any sphere embedded in a surrounding matrix undergoing some radial deformation due to a pressure, P_∞, imposed far away from the inclusion. The system of interest describes bubbles, as well as the dynamics of both a single SAMM inclusion and an effective medium that contains SAMM inclusions. For the sphere embedded in a matrix material, the instantaneous radius of the sphere, R, will change as a function of time due to the total pressure on the surface of the sphere, P_{total}.

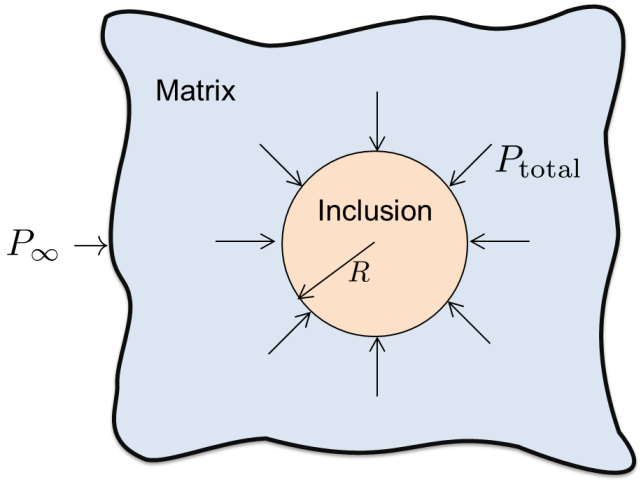

Figure 4.2: Schematic of the general dynamic system for a sphere embedded in a matrix material.

The nonlinear, second order differential equation describing the dynamics of a sphere embedded in a viscoelastic matrix material is of Rayleigh-Plesset form. The derivation, which appears in Appendix D using a Lagrangian approach for convenience, follows from Refs. [99], [100], and [101], using several assumptions. The sphere is assumed to be lossless. Thus, the damping is added to the overall system only through the viscoelastic matrix material, which is modeled as a lossy, linear, and nearly incompressible elastic medium. Recall from Section 3.2 that the size of the inclusion is much smaller than the wavelength of a propagating acoustic wave through the matrix. Because of this assumption, radiation losses from the inclusion's oscillations can be neglected and the matrix can reasonably be modeled as a nearly incompressible elastic solid. Additionally, the mass of the bubble itself is typically ignored because the surrounding material, either a fluid or nearly incompressible solid,

is typically orders of magnitude more dense than the gas within the bubble. The kinetic energy of the gas is therefore negligibly small in comparison to that of the matrix [98]. As a first approximation, effects due the density of the SAMM inclusions and effective medium will also be neglected. Using these assumptions, one obtains the following equation of Rayleigh-Plesset form,

$$R\ddot{R} + \frac{3}{2}\dot{R}^2 = \frac{P_{\text{total}}}{\rho_{\text{M}}} - \frac{4\eta_{\text{M}}}{\rho_{\text{M}}}\frac{\dot{R}}{R}, \tag{4.1}$$

where ρ_{M} is the density of the matrix, η_{M} is the shear viscosity of the matrix, and the dots indicate derivatives with respect to time. The total pressure, P_{total}, is evaluated at the surface of the inclusion. The specific form of P_{total} for the single SAMM inclusion and effective medium will be presented in the following sections.

4.2.1 SAMM Inclusion

The simplest way to model the dynamics of the system is to decouple the length scales such that the microscale and macroscale are modeled independently. Thus in the present research, the dynamic response of the effective medium is not influenced by the behavior of the SAMM inclusions, and vice versa. The first case considers the oscillations of one SAMM inclusion embedded in the nearly incompressible matrix, which is schematized in Fig. 4.3. The total pressure at the interface between the inclusion and matrix is comprised of three components: (*i*) the pressure infinitely far away from the inclusion, P_∞, may include a constant static pressure, a time-harmonic, acoustic pressure, or both; (*ii*) the pressure due to the shear stress of the elastic matrix, P_{M}^{I}, which

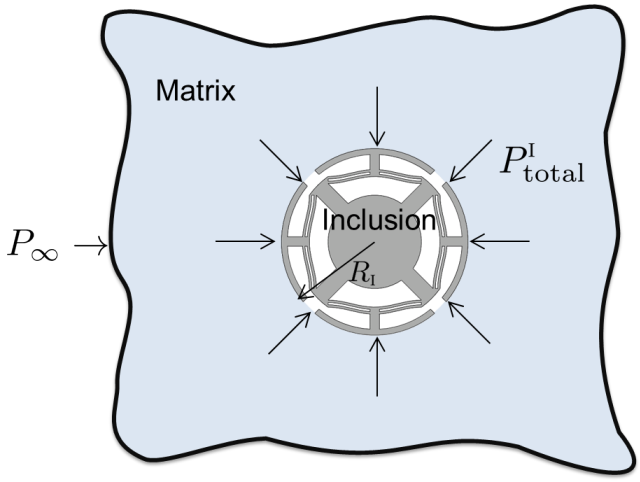

Figure 4.3: Schematic of the dynamic system for one SAMM inclusion in matrix material.

is derived with further details in Appendix D, assumes the following form

$$P^{\mathrm{I}}_{\mathrm{M}} = -\frac{4}{3}\mu_{\mathrm{M}}\varepsilon_{v\mathrm{I}}, \tag{4.2}$$

where μ_{M} is the shear modulus and the superscript I on $P^{\mathrm{I}}_{\mathrm{M}}$ indicates that the effective pressure due to the deformation of the matrix is evaluated at the surface of the inclusion; and (*iii*) the internal pressure from the SAMM inclusion itself, which is found using the assumed constitutive pressure-volumetric strain relationship introduced in Section 2.2 and is repeated here for convenience,

$$P_{\mathrm{I}} = P_{\mathrm{I}_0} - K_{\mathrm{I}}\varepsilon_{v\mathrm{I}} + \frac{1}{2}K'_{\mathrm{I}}\varepsilon^2_{v\mathrm{I}} - \frac{1}{6}K''_{\mathrm{I}}\varepsilon^3_{v\mathrm{I}}. \tag{4.3}$$

The resulting approximate expression describing the forced dynamics of the inclusion is of the same as Eq. (4.1):

$$R_{\mathrm{I}}\ddot{R}_{\mathrm{I}} + \frac{3}{2}\dot{R}^2_{\mathrm{I}} = \frac{P_{\mathrm{I}} + P^{\mathrm{I}}_{\mathrm{M}} - P_\infty}{\rho_{\mathrm{M}}} - \frac{4\eta_{\mathrm{M}}}{\rho_{\mathrm{M}}}\frac{\dot{R}_{\mathrm{I}}}{R_{\mathrm{I}}}. \tag{4.4}$$

Comparing a linearized form of Eq. (4.4) with the general linear oscillator due to a forcing function, $F(t)$, as given by [55]

$$\ddot{z} + \frac{\omega_0}{Q}\dot{z} + \omega_0^2 z = F(t), \tag{4.5}$$

allows characterization of the natural frequency of the system, ω_0, and the quality factor of the system, Q. Linearizing Eq. (4.4) by letting $R_{\mathrm{I}} = R_{\mathrm{I}_0} + x$, where x is a small perturbation from the equilibrium radius, R_{I_0}, provides the following:

$$\ddot{x} + \frac{4\eta_{\mathrm{M}}}{\rho_{\mathrm{M}} R_{\mathrm{I}_0}^2}\dot{x} + \frac{3K_{\mathrm{I}} + 4\mu_{\mathrm{M}}}{\rho_{\mathrm{M}} R_{\mathrm{I}_0}^2}x = -\frac{P_\infty}{\rho_{\mathrm{M}} R_{\mathrm{I}_0}^2}. \tag{4.6}$$

The natural frequency of the system, ω_{I_0} has two components: ω_{I} and ω_{M}. The first corresponds to the natural frequency of the SAMM inclusion, ω_{I}, when embedded in a nearly incompressible matrix in the limit of zero shear modulus, and the second is the oscillation frequency of a spherical cavity in the matrix, ω_{M}, such that $\omega_{\mathrm{I}_0}^2 = \omega_{\mathrm{I}}^2 + \omega_{\mathrm{M}}^2$. The frequencies are obtained by comparing Eqs. (4.5) and (4.6), to yield

$$\omega_{\mathrm{I}}^2 = \frac{3K_{\mathrm{I}}}{\rho_{\mathrm{M}} R_{\mathrm{I}_0}^2} \tag{4.7}$$

and

$$\omega_{\mathrm{M}}^2 = \frac{4\mu_{\mathrm{M}}}{\rho_{\mathrm{M}} R_{\mathrm{I}_0}^2}. \tag{4.8}$$

Likewise, an expression for the quality factor, which is a damping characterization metric that is inversely proportional to the rate of energy loss relative

to energy stored in a resonator, is

$$Q_{\mathrm{I}} = \frac{\rho_{\mathrm{M}} R_{\mathrm{I}_0}^2 \omega_{\mathrm{I}_0}}{4\eta_{\mathrm{M}}}. \tag{4.9}$$

It is helpful to express Eq. (4.4) in a dimensionless form for computational efficiency. Defining a dimensionless radius, $\mathcal{R}_{\mathrm{I}} = R_{\mathrm{I}}/R_{\mathrm{I}_0}$, a dimensionless velocity, $\mathcal{S}_{\mathrm{I}} = \dot{\mathcal{R}}_{\mathrm{I}}$, and a dimensionless time $\tau = \omega_{\mathrm{I}} t/2\pi$ allows Eq. (4.4) to be expressed as

$$\frac{\omega_{\mathrm{I}}^2 R_{\mathrm{I}_0}^2}{4\pi^2}\mathcal{R}_{\mathrm{I}}\dot{\mathcal{S}}_{\mathrm{I}} + \frac{3}{2}\frac{\omega_{\mathrm{I}}^2 R_{\mathrm{I}_0}^2}{4\pi^2}\mathcal{S}_{\mathrm{I}}^2 = \frac{P_{\mathrm{I}} + P_{\mathrm{M}}^{\mathrm{I}} - P_\infty}{\rho_{\mathrm{M}}} - \frac{4\eta_{\mathrm{M}}}{\rho_{\mathrm{M}}}\frac{\omega_{\mathrm{I}}}{2\pi}\frac{\dot{\mathcal{R}}_{\mathrm{I}}}{\mathcal{R}_{\mathrm{I}}}. \tag{4.10}$$

The dimensionless expression of Rayleigh-Plesset form, which is obtained through use of the expressions in Eqs. (4.7) and (4.9) in Eq. (4.10) and by solving for $\dot{\mathcal{S}}_{\mathrm{I}}$, is solved as a pair of coupled, first order ordinary differential equations, given by

$$\dot{\mathcal{R}}_{\mathrm{I}} = \mathcal{S}_{\mathrm{I}} \tag{4.11}$$

$$\dot{\mathcal{S}}_{\mathrm{I}} = -\frac{3}{2}\frac{{\mathcal{S}_{\mathrm{I}}}^2}{\mathcal{R}_{\mathrm{I}}} + \frac{4\pi^2}{3K_{\mathrm{I}}\mathcal{R}_{\mathrm{I}}}\left(P_{\mathrm{I}} + P_{\mathrm{M}}^{\mathrm{I}} - P_\infty\right) - \frac{2\pi}{Q_{\mathrm{I}}}\sqrt{1 + \frac{4\mu_{\mathrm{M}}}{3K_{\mathrm{I}}}}\frac{\mathcal{S}_{\mathrm{I}}}{{\mathcal{R}_{\mathrm{I}}}^2}. \tag{4.12}$$

Note that it is possible to derive a non-dimensional form of Eq. (4.4) that differs from Eq. (4.12), particularly by redefining τ. In Eq. (4.12), time is nondimensionalized with respect to the natural frequency of the SAMM inclusion. This frequency was chosen in order to clearly illustrate that the dynamical behavior of interest occurs even when the frequency of the acoustic driving pressure is well below the resonance frequency of the SAMM inclusion. For example, assume the driving pressure is a sinusoidal function, such that

$P_\infty = p_0 \sin \omega t$, where ω is the frequency of the driving pressure. In terms of τ and a dimensionless drive frequency defined as $\bar{\omega} = \omega/\omega_{\text{I}}$, the pressure at infinity is then

$$P_\infty = p_0 \sin 2\pi\bar{\omega}\tau. \tag{4.13}$$

Expressing $\bar{\omega}$ as a function of ω_{I}, instead of ω_{I_0}, defines the acoustic driving frequency as some percentage of the resonance frequency of the SAMM inclusion. For example, if $\bar{\omega} = 0.1$, then the resulting dynamical response corresponds to frequencies well below the resonance of the SAMM inclusion. Recall from Chapter 1 that the frequency range in which some acoustic metamaterials operate efficiently is often limited to near resonance. Using a time scale nondimensionalized by ω_{I} emphasizes that the snapping dynamical behavior is not limited to a range near the SAMM resonance frequency, indicating more versatility than other acoustic metamaterials. The subresonant behavior will be illustrated in Section 4.3.

4.2.2 Nonlinear Effective Medium Response

For an effective medium described as a decoupled, single scale dynamical system, the nonlinear response can be modeled in a manner similar to that presented in the previous section for the SAMM inclusion. The schematic in Fig. 4.4 depicts a spherical inclusion undergoing the deformation, where the inclusion now represents an effective medium that contains a dilute concentration of SAMM inclusions embedded in the matrix material. In this case, the dynamical response is well represented using Eq. (4.1) with the effective

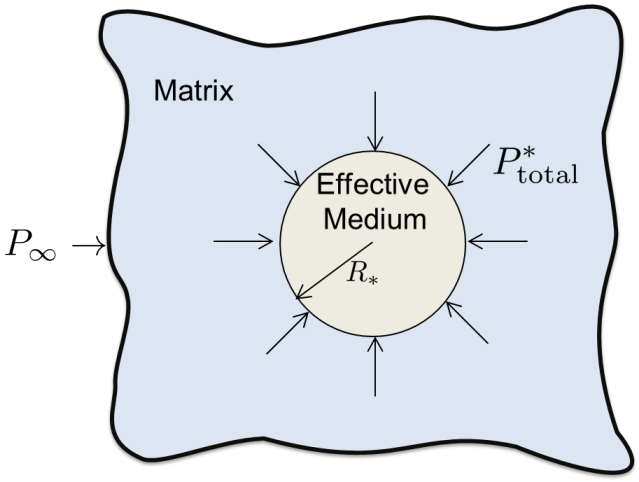

Figure 4.4: Schematic of the dynamics for a sphere of the effective medium embedded in a matrix material.

material parameters substituted in for the inclusion:

$$R_* \ddot{R}_* + \frac{3}{2}\dot{R}_*^2 = \frac{P_* + P_{\text{M}}^* - P_\infty}{\rho_{\text{M}}} - \frac{4\eta_{\text{M}}}{\rho_{\text{M}}}\frac{\dot{R}_*}{R_*}. \tag{4.14}$$

The subscript $*$ now refers to the instantaneous radius of the effective medium, while the superscript $*$ on P_{M}^* indicates the effective pressure contributions of the matrix on the surface of the effective medium. Thus, the effective pressure of the matrix material is given by

$$P_{\text{M}}^* = -\frac{4}{3}\mu_{\text{M}}\varepsilon_{v_*}. \tag{4.15}$$

The internal pressure of the effective medium is a third order expansion with respect to macroscopic volumetric strain, such that

$$P_* = P_{*_0} - K_*\varepsilon_{v_*} + \frac{1}{2}K_*'\varepsilon_{v_*}^2 - \frac{1}{6}K_*''\varepsilon_{v_*}^3. \tag{4.16}$$

The nonlinear stiffness parameters, K_*, K_*', and K_*'', are obtained from the Hashin-Shtrikman method detailed in Section 3.2.2.1. Therefore, the dynamics on the macroscale necessarily correspond to the quasi-static limit that is only accurate for frequencies well below the resonance of a single SAMM inclusion.

Just as with the SAMM inclusion, a resonance frequency and quality factor describing the effective medium are obtained by comparing the small amplitude limit of Eq. (4.14) with that of a linear oscillator described in Eq. (4.5). Linearizing Eq. (4.14) with $R_* = R_{*_0} + y$, where y is a small perturbation from the equilibrium radius R_{*_0} of the effective medium provides

$$\ddot{y} + \frac{4\eta_{\mathrm{M}}}{\rho_{\mathrm{M}} R_{*_0}^2}\dot{y} + \frac{3K_* + 4\mu_{\mathrm{M}}}{\rho_{\mathrm{M}} R_{*_0}^2} y = -\frac{P_\infty}{\rho_{\mathrm{M}} R_{*_0}^2}. \tag{4.17}$$

The natural frequency of the effective medium surrounded by an elastic medium with zero shear modulus is

$$\omega_*^2 = \frac{3K_*}{\rho_{\mathrm{M}} R_{*_0}^2}. \tag{4.18}$$

The other component of the natural frequency of the system can be expressed in terms Eq. (4.8). R_{*_0} can be expressed as a function of R_{I_0} due to the expression for volume fraction given in Eq. (3.13), such that $R_{*_0}^2 = (N/\phi)^{2/3} R_{\mathrm{I}_0}^2$. The natural frequency of the effective medium system is then

$$\omega_{*_0}^2 = \omega_*^2 + \omega_{\mathrm{M}}^2 \left(\frac{\phi}{N}\right)^{2/3}, \tag{4.19}$$

where ω_{M} is defined in Eq. (4.8). Matching terms in Eq. (4.5) and (4.17) yields a quality factor, Q_*, given by

$$Q_* = \frac{\rho_{\mathrm{M}} R_{*_0}^2 \omega_{*_0}}{4\eta_{\mathrm{M}}}. \tag{4.20}$$

Although the two scales are decoupled, the behavior of a SAMM inclusion still affects the response on the macroscale if the same non-dimensional time is used. The same expression for time, $\tau = \omega_{\mathrm{I}} t/2\pi$, is used in order to understand the behavior on the macroscale in relation to the behavior on the microscale, especially when considering the same external forcing pressure. Through use of the dimensionless radius $\mathcal{R}_* = R_*/R_{*_0} = (R_*/R_{\mathrm{I}_0})\,(\phi/N)^{1/3}$, Eq. (4.14) becomes:

$$\frac{\omega_{\mathrm{I}}^2 N^{2/3} R_{\mathrm{I}_0}^2}{4\pi^2\phi^{2/3}}\mathcal{R}_*\dot{\mathcal{S}}_* + \frac{3}{2}\frac{\omega_{\mathrm{I}}^2 N^{2/3} R_{\mathrm{I}_0}^2}{4\pi^2\phi^{2/3}}\mathcal{S}_*^2 = \frac{P_* + P_{\mathrm{M}}^* - P_\infty}{\rho_{\mathrm{M}}} - \frac{4\eta_{\mathrm{M}}}{\rho_{\mathrm{M}}}\frac{\omega_{\mathrm{I}}}{2\pi}\frac{\dot{\mathcal{R}}_*}{\mathcal{R}_*}, \tag{4.21}$$

where time derivatives are now with respect to τ. Rearranging Eq. (4.21) for $\dot{\mathcal{S}}_*$ yields

$$\begin{aligned}\dot{\mathcal{S}}_* = &-\frac{3}{2}\frac{\mathcal{S}_*^2}{\mathcal{R}_*} + \frac{4\pi^2\phi^{2/3}}{\omega_{\mathrm{I}}^2 N^{2/3} R_{\mathrm{I}_0}^2 \rho_{\mathrm{M}} \mathcal{R}_*}\left(P_* + P_{\mathrm{M}}^* - P_\infty\right) \\ &-\frac{4\eta_{\mathrm{M}}}{\rho_{\mathrm{M}}}\frac{4\pi^2\phi^{2/3}}{\omega_{\mathrm{I}}^2 N^{2/3} R_{\mathrm{I}_0}^2}\frac{\omega_{\mathrm{I}}}{2\pi}\frac{\dot{\mathcal{R}}_*}{\mathcal{R}_*^2}.\end{aligned} \tag{4.22}$$

One can then make use of the expressions in Eqs. (4.7) and (4.9) in Eq. (4.22) to find the following dimensionless expression of Rayleigh-Plesset form for the dynamical response of the effective inclusion,

$$\dot{\mathcal{R}}_* = \mathcal{S}_*, \tag{4.23}$$

$$\begin{aligned}\dot{\mathcal{S}}_* = &-\frac{3}{2}\frac{\mathcal{S}_*^2}{\mathcal{R}_*} + \frac{4\pi^2}{3K_{\mathrm{I}}\mathcal{R}_*}\left(\frac{\phi}{N}\right)^{2/3}\left(P_* + P_{\mathrm{M}}^* - P_\infty\right) \\ &-\frac{2\pi}{Q_{\mathrm{I}}}\sqrt{1 + \frac{4\mu_{\mathrm{M}}}{3K_{\mathrm{I}}}}\left(\frac{\phi}{N}\right)^{2/3}\frac{\dot{\mathcal{R}}_*}{\mathcal{R}_*^2}.\end{aligned} \tag{4.24}$$

Once again, it is possible to obtain different dimensionless forms for Eq. (4.24). The nondimensionlization chosen here is consistent with that of the single

SAMM inclusion case, which allows a more direct comparison between the two length scales for the same initial conditions.

4.3 Nonlinear Dynamics Results

The nonlinear dynamic response of both a single SAMM inclusion in a continuous matrix and an effective medium inclusion in a matrix are obtained by integrating the coupled equations given by Eqs. (4.11) and (4.12) and Eqs. (4.23) and (4.24) using a fourth order Runge-Kutta ordinary differential equation solver. For simplicity, static values of the elastic parameters K_{I}, K_{I}', and K_{I}'' obtained from a global fit of the constitutive curve shown in Fig. 2.6 are chosen. The fit yields $K_{\text{I}} = 16.93$ MPa, $K_{\text{I}}' = -189.03$ MPa, and $K_{\text{I}}'' = 809.76$ MPa. Similarly, the elastic parameters of the effective inclusion are chosen by fitting the constitutive curve shown in Fig. 3.11 for $\nu = 0.4991$. A fit of that response yields $K_* = 116.59$ MPa, $K_*' = -22.44$ GPa, and $K_*'' = 4.18$ TPa. Recall from Section 2.1.2 that the use of global coefficients may be too simple for the complicated nonlinear behavior of the SAMM inclusions. However, the use of static values allows for a simpler, decoupled multiscale system, which will serve as a first approximation of the nonlinear system in order to provide insight into the complicated snapping behavior. Note that even though the effective medium dynamics are solved for independently of the SAMM inclusion, certain input parameters on the macroscale depend on constants from the microscale. For example, K_{I} and Q_{I} appear in Eq. (4.24) due to the nondimensional time chosen, but the parameters are

constants.

The present work considers a heterogeneous material containing $N = 20$ SAMM inclusions comprising $\phi = 1\%$ of the total volume. With the assumed parameters of the matrix material and SAMM inclusion, it is possible to constrain each inclusion to its negative stiffness regime while maintaining stability of the overall effective medium.

For all cases considered, the initial radii of the SAMM inclusion and effective medium are their equilibrium radii, R_{I_0} and R_{*_0}, indicating zero volumetric strain, and the initial velocity of both is 0. In order to emphasize that the simulated dynamics represent subresonant SAMM inclusion behavior, the acoustic pressure at infinity is assumed to be a sinusoid with dimensionless drive frequency $\bar{\omega} = 0.1$. Other parameters, such as quality factor, Q_{I}, and amplitude of the acoustic driving pressure, p_0, will vary with the cases presented in Sections 4.3.1–4.3.3.

The solution for an oscillator has two components; one is transient and the other is steady state. The transient component is characterized by a complicated, non-periodic response due to the contribution of other frequencies. The transient occurs immediately after an external force is applied, but decays to zero for some finite time after the initial disturbance. On the other hand, the steady state response tends to correspond to a system oscillating at the driving frequency of the forcing function [98]. However, the two regimes are not as simply defined when the nonlinear dynamics of a system are considered. For example, transient chaos may occur where the random-like response

remains present over large time periods [58]. It is possible that steady-state oscillations, where the motion follows the same path for each period, may not be obtained over the time scales considered, which is the case in Section 4.3.2. Further, when a bistable oscillator is driven at a forcing frequency much less than the natural frequency of the oscillator, there are two time scales that describe the steady state oscillations [102]. A slow time scale, corresponding to the frequency of the driving force as previously described, is indicative of the overall shape. A fast time scale is responsible for any other oscillations present in the dynamic response. For example, there may be additional disturbances that ring down near the maxima or minima of the slow scale oscillations. Such a response with fast and slow time scales is shown in Section 4.3.1.

4.3.1 Single SAMM Inclusion

The first three figures in this section compare the response for a single SAMM inclusion embedded in a continuous matrix material that is driven at different acoustic pressure amplitudes for $Q_{\text{I}} = 2$. The transient component has been removed to clearly see the steady state response of interest. Figure 4.5 shows the instantaneous radius normalized by the equilibrium radius for a single SAMM inclusion versus dimensionless time $\omega_{\text{I}} t$. The blue curve is the lowest drive pressure, $p_0 = 0.5$ MPa, and represents the response of an SAMM inclusion operating within a linear section of the constitutive relation. To better see the response, Fig. 4.5(b) shows just the behavior for $p_0 = 0.5$ MPa with a more zoomed in y-axis. This response is as expected for

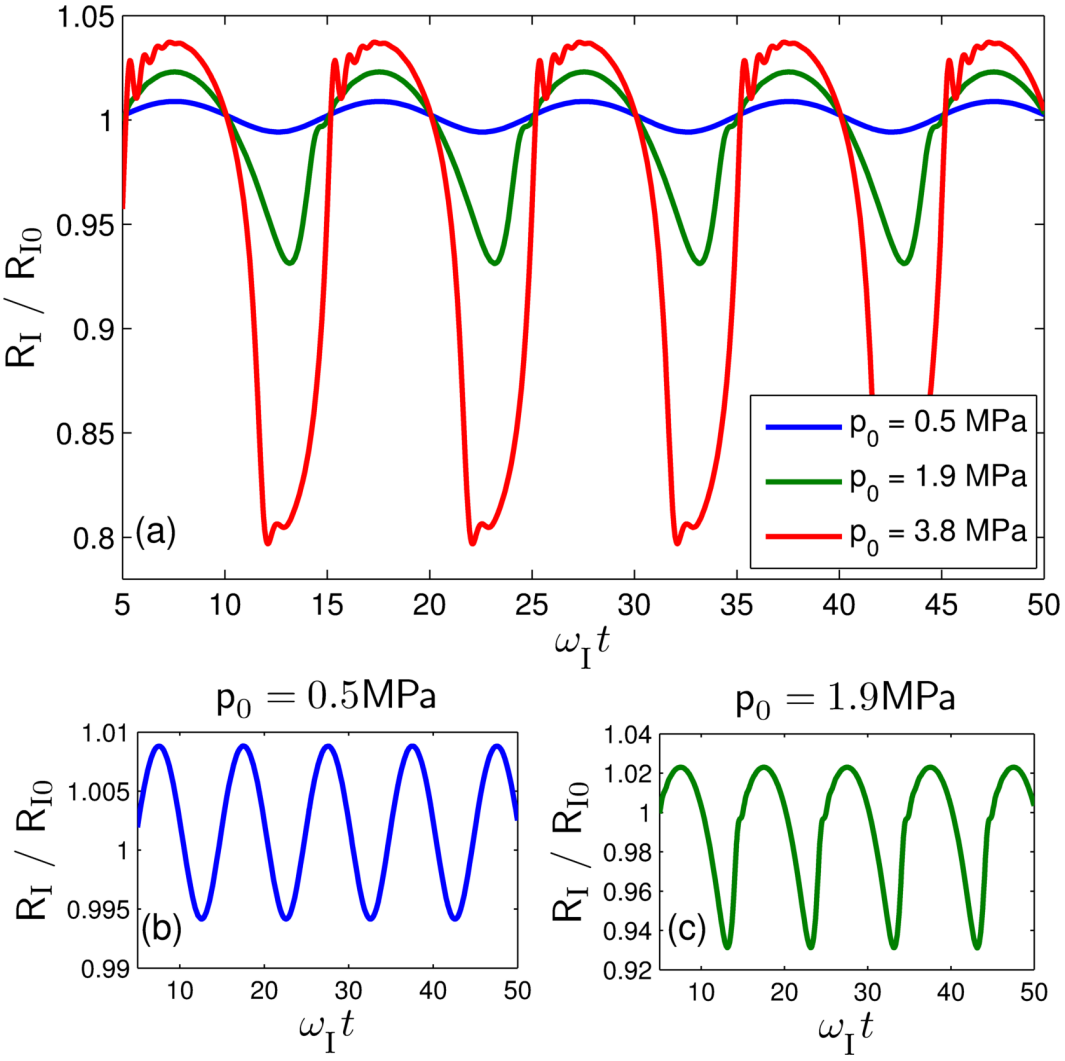

Figure 4.5: Normalized radius of SAMM inclusion versus dimensionless time for $p_0 = 0.5$ MPa, $p_0 = 1.9$ MPa, and $p_0 = 3.8$ MPa and $Q_I = 2$.

a linear oscillator; the radius fluctuates for small magnitudes about $R_{\text{I}} = R_{\text{I}0}$ in a smooth and sinusoidal manner. As the pressure amplitude increases, the radius expands and contracts to larger magnitudes of $\mathcal{R}_{\text{I}}$, pushing the SAMM inclusion into nonlinear regimes of its constitutive response. The green curve, which corresponds to $p_0 = 1.9$ MPa, accounts for quadratic nonlinearities and is shown more clearly in Fig. 4.5(c). The red curve is the highest drive pressure considered, $p_0 = 3.8$ MPa. For the higher pressure amplitude, the SAMM inclusion now operates within the fully cubic non-monotonic constitutive curve.

While the blue curve is smooth, the green and red curves have additional oscillations. These transient oscillations on the fast time scale occur when the SAMM inclusion snaps from one configuration to another. For the $p_0 = 1.9$ MPa drive amplitude (the green curve), the overall oscillations go from about 0.93 to 1.03, with additional oscillations occurring near $R_{\text{I}} = R_{\text{I}0}$. For $p_0 = 3.9$ MPa (the red curve), the overall oscillations go back and forth from 0.8 to 1.03, and the fast scale transient oscillations are present near the minimum and maximum of the overall response. By decreasing the quality factor, the amount of damping in the matrix increases and the curves will smooth out to eliminate the fast scale transient response.

Aside from the high frequency oscillations associated with snapping, one also notes that while the low drive response is nearly symmetric about $R_{\text{I}} = R_{\text{I}0}$, the behavior at the higher drive pressure is very asymmetric. As the drive pressure increases, the maximum change in radius from equilibrium as the SAMM inclusion expands differs from the change in radius for com-

pression. The asymmetry of the radial oscillations is expected for nonlinear oscillators and is also observed in the nonlinear behavior associated with a gas bubble. In the low amplitude limit for driving pressure, a gas bubble should respond like a linear oscillator, but for higher pressure magnitudes, the response becomes non-symmetric about its equilibrium [98]. Such features are further exemplified in Figs. 4.6 and 4.7, which show the normalized radial velocity versus normalized radius and the total pressure at the inclusion-matrix interface versus volumetric strain, respectively. Additionally, it is worth noting that all three pressure amplitudes induce a seemingly periodic response. Once the initial transient component has decayed to zero, each curve shows the SAMM inclusion periodically forced to the same radii during each period defined by the slow time scale.

The phase space shown in Fig. 4.6(a) plots the normalized velocity for a single SAMM inclusion versus the dimensionless radius for the same three pressure magnitudes shown in Fig. 4.5. Because the dimensionless radius and velocity are much larger for $p_0 = 3.8$ MPa, a zoomed in version of $p_0 = 0.5$ MPa is shown in Fig. 4.6(b), while a zoomed in version of $p_0 = 1.9$ MPa is shown in Fig. 4.6(c). Phase space is a valuable tool for studying nonlinear dynamics. It provides an assessment of a variety of characteristics of motion, such as whether the solution corresponds to movement that is recurrent, restricted to some region, attracted to some stability point, and so forth [63]. Although phase space is represented in terms of two variables, position and velocity, it also has a time dependence. Thus the trajectories traced out are necessar-

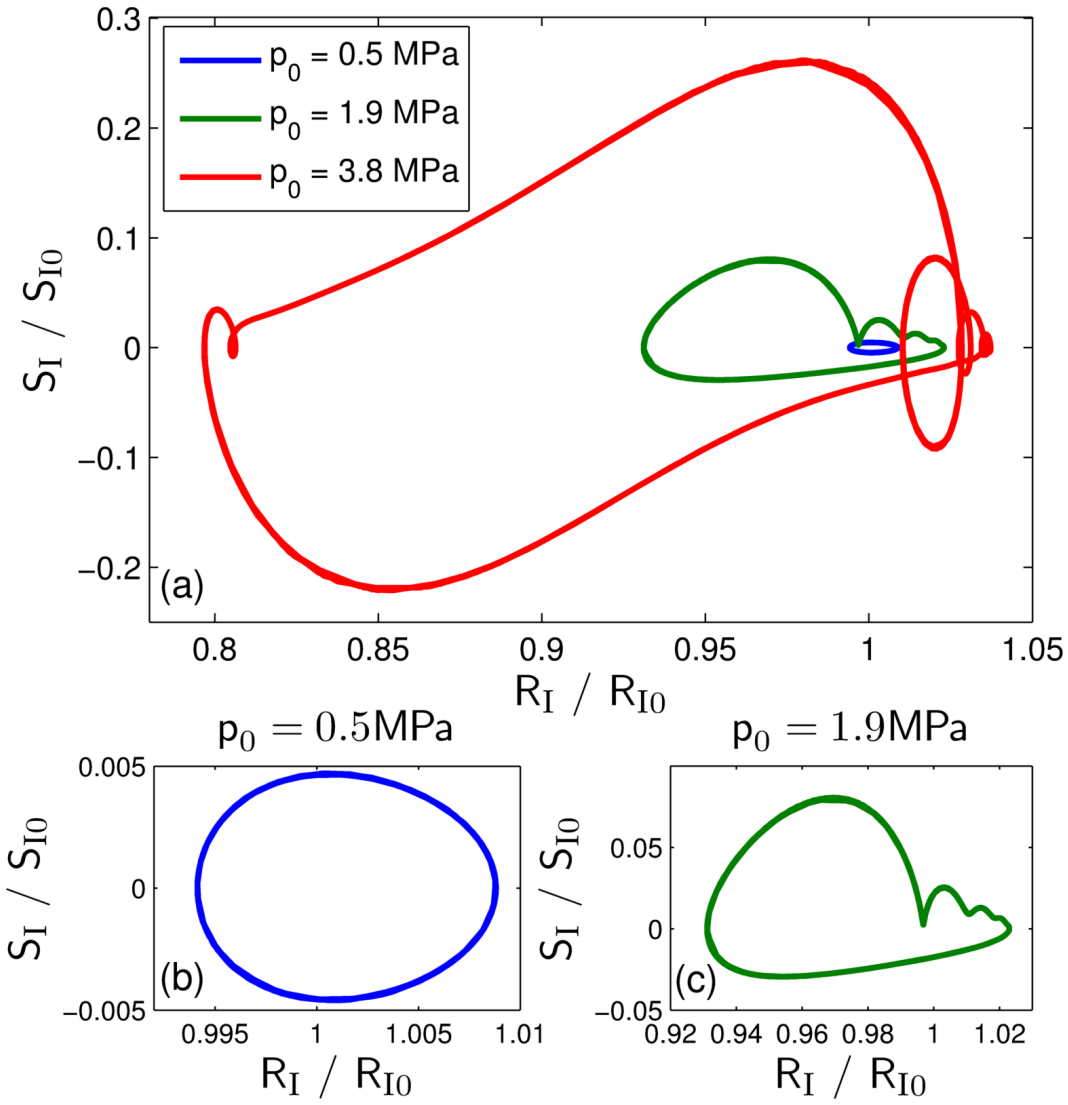

Figure 4.6: Normalized velocity of SAMM inclusion versus normalized radius for $p_0 = 0.5$ MPa, $p_0 = 1.9$ MPa, and $p_0 = 3.8$ MPa and $Q_{\text{I}} = 2$.

ily non-intersecting, which would be apparent if Fig. 4.6 is plotted in three variables as a projection through time [58]. Consider first the blue curve in Fig. 4.6, which is only the steady state response. It traces out approximately the same path for each period as indicated by the single ellipsoidal shape. Similarly, the green curve also periodically traces out the same path, though the phase space for $p_0 = 1.8$ MPa differs from that for $p_0 = 0.5$ MPa. The same is also true for $p_0 = 3.8$ MPa; the red curve also repeats, but the phase space is different than the blue and green curves. This clearly indicates the periodicity of the forced oscillations for a single SAMM inclusion for each acoustic pressure amplitude. The increase in area traced out by the phase space trajectories also increases for forcing amplitude. The period of the oscillations, as defined by the slow time scale, is the same for all three cases, while the maximum magnitude of the radius increases with forcing pressure. Therefore, the SAMM inclusion oscillates more quickly to attain the larger volume changes over the same time period. Although the time period is the same, the frequency content of these oscillations differs with forcing amplitude. The jagged kinks occurring in Fig. 4.6 appear in the phase space when there is a sharp cusp, such as in the green curve, or when the trajectory appears to cross itself, as with the loops present in the red curve. The blue curve traces out a near ellipse that is characteristic of a linear oscillator.

The total microscopic pressure, $P^{\mathrm{I}}_{\mathrm{total}} = P_{\mathrm{I}} + P^{\mathrm{I}}_{\mathrm{M}} - P_{\infty}$, is plotted in Fig. 4.7(a), where zoomed in plots for $p_0 = 0.5$ MPa and $p_0 = 1.9$ MPa are once again shown in Fig. 4.7(b) and (c), respectively. For $p_0 = 0.5$ MPa,

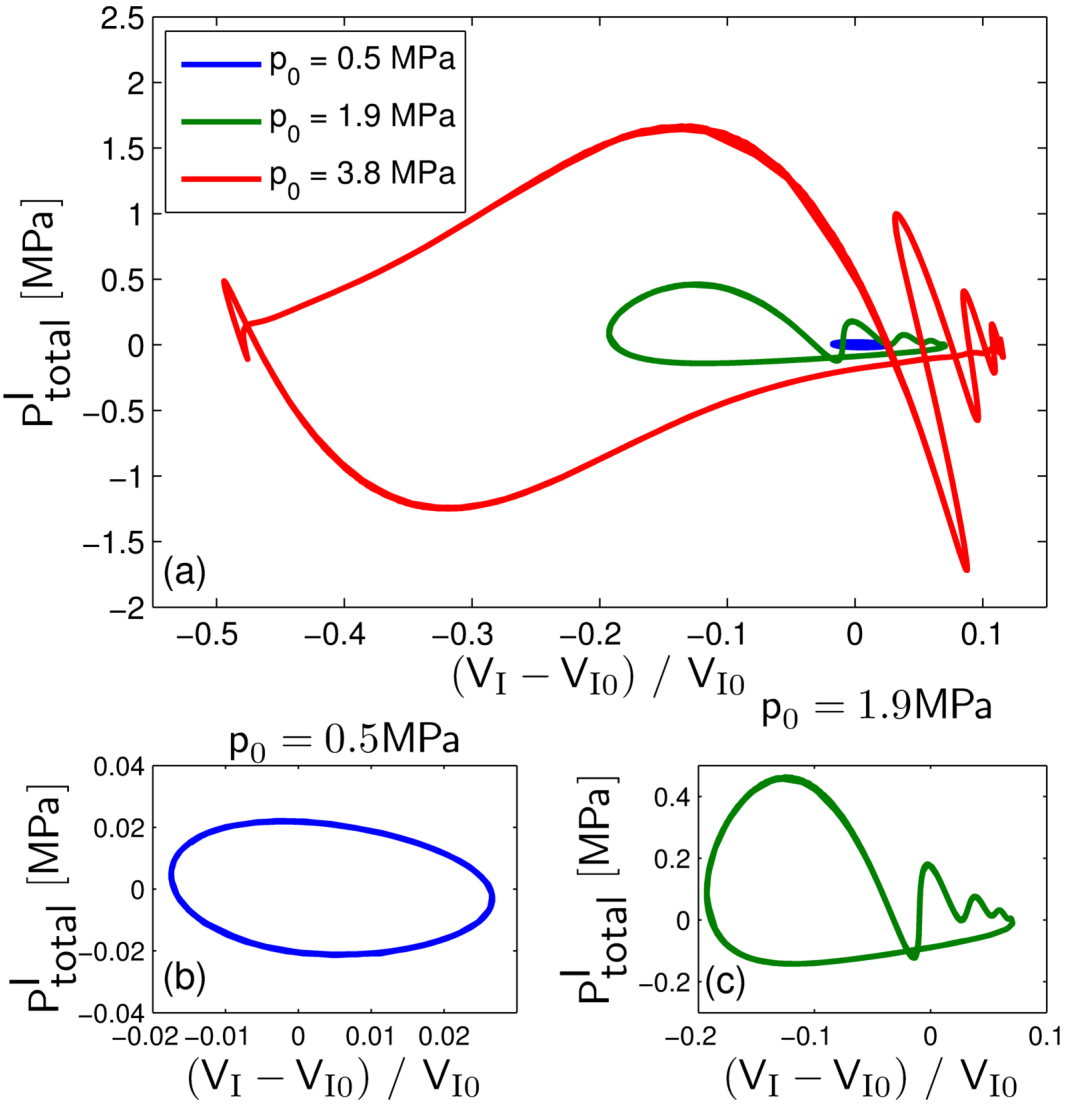

Figure 4.7: Total pressure of SAMM inclusion versus volumetric strain for $p_0 = 0.5$ MPa, $p_0 = 1.9$ MPa, and $p_0 = 3.8$ MPa and $Q_{\text{I}} = 2$.

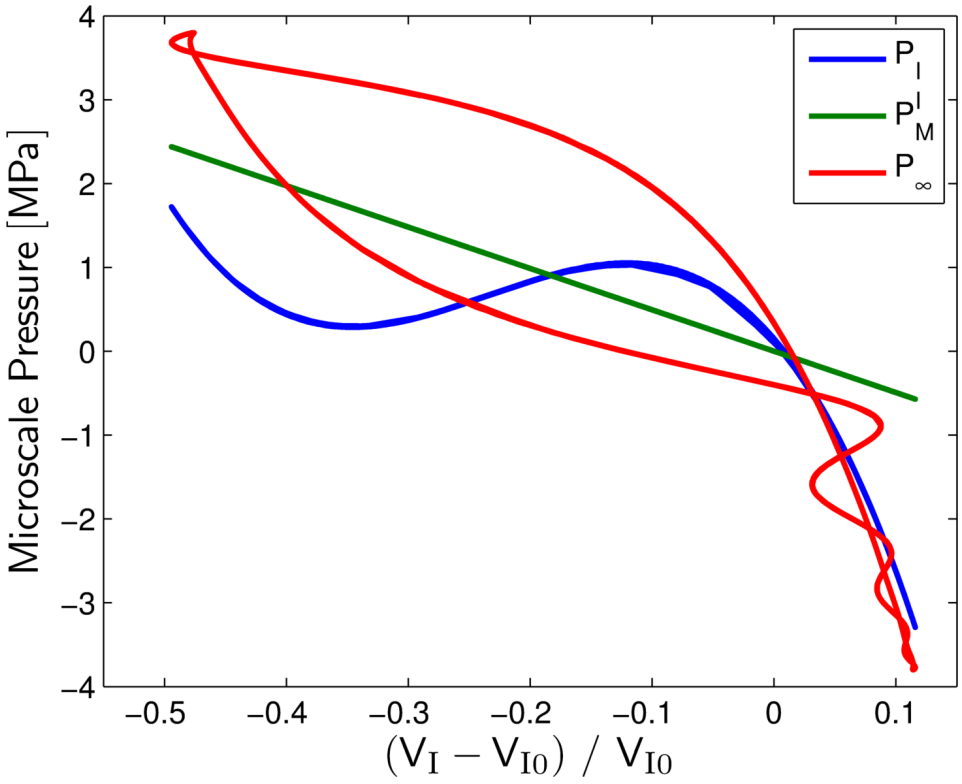

Figure 4.8: Pressure due to a single SAMM inclusion, the matrix on the surface of the SAMM inclusion, and the forcing pressure at infinity versus volumetric strain for $p_0 = 3.8$ MPa and $Q_{\text{I}} = 2$.

the total pressure as a function of volumetric strain is very nearly an ellipse, further indicating a linear response. As the pressure increases, so does the area traced out by the total pressure curve. The area is representative of the damping associated with one single SAMM inclusion. Therefore, the more nonlinear the SAMM inclusion response, the larger the area traced out by the total pressure and the more energy dissipated.

It is informative to examine the partial pressures that contribute to the

total pressure plotted in Fig. 4.7. The pressure due to the SAMM inclusion, P_{I}, pressure due to the matrix at the surface of the inclusion, $P_{\mathrm{M}}^{\mathrm{I}}$, and pressure at infinity, P_{∞}, are all plotted in Fig. 4.8 for $p_0 = 3.8$ MPa. As described earlier, the amplitude of the acoustic drive pressure is large enough to force the SAMM inclusion to operate about the fully cubic nonlinear constitutive curve, shown in blue. The non-monotonic response clearly indicates regimes of both positive and negative stiffness. The effects of the shear pressure due to the matrix is shown in green and is linear as expected. The magnitude of $P_{\mathrm{M}}^{\mathrm{I}}$ is of comparable magnitudes to P_{I}, indicating that even for a nearly incompressible matrix with $\nu = 0.4991$, the effects of shear can be fairly significant depending on the SAMM inclusion microstructure. The red curve represents the sinusoidal forcing function. While the center area is somewhat ellipsoidal, the oscillatory features for a volumetric strain greater than 0 and near -0.5 corresponding to the transient behavior due to the fast time scale.

4.3.2 Effective Medium with SAMM Inclusions

It is difficult to obtain a clear dynamic response when considering both the microscale and macroscale because of the difference in magnitudes between the two length scales. The acoustic driving pressure amplitude must be large in order to induce an observable deformation. However, even if the resulting plots showed a change in volume, the nonlinear behavior may still be difficult to see. Therefore, the following plots show the response of the effective medium with $Q_{\mathrm{I}} = 2$ at just the higher pressure amplitude, $p_0 = 3.8$ MPa.

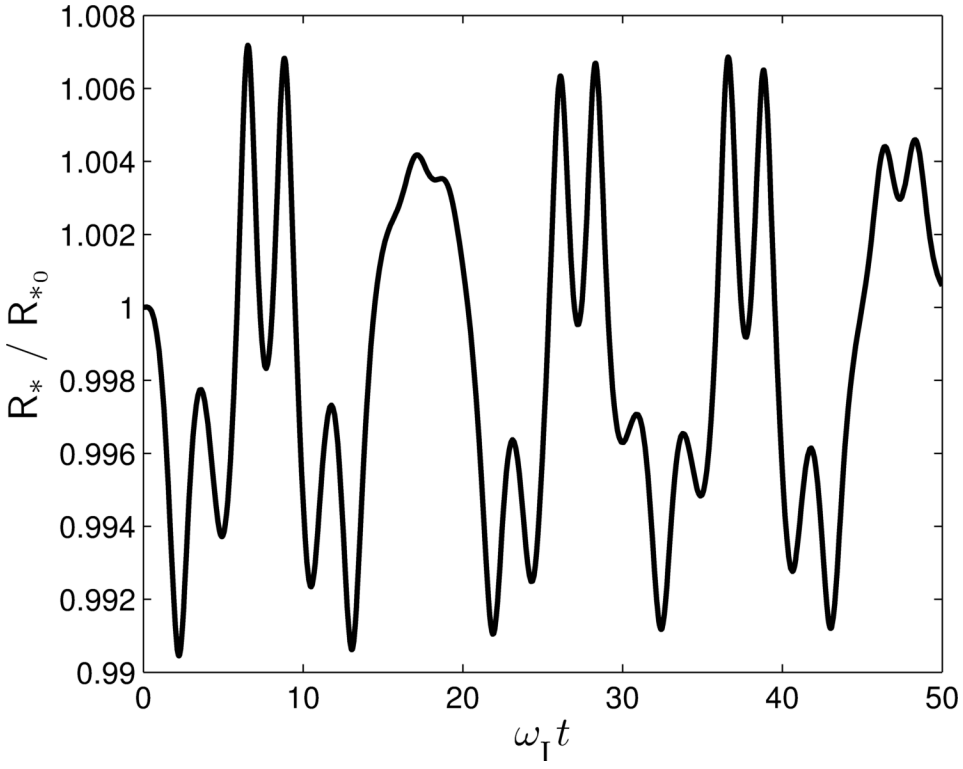

Figure 4.9: Normalized radius of the effective medium versus dimensionless time for $p_0 = 3.8$ MPa and $Q_{\text{I}} = 2$.

The instantaneous radius normalized by the equilibrium radius for the effective medium is plotted as a function of dimensionless time, $\omega_{\text{I}}t$ in Fig. 4.9. For the time scale considered, the overall response has jagged oscillations, which are non-periodic and suggestive of chaos. The pressure amplitude also induces very small changes in radius for the effective medium in comparison to the changes observed for the single SAMM inclusion as shown in Fig. 4.5. Further reducing the quality factor will smooth out the random-like oscillations to induce a steady state behavior. Additionally, the oscillations are once again

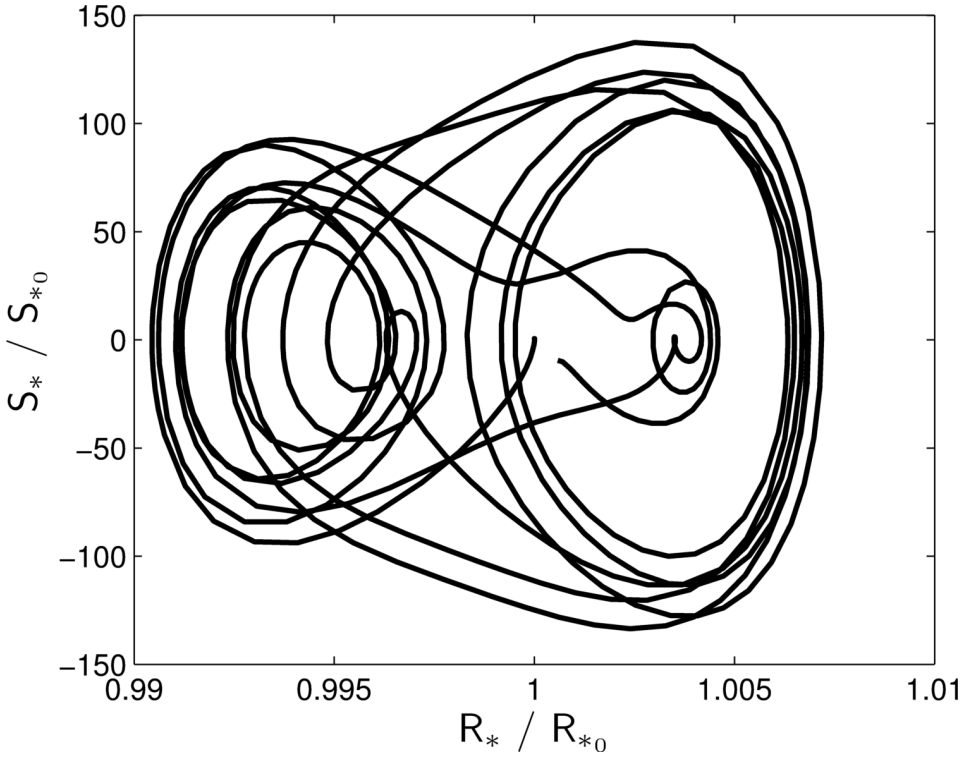

Figure 4.10: Normalized velocity versus normalized radius of the effective medium for $p_0 = 3.8$ MPa and $Q_{\text{I}} = 2$.

non-symmetric about $R_* = R_{*_0}$.

The normalized velocity versus normalized radius for the effective medium is shown in Fig. 4.10. The nature of the macroscale oscillations suggesting chaos is more readily apparent from this figure. Since the two-dimensional phase space does not periodically trace over itself, the motion does not repeat like it does for a single SAMM inclusion. Decreasing damping would smooth out these oscillations to induce a more recurrent motion for the effective medium as a whole.

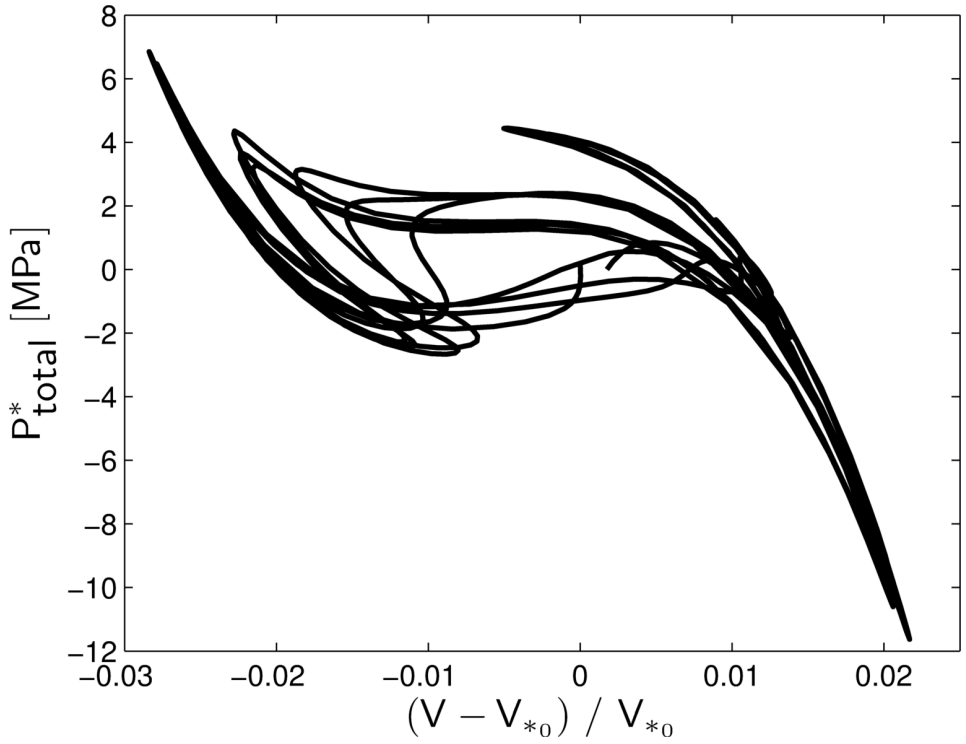

Figure 4.11: Total macroscopic pressure for effective medium versus volumetric strain for $p_0 = 3.8$ MPa and $Q_{\text{I}} = 2$.

The total macroscopic pressure, $P^*_{\text{total}} = P_* + P^*_{\text{M}} - P_\infty$, is plotted as a function of the macroscopic volumetric strain in Fig. 4.11. The macroscopic volumetric strain is an order of magnitude smaller than then microscopic volumetric strain. A change in volume as small as 3% for the effective medium induces large displacements for each SAMM inclusion that correspond to microscopic volumetric strain values as large as 50%. Despite the small deformations on the macroscale, the response still corresponds to a cubic nonlinear constitutive relationship. Once again, the area traced out by this curve corresponds to the total energy dissipated. However, the non-periodic dynamic

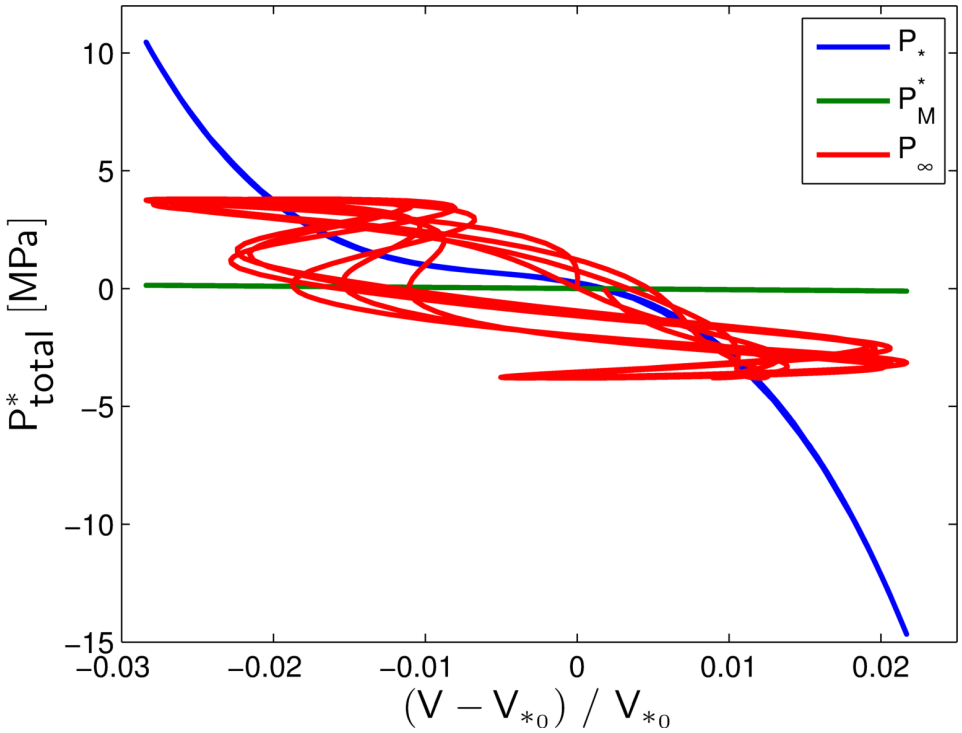

Figure 4.12: Pressure due to a the effective medium, the matrix at the effective medium boundary, and the forcing pressure at infinity versus volumetric strain for $p_0 = 3.8$ MPa and $Q_{\text{I}} = 2$.

response means that the total pressure does not trace out the same curve every 'cycle'. Herein lies the difficulty of quantifying the loss with nonlinear elasticity; the irregular response is difficult to track. The area traced out by each curve over one cycle is thus summed to obtain the total energy dissipated.

Figure 4.12 presents each pressure that contributes to the total pressure on the macroscale separately. The blue curve is a monotonic, cubic constitutive curve for the effective medium, corresponding to P_*. Locally, the slope is always negative, indicating positive stiffness that represents a stable hetero-

geneous material. The green curve shows shear effects of the matrix at the surface of the effective medium. On this scale, the magnitude of P_{M}^{*} appears to be zero, illustrating that it is negligibly small in comparison to P_{*} and P_{∞}. The chaotic response manifests itself in the acoustic driving pressure, P_{∞}, due to the time dependence.

4.3.3 Comparing Effective Medium with SAMM Inclusions and Air Filled Voids

The present work only considers the energy dissipated from a qualitative standpoint. In order to understand the enhanced effects, the total macroscopic pressure for an effective medium that contains SAMM inclusions is compared with a more conventional composite, a visocelastic matrix material that contains randomly dispersed air filled voids. The composite with air filled voids is modeled using Eq. (4.24), with the higher order terms $K_{*}' = 0$ and $K_{*}'' = 0$ and the static bulk modulus calculated from Eq. (3.38) with $K_{\text{I}} = 1.01\,(10^{5})$. The void fraction is still $\phi = 1\%$ with $N = 20$ air filled voids within a matrix with the same properties, K_{M}, ν_{M}, and η_{M}, considered for the effective medium with SAMM inclusions presented in Section 4.3.2.

The total macroscopic pressure for the SAMM inclusion and composite with air filled voids with a quality factor of $Q_{\text{I}} = 0.1$ and an acoustic pressure of $p_0 = 3.8$ MPa is shown in Fig. 4.13. The total pressure for composite with air filled voids, shown in green, is an ellipse corresponding to a linear response as expected. The effective medium with SAMM inclusions, plotted in blue,

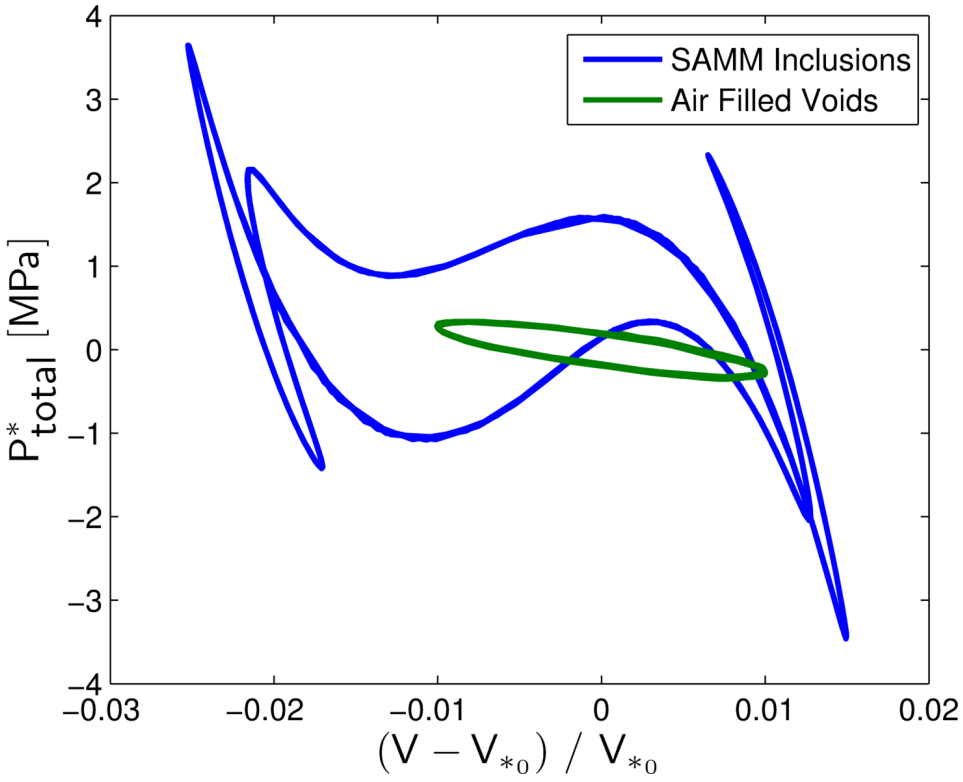

Figure 4.13: Total macroscopic pressure for an effective medium containing SAMM inclusions and composite with air filled voids versus volumetric strain for $p_0 = 3.8$ MPa and $Q_{\text{I}} = 0.1$.

traces out a much larger area than the green curve. The area traced out by the hysteresis loops is representative of the energy dissipated within the system. Therefore, there is more loss in the effective medium due to the SAMM inclusions. Furthermore, local approximations of stiffness for small disturbances can be obtained from Fig. 4.13. The composite with air filled voids represented by the green curve lies more vertical than the effective medium with SAMM inclusions, denoted by the blue curve. The steeper slope is indicative of a higher local stiffness. Therefore, a heterogeneous medium with SAMM

inclusions qualitatively demonstrates both a higher local stiffness and the dissipation of more energy than its equivalent counterpart containing the same volume fraction of air filled voids. However, the dissipation of energy is only considered in a qualitative manner. Future work aims to quantify how much energy is dissipated in a heterogeneous material containing SAMM inclusions through some loss metric.

4.4 Discussion

The present chapter detailed a decoupled model for the SAMM inclusion and a heterogeneous material containing SAMM inclusions that allowed the dynamics of each system to be obtained independently. While this nonlinear dynamic behavior is worth examining, the analysis here includes a variety of simplifying assumptions that overlook some physical details of the SAMM inclusion, most of which are due to decoupling the microscale and macroscale. In reality, the oscillations of the SAMM inclusions will generate dissipation within the effective medium, making it unrealistic to ignore dissipation with the sphere that describes the macroscale. An additional damping term must be added to Eq. (4.14) to account for energy dissipated by N SAMM inclusions. Furthermore, the pressure imposed on the surface of the effective medium will also influence the microscale. Thus the total pressure on the surface of the inclusion, $P^{\mathrm{I}}_{\mathrm{total}}$, will also include the effects of pressure due to the matrix on the surface of the effective medium, P^{*}_{M}, and pressure due to the homogenized medium itself, P_{*}. By implementing these additions into the governing

Rayleigh-Plesset type equation, the dynamics of the SAMM inclusion affect the behavior of the effective medium and vice versa. It is worth noting regardless of these additions to the models, the effective parameters, K_*, K'_* and K''_*, are still obtained in the quasi-static limit via the Hashin-Shtrikman method from Section 3.2.2.

Furthermore, the linear and nonlinear stiffness of both the SAMM inclusion and effective medium vary locally as a function of volumetric strain, or radius, and a more accurate model would account for this. It is more difficult, however, to utilize the locally changing coefficients with a decoupled model. The use of locally varying stiffness, instead of the global parameters considered in the present chapter, will thus be implemented in future work with the coupled system.

Another way to improve the model is to account for the mass of the SAMM inclusion, which would add additional terms to obtain a governing differential equation similar to that presented in Ref. [101]. The mass for the effective medium could also be accounted for in the same way. The addition of the mass terms could be used with the decoupled model presented throughout the chapter, as well as the proposed coupled model to be investigated in future work.

The behavior demonstrated by the effective medium is qualitatively what was expected—a matrix containing SAMM inclusions was qualitatively stiffer with a higher damping capacity than the same matrix with air filled voids. However, a quantitative metric of characterizing the dissipation of en-

ergy is desired to further understand the enhanced damping ability associated with the SAMM inclusions. The goal is to develop a model to accurately understanding the dynamic behavior associated with the SAMM inclusions and thus future work will investigate these simplifying assumptions in more detail to determine their effects on the nonlinear material response.

Chapter 5

Conclusion

5.1 Summary

The study of acoustic metamaterials has emerged in recent years as a field of high interest because they offer the possibility to obtain material properties outside the limits of those available with conventional materials. The exotic properties may result in an increased ability to manipulate or tailor the response of acoustic waves and lead to improved acoustic technologies, such as superlenses, acoustic cloaks, phononic switches, and so forth. The present thesis studied one specific type of acoustic metamaterial, known as a snapping acoustic metamaterial, or SAMM, which possesses local regimes of negative stiffness and effective material nonlinearity. The analysis builds upon FEM used to describe the SAMM inclusions. Techniques are adapted from nonlinear elasticity and nonlinear acoustics in order to develop analytical models to investigate the behavior of the SAMM inclusions of interest. The following paragraphs provide a detailed summary of the work presented in each chapter.

Chapter 2 focused exclusively on the quasi-static elastic response of the SAMM inclusions. The pressure-volumetric strain constitutive relation-

ship for the SAMM inclusions was described using small perturbations about imposed pre-strains. The approximation gives rise to strain-dependent linear contributions to the SAMM stiffness that may be either positive or negative, as well as high order stiffness terms that may induce hysteretic snapping. The deformation of the representative SAMM element was shown through the pressure-volumetric strain constitutive relationship and local stiffness parameters to provide insight into the response that could be obtained with the SAMM inclusions.

Chapter 3 provided a great amount of detail on modeling an effective medium containing a dilute concentration of non-interacting SAMM inclusions. Two homogenization techniques were applied to obtain estimates of the effective stiffness and acoustic nonlinearity of the heterogeneous material. The first method adapted a mixture law, but the subsequent response provided unbounded acoustic parameters of nonlinearity resulting from the instability of the effective medium predicted by this simple model. The inaccurate prediction of the mixture law is due to the assumption that all materials in the mixture offer no resistance to shear deformation. A second homogenization scheme was therefore developed to address the shortcomings of the mixture law. The second model modified the derivation of the linear Hashin-Shtrikman bounds to include the effects of nonlinear elasticity. This model permitted certain values of the shear modulus of the matrix to stabilize the effective medium by constraining the SAMM inclusion in the locally negative stiffness regime. The results presented in Chapter 3 indicate that the effective medium can simulta-

neously exhibit large but bounded quadratic and cubic material nonlinearity. Analysis of propagating waves in the presence of strong cubic nonlinearities requires extending many of the standard nonlinear acoustics techniques to third order. The work presented in this thesis therefore analyzed state equations, one-dimensional wave equations, and the shock formation distance for a wave propagating in media with quadratic and cubic nonlinearities. Examples of wave distortion for a traveling plane wave for several cases of quadratic and cubic nonlinearity and a small amount of thermoviscous absorption were provided to illustrate the responses that could be obtained with the SAMM inclusions.

Chapter 4 developed a model to study the forced nonlinear oscillations of a SAMM inclusion and an effective medium consisting of a continuous matrix with a dilute concentration of SAMM inclusions. The governing differential equation is of the same form as the Rayleigh-Plesset equation that is commonly used to study the dynamics of bubbles. A dimensionless form of the equation was numerically integrated for both a single SAMM inclusion and the effective medium. The matrix material considered had a shear modulus large enough to fully constrain the negative stiffness regime of the SAMM inclusion. The single SAMM inclusion was described using global parameters, and the subresonant response for different forcing amplitudes were compared. All three forcing amplitudes showed a periodic, steady state response that exhibited large deformations on the microscale, but the snapping was only present for the largest amplitude. The effective medium model also utilized global ef-

fective parameters, which correspond to the same properties used to describe the matrix and SAMM inclusion in the single SAMM inclusion dynamics case. The simulation for dynamics of the effective medium revealed a chaos-like response. The macroscale deformations were smaller, but still corresponded to a cubically nonlinear effective medium. When a composite containing SAMM inclusions was compared to a composite containing air filled voids, the former was found to qualitatively dissipate more energy.

Although the behavior studied throughout this thesis is limited to the analysis of one representative SAMM inclusion, the response shown throughout Chapters 2–4 is as anticipated. The analyses may also be generalized to different SAMM inclusion geometries, assuming the constitutive behavior demonstrate regions of negative curvature of the strain energy response due to an imposed deformation. The acoustic nonlinearities of a medium containing a low volume fraction of SAMM incsluions are shown to be much larger than for most conventional materials, particularly with respect to cubic nonlinearity. It is important to note that the strain regions where one observes enhanced acoustic nonlinearity correspond to microscopic negative stiffness behavior that is stabilized by the surrounding elastic matrix material. One observes that different regions of the nonlinear response give rise to a variety of combinations for the quadratic and cubic nonlinearity, which can be either positive or negative. Furthermore, the effective medium was also shown to have an increased damping capacity. Although more research on the behavior is necessary, the present thesis indicates that the SAMM inclusions studied

may be used to address some of the limitations commonly encountered with conventional materials and therefore merit further investigation.

5.2 Future Work

The research presented here marks an initial investigation into the unique nonlinear acoustic and dynamic response of a specific design for a nonlinear snapping acoustic metamaterial. Therefore, there is a great deal left to understand regarding the behavior of acoustic metamaterial elements with engineered instabilities, some of which have been acknowledged throughout the preceding chapters of the present thesis. The theoretical modeling tools developed here were only applied to one specific SAMM inclusion. Altering the material properties and sub-wavelength geometry of the microstructures may perhaps lead to a different response for all of the computational results presented in Chapters 2–4. For example, the acoustic nonlinearity attainable may be further enhanced, a stiffer (or softer) matrix may be required to fully constrain the negative stiffness regime on the microscale, or different amplitudes of acoustic pressure would be necessary to elicit a desired acoustic or dynamic response. The effective medium was also limited to a low volume fraction of SAMM inclusions. For a heterogeneous material with a higher volume fraction of SAMM inclusions, interactions between the inclusion would need to be accounted for. A more complicated analytical model may be considered in the future to capture the higher order scattering effects.

Specific limitations with the nonlinear dynamics model detailed in Chap-

ter 4 were already outlined in Section 4.4, and future work aims to address them through more complicated models that quantifies the energy dissipated. Of highest interest is a coupled model that accounts for additional dissipation on the macroscale due to the individual SAMM inclusion and the contributions of the pressure at the effective medium-matrix interface at the microscale. The model can then incorporate nonlinear stiffness parameters that vary locally as a function of strain. Other future models will also include mass terms in the Rayleigh-Plesset type equation for the SAMM inclusion. Note that the future models will still be limited to an effective medium in the quasi-static regime that is described through the Hashin-Shtrikman method. A different effective medium theory is required to account for the resonant effects.

Further understanding of the response of the SAMM inclusions and a heterogeneous material containing them will allow these metamaterials to be applied to specific applications through the creation of physical systems and devices. Experimental verification of the acoustic nonlinearities and damping capacity of an effective medium containing the SAMM inclusions is therefore necessary. The analytic models provided throughout this thesis can also be compared to finite element models to verify their validity. Overall, the models developed here serve as tools to understand the influence of the nonlinear microscale material behavior in an effort to design and physically create composites with enhanced macroscopic properties in terms of nonlinearity, stiffness and damping capacity in the future.

Appendices

Appendix A

Derivation of Lossy Wave Equation with Quadratic and Cubic Nonlinearity

A.1 Wave Equation

The three-dimensional, lossy wave equation up to third order with respect to nonlinearity is derived from conservation of mass,

$$\frac{\partial \rho}{\partial t} + \nabla \cdot (\rho \boldsymbol{u}) = 0, \tag{A.1}$$

conservation of momentum, including losses due to bulk viscosity, μ_{B}, and shear viscosity, μ,

$$\nabla p + \rho \frac{\partial \boldsymbol{u}}{\partial t} + \rho \boldsymbol{u} \cdot \nabla \boldsymbol{u} = \mu \nabla^2 \boldsymbol{u} + \left(\mu_{\text{B}} + \frac{1}{3} \mu \right) \nabla \left(\nabla \cdot \boldsymbol{u} \right), \tag{A.2}$$

and the equation of state given in [67],

$$\begin{aligned} \rho' = \frac{p}{c_0^2} - \frac{1}{\rho_0 c_0^4} \left(\frac{B}{2A} \right) p^2 - \frac{1}{\rho_0^2 c_0^6} \left[\frac{C}{6A} - \frac{1}{2} \left(\frac{B}{A} \right)^2 \right] p^3 \\ - \frac{\kappa}{\rho_0 c_0^4} \left(\frac{1}{c_v} - \frac{1}{c_p} \right) \frac{\partial p}{\partial t}. \end{aligned} \tag{A.3}$$

Equation (A.3) differs from Eq. (3.4) because there is a Taylor expansion with respect to entropy in addition to the expansion with respect to density, which gives rise to the loss through the thermal conductivity, κ, isobaric specific

heat, c_p, and isochoric specific heat, c_v. Expressing Eq. (A.1) in terms of excess density provides

$$\frac{\partial \rho'}{\partial t} + \rho_0 \nabla \cdot \boldsymbol{u} = -\rho' \nabla \cdot \boldsymbol{u} - \boldsymbol{u} \cdot \nabla \rho'. \tag{A.4}$$

The medium is assumed to be linear with respect to losses and up to third order with respect to nonlinearity. Substituting Eq. (A.3) into Eq. (A.4) eliminates excess density from conservation of mass to obtain

$$\begin{aligned} &\frac{1}{c_0^2}\frac{\partial p}{\partial t} - \frac{1}{\rho_0 c_0^4}\left(\frac{B}{2A}\right)\frac{\partial p^2}{\partial t} - \frac{1}{\rho_0^2 c_0^6}\left[\frac{C}{6A} - \frac{1}{2}\left(\frac{B}{A}\right)^2\right]\frac{\partial p^3}{\partial t} \\ &\quad - \frac{\kappa}{\rho_0 c_0^4}\left(\frac{1}{c_v} - \frac{1}{c_p}\right)\frac{\partial^2 p}{\partial t^2} + \rho_0 \nabla \cdot \boldsymbol{u} = -\frac{p}{c_0^2}\nabla \cdot \boldsymbol{u} \\ &\quad + \frac{1}{\rho_0 c_0^4}\left(\frac{B}{2A}\right) p^2 \nabla \cdot \boldsymbol{u} - \frac{1}{c_0^2}\boldsymbol{u} \cdot \nabla p + \frac{1}{\rho_0 c_0^4}\left(\frac{B}{2A}\right)\boldsymbol{u} \cdot \nabla p^2. \end{aligned} \tag{A.5}$$

The following two vector identities

$$\boldsymbol{u} \cdot \nabla \boldsymbol{u} = \frac{1}{2}\nabla u^2 - \boldsymbol{u} \times \nabla \times \boldsymbol{u}$$

$$\nabla\left(\nabla \cdot \boldsymbol{u}\right) = \nabla u^2 - \nabla \times \nabla \times \boldsymbol{u},$$

are used with $u^2 = \boldsymbol{u} \cdot \boldsymbol{u}$ to express conservation of momentum in terms of excess density, as given by

$$\begin{aligned} \nabla p + \rho_0 \frac{\partial \boldsymbol{u}}{\partial t} = &-\rho' \frac{\partial \boldsymbol{u}}{\partial t} - \frac{\rho_0}{2}\nabla u^2 - \frac{\rho'}{2} \cdot \nabla u^2 + \left(\mu_{\text{B}} + \frac{4}{3}\mu\right)\nabla^2 \boldsymbol{u} \\ &+ \rho_0 \boldsymbol{u} \times \nabla \times \boldsymbol{u} + \rho' \boldsymbol{u} \times \nabla \times \boldsymbol{u} \\ &- \left(\mu_{\text{B}} + \frac{1}{3}\mu\right)\nabla \times \nabla \times \boldsymbol{u}. \end{aligned} \tag{A.6}$$

The velocity $\boldsymbol{u}$ for small disturbances can be expressed as the superposition of three modes—acoustic, vorticity and entropy [90]. The last three terms in Eq. (A.6) correspond to vorticity field in linear theory, which are negligibly small unless within a thermoviscous boundary layer. If the boundary layer thickness is much smaller than the acoustic wavelength, the last three terms of Eq. (A.6) can be discarded, giving

$$\nabla p + \rho_0 \frac{\partial \boldsymbol{u}}{\partial t} = -\rho' \frac{\partial \boldsymbol{u}}{\partial t} - \frac{\rho_0}{2} \nabla u^2 - \frac{\rho'}{2} \cdot \nabla u^2 + \left(\frac{4}{3}\mu + \mu_{\text{B}} \right) \nabla^2 \boldsymbol{u}. \tag{A.7}$$

See Ref. [90] for further details. Substituting Eq. (A.3) into Eq. (A.7), gives

$$\begin{aligned} \nabla p + \rho_0 \frac{\partial \boldsymbol{u}}{\partial t} = &\left[-\frac{p}{c_0^2} + \frac{1}{\rho_0 c_0^4} \left(\frac{B}{2A} \right) p^2 \right] \frac{\partial \boldsymbol{u}}{\partial t} - \frac{\rho_0}{2} \nabla u^2 \\ &- \frac{p}{2c_0^2} \nabla u^2 + \left(\frac{4}{3}\mu + \mu_{\text{B}} \right) \nabla^2 \boldsymbol{u}. \end{aligned} \tag{A.8}$$

Conservation of mass and momentum are combined into one wave equation by subtracting the time derivative of Eq. (A.5) from the divergence of Eq. (A.8):

$$\begin{aligned} &\nabla^2 p - \frac{1}{c_0^2} \frac{\partial^2 p}{\partial t^2} + \frac{1}{\rho_0 c_0^4} \left(\frac{B}{2A} \right) \frac{\partial^2 p^2}{\partial t^2} + \frac{1}{\rho_0^2 c_0^6} \left[\frac{C}{6A} - \frac{1}{2} \left(\frac{B}{A} \right)^2 \right] \frac{\partial^2 p^3}{\partial t^2} \\ &\quad + \frac{\kappa}{\rho_0 c_0^4} \left(\frac{1}{c_v} - \frac{1}{c_p} \right) \frac{\partial^3 p}{\partial t^3} - \left(\frac{4}{3}\mu + \mu_{\text{B}} \right) \nabla^2 \left(\nabla \cdot \boldsymbol{u} \right) \\ &= \nabla \cdot \left[-\frac{p}{c_0^2} + \frac{1}{\rho_0 c_0^4} \left(\frac{B}{2A} \right) p^2 \right] \frac{\partial \boldsymbol{u}}{\partial t} - \frac{\rho_0}{2} \nabla^2 u^2 - \nabla \cdot \frac{p}{2c_0^2} \nabla u^2 \\ &\quad + \frac{\partial}{\partial t} \left(\frac{p}{c_0^2} \nabla \cdot \boldsymbol{u} \right) - \frac{1}{\rho_0 c_0^4} \left(\frac{B}{2A} \right) \frac{\partial}{\partial t} \left(p^2 \nabla \cdot \boldsymbol{u} \right) \\ &\quad + \frac{1}{c_0^2} \frac{\partial}{\partial t} \left(\boldsymbol{u} \cdot \nabla p \right) - \frac{1}{\rho_0 c_0^4} \left(\frac{B}{2A} \right) \frac{\partial}{\partial t} \left(\boldsymbol{u} \cdot \nabla p^2 \right). \end{aligned} \tag{A.9}$$

The wave equation given in Eq. (A.9) can be rewritten as

$$\begin{aligned}
&\nabla^2 p - \frac{1}{c_0^2}\frac{\partial^2 p}{\partial t^2} + \frac{\kappa}{\rho_0 c_0^4}\left(\frac{1}{c_v} - \frac{1}{c_p}\right)\frac{\partial^3 p}{\partial t^3} - \left(\frac{4}{3}\mu + \mu_{\text{B}}\right)\nabla^2\left(\nabla\cdot\boldsymbol{u}\right) \\
&\quad = -\frac{1}{\rho_0 c_0^4}\left(\frac{B}{2A}\right)\frac{\partial^2 p^2}{\partial t^2} - \frac{1}{\rho_0^2 c_0^6}\left[\frac{C}{6A} - \frac{1}{2}\left(\frac{B}{A}\right)^2\right]\frac{\partial^2 p^3}{\partial t^2} \\
&\qquad + \frac{\partial}{\partial t}\nabla\cdot\left[\frac{p\boldsymbol{u}}{c_0^2} - \left(\frac{B}{2A}\right)\frac{p^2\boldsymbol{u}}{\rho_0 c_0^2}\right] - \frac{\rho_0}{2}\nabla^2 u^2 - \nabla\cdot\frac{p}{2c_0^2}\nabla u^2 \\
&\qquad + \nabla\cdot\left[-\frac{p}{c_0^2} + \frac{1}{\rho_0 c_0^4}\left(\frac{B}{2A}\right)p^2\right]\frac{\partial \boldsymbol{u}}{\partial t}.
\end{aligned} \tag{A.10}$$

The last term in Eq. (A.10), $\partial\boldsymbol{u}/\partial t$, can be rewritten by solving for $\partial\boldsymbol{u}/\partial t$ in Eq. (A.8) and retaining only lossless terms up to second order in pressure. This is the same recursion method outlined in Section 3.1.1 used to find Eqs. (3.4) and (3.7). The expression for $\partial\boldsymbol{u}/\partial t$ is

$$\frac{\partial \boldsymbol{u}}{\partial t} = -\frac{1}{\rho_0}\nabla p + \frac{p}{\rho_0^2 c_0^2}\nabla p - \frac{1}{2}\nabla u^2. \tag{A.11}$$

Equation (A.10) then becomes

$$\begin{aligned}
&\nabla^2 p - \frac{1}{c_0^2}\frac{\partial^2 p}{\partial t^2} + \frac{\kappa}{\rho_0 c_0^4}\left(\frac{1}{c_v} - \frac{1}{c_p}\right)\frac{\partial^3 p}{\partial t^3} - \left(\frac{4}{3}\mu + \mu_{\text{B}}\right)\nabla^2\left(\nabla\cdot\boldsymbol{u}\right) \\
&\quad = -\frac{1}{\rho_0 c_0^4}\left(\frac{B}{2A}\right)\frac{\partial^2 p^2}{\partial t^2} - \frac{1}{\rho_0^2 c_0^6}\left[\frac{C}{6A} - \frac{1}{2}\left(\frac{B}{A}\right)^2\right]\frac{\partial^2 p^3}{\partial t^2} \\
&\qquad + \frac{\partial}{\partial t}\nabla\cdot\left[\frac{p\boldsymbol{u}}{c_0^2} - \left(\frac{B}{2A}\right)\frac{p^2\boldsymbol{u}}{\rho_0 c_0^2}\right] \\
&\qquad + \nabla^2\left[\frac{p^2}{2\rho_0 c_0^2} - \frac{\rho_0^2 u^2}{2} + \left(1 + \frac{B}{2A}\right)\frac{p^3}{3\rho_0 c_0^4}\right].
\end{aligned} \tag{A.12}$$

If the loss terms in Eq. (A.12) are neglected, this wave equation is identical to that presented in Ref. [89].

Because the propagation of plane progressive waves in one direction is of interest, Eq. (A.12) can be reduced to a function of pressure alone. The second order impedance relationship between pressure and velocity is [3]

$$p = \rho_0 c_0 u + \frac{1}{2}\left(1 + \frac{B}{2A}\right)\rho_0 u^2. \tag{A.13}$$

An expression for velocity as a function of pressure is easily obtained by solving for u and substituting the expansion for u into the higher order terms, such that

$$u = \frac{p}{\rho_0 c_0} - \frac{1}{2}\left(1 + \frac{B}{2A}\right)\frac{p^2}{\rho_0^2 c_0^3}. \tag{A.14}$$

The one dimensional wave equation then becomes

$$\begin{aligned}
&\frac{\partial^2 p}{\partial x^2} - \frac{1}{c_0^2}\frac{\partial^2 p}{\partial t^2} + \frac{\kappa}{\rho_0 c_0^4}\left(\frac{1}{c_v} - \frac{1}{c_p}\right)\frac{\partial^3 p}{\partial t^3} - \left(\frac{4}{3}\mu + \mu_{\text{B}}\right)\frac{\partial^3 u}{\partial x^3} \\
&\quad = -\frac{1}{\rho_0 c_0^4}\left(\frac{B}{2A}\right)\frac{\partial^2 p^2}{\partial t^2} - \frac{1}{\rho_0^2 c_0^6}\left[\frac{C}{6A} - \frac{1}{2}\left(\frac{B}{A}\right)^2\right]\frac{\partial^2 p^3}{\partial t^2} \\
&\qquad + \frac{\partial^2}{\partial t \partial x}\left[\frac{p^2}{\rho_0 c_0^3} - \left(\frac{1}{2} + \frac{3B}{4A}\right)\frac{p^3}{\rho_0^2 c_0^5}\right] + \left(\frac{5}{6} + \frac{5B}{12A}\right)\frac{p^2}{3\rho_0 c_0^4}\frac{\partial^2 p}{\partial x^2}.
\end{aligned} \tag{A.15}$$

A relation derived from Eqs. (A.11) and (A.13),

$$\frac{\partial p}{\partial x} = -\frac{1}{c_0}\frac{\partial p}{\partial t} + \frac{1}{\rho_0 c_0^3}\left(1 + \frac{B}{2A}\right)\frac{\partial p}{\partial t}, \tag{A.16}$$

the lossless wave equation,

$$\frac{\partial^2 p}{\partial x^2} = \frac{1}{c_0^2}\frac{\partial^2 p}{\partial t^2}, \tag{A.17}$$

and a relation derived from Eqs. (A.16) and (A.17),

$$\frac{\partial^3 u}{\partial x^3} = -\frac{1}{\rho_0 c_0^4}\frac{\partial^3 p}{\partial t^3}, \tag{A.18}$$

are used to derive the one dimensional wave equation, only as a function of pressure, given by

$$\frac{\partial^2 p}{\partial x^2} - \frac{1}{c_0^2}\frac{\partial^2 p}{\partial t^2} + \frac{1}{c_0^4}\left[\frac{1}{\rho_0}\left(\frac{4}{3}\mu + \mu_{\text{B}}\right) + \frac{\kappa}{\rho_0}\left(\frac{1}{c_v} - \frac{1}{c_p}\right)\right]\frac{\partial^3 p}{\partial t^3} = -\frac{1}{\rho_0 c_0^4}\left(1 + \frac{B}{2A}\right)\frac{\partial^2 p^2}{\partial t^2} - \frac{1}{\rho_0^2 c_0^6}\left[\frac{C}{6A} - \frac{1}{2}\left(\frac{B}{A}\right)^2 - \frac{7B}{6A} - \frac{4}{3}\right]\frac{\partial^2 p^3}{\partial t^2} \tag{A.19}$$

or

$$\frac{\partial^2 p}{\partial x^2} - \frac{1}{c_0^2}\frac{\partial^2 p}{\partial t^2} + \frac{\delta}{c_0^4}\frac{\partial^3 p}{\partial t^3} = -\frac{\beta}{\rho_0 c_0^4}\frac{\partial^2 p^2}{\partial t^2} - \frac{2\gamma}{3\rho_0^2 c_0^6}\frac{\partial^2 p^3}{\partial t^2}, \tag{A.20}$$

where the diffusivity of sound, δ, is

$$\delta = \frac{1}{\rho_0}\left(\frac{4}{3}\mu + \mu_{\text{B}}\right) + \frac{\kappa}{\rho_0}\left(\frac{1}{c_v} - \frac{1}{c_p}\right), \tag{A.21}$$

β is defined as

$$\beta = 1 + \frac{B}{2A}, \tag{A.22}$$

and γ is defined as

$$\gamma = \frac{3}{2}\left[\frac{C}{6A} - \frac{1}{2}\left(\frac{B}{A}\right)^2 - \frac{7B}{6A} - \frac{4}{3}\right]. \tag{A.23}$$

A.2 Evolution Equation

As described in Section 3.4.1, the wave equation given in Eq. (A.20) can be split into three differential equations to transform the wave equation into a one dimensional evolution equation. Consider first the lossy linear wave

equation:

$$\frac{\partial^2 p}{\partial x^2} - \frac{1}{c_0^2}\frac{\partial^2 p}{\partial t^2} = -\frac{\delta}{c_0^4}\frac{\partial^3 p}{\partial t^3}. \tag{A.24}$$

To derive the evolution equation, a slow scale is introduced with retarded time is $\tau = t - x/c_0$, and the corresponding slow scale of the spatial coordinate is $x_1 = \tilde{\epsilon}x$. The parameter, $\tilde{\epsilon}$, is on the order of both the pressure, p, and diffusivity of sound, δ. Derivatives in time t and τ are the same, such that

$$\frac{\partial^n}{\partial t^n} = \frac{\partial^n}{\partial \tau^n}, \tag{A.25}$$

but derivatives in x are now a function of x_1 and τ, such that

$$\frac{\partial}{\partial x} = \tilde{\epsilon}\frac{\partial}{\partial x_1} - \frac{1}{c_0}\frac{\partial}{\partial \tau}.$$

The second derivative with respect to x is:

$$\frac{\partial^2}{\partial x^2} = \tilde{\epsilon}^2\frac{\partial^2}{\partial x_1^2} - \frac{2\tilde{\epsilon}}{c_0}\frac{\partial^2}{\partial \tau \partial x_1} + \frac{1}{c_0^2}\frac{\partial^2}{\partial \tau^2} \tag{A.26}$$

Equation (A.24) expressed in terms of the space and time derivatives given by Eqs. (A.25) and (A.26) is

$$\tilde{\epsilon}^2\frac{\partial^2 p}{\partial x_1^2} - \frac{2\tilde{\epsilon}}{c_0}\frac{\partial^2 p}{\partial \tau \partial x_1} = -\frac{\delta}{c_0^4}\frac{\partial^3 p}{\partial \tau^3}. \tag{A.27}$$

Since p and δ are both order $\tilde{\epsilon}$, the first term on the left-hand side of Eq. (A.27) is of order $\tilde{\epsilon}^3$, while the other two terms in the equation are of order $\tilde{\epsilon}^2$. On the slow scale, only the lowest order of $\tilde{\epsilon}$ is retained and the first term on the left-hand side of Eq. (A.27) is therefore discarded. Additionally, $\partial/\partial\tau$ is common to all terms and cancels out. The wave equation is now given by

$$\frac{2\tilde{\epsilon}}{c_0}\frac{\partial p}{\partial x_1} = \frac{\delta}{c_0^4}\frac{\partial^2 p}{\partial \tau^2}.$$

After the spatial coordinate is transformed back to the coordinate x, the lossy linear wave equation reduces to

$$\frac{\partial p}{\partial x} = \frac{\delta}{2c_0^3}\frac{\partial^2 p}{\partial \tau^2}. \tag{A.28}$$

The same transformations are applied to the lossless form of Eq. (A.20) that accounts only quadraticr nonlinearities,

$$\frac{\partial^2 p}{\partial x^2} - \frac{1}{c_0^2}\frac{\partial^2 p}{\partial t^2} = -\frac{\beta}{\rho_0 c_0^4}\frac{\partial^2 p^2}{\partial t^2}. \tag{A.29}$$

Applying Eqs. (A.25) and (A.26) to Eq. (A.29) gives rise to

$$\tilde{\epsilon}^2\frac{\partial^2 p}{\partial x_1^2} - \frac{2\tilde{\epsilon}}{c_0}\frac{\partial^2 p}{\partial \tau \partial x_1} = -\frac{\beta}{\rho_0 c_0^4}\frac{\partial^2 p^2}{\partial \tau^2}. \tag{A.30}$$

Once again, only terms on the order of $\tilde{\epsilon}^2$ are retained. In terms of the coordinate, x, the second order lossless wave equation simplifies to

$$\frac{\partial p}{\partial x} = \frac{\beta p}{\rho_0 c_0^3}\frac{\partial p}{\partial \tau}. \tag{A.31}$$

The nonlinear, lossless wave equation with cubic nonlinearity

$$\frac{\partial^2 p}{\partial x^2} - \frac{1}{c_0^2}\frac{\partial^2 p}{\partial t^2} = \frac{2\gamma}{3\rho_0^2 c_0^6}\frac{\partial^2 p^3}{\partial t^2}, \tag{A.32}$$

is now transformed to the slow scale. The retarded time τ is the same but the spatial coordinate on the slow scale is now $x_2 = \tilde{\epsilon}^2 x$, where $\tilde{\epsilon}$ once again characterizes the order of pressure, p. The first derivative with respect to x is

$$\frac{\partial}{\partial x} = \tilde{\epsilon}^2\frac{\partial}{\partial x_2} - \frac{1}{c_0}\frac{\partial}{\partial \tau},$$

and the second derivative with respect to x is

$$\frac{\partial^2}{\partial x^2} = \tilde{\epsilon}^4 \frac{\partial^2}{\partial x_2^2} - \frac{2\tilde{\epsilon}^2}{c_0} \frac{\partial^2}{\partial \tau \partial x_2} + \frac{1}{c_0^2} \frac{\partial^2}{\partial \tau^2}. \tag{A.33}$$

After applying the derivatives from Eq. (A.25) and (A.33) to Eq. (A.29), the nonlinear wave equation with cubic nonlinearity on the slow scale becomes

$$\tilde{\epsilon}^4 \frac{\partial^2 p}{\partial x_2^2} - \frac{2\tilde{\epsilon}^2}{c_0} \frac{\partial^2 p}{\partial x_2 \partial \tau} = -\frac{2\gamma}{3\rho_0^2 c_0^6} \frac{\partial^2 p^3}{\partial \tau^2}. \tag{A.34}$$

Once again only the lowest order of $\tilde{\epsilon}$ is retained. Both the term on the right-hand side of Eq. (A.34) and the second term on the left-hand side are of order $\tilde{\epsilon}^3$. However, the first term is on the order of $\tilde{\epsilon}^5$ and is thus discarded. After transforming Eq. (A.34) back to the x coordinate and canceling common terms, the cubically nonlinear, lossless wave equation becomes

$$\frac{\partial p}{\partial x} = \frac{\gamma p^2}{\rho_0^2 c_0^5} \frac{\partial p}{\partial \tau}. \tag{A.35}$$

Since the time scales are the same, the right-hand side of Eqs. (A.28), (A.31) and (A.35) are added together with $\partial p/\partial x$ on the left-hand side to obtain the evolution equation for a plane progressive wave,

$$\frac{\partial p}{\partial x} = \frac{\delta}{2c_0^3} \frac{\partial^2 p}{\partial \tau^2} + \left(\frac{\beta p}{\rho_0 c_0^3} + \frac{\gamma p^2}{\rho_0^2 c_0^5} \right) \frac{\partial p}{\partial \tau}. \tag{A.36}$$

Appendix B

Harmonic Materials

A closed form solution for the deformation of harmonic materials was derived independently by both Ogden [64] and Abeyarante and Horgan [103]. The former considers Biot stress, while the latter considers Cauchy stress. Additional information can be found in Ref. [86] and the references therein. In Ref. [6], the authors considered effective moduli for a linear inclusion embedded in a nonlinear matrix undergoing nonlinear deformations. The strain energy density assumed here simplifies that presented in Ref. [6] for the nonlinear matrix to a linear medium subjected to geometrical nonlinearities. The derivations in terms of Biot stress are repeated here for convenience, and then reformulated in terms of Cauchy stress.

A reference configuration is defined by (r, θ, ϕ) and a deformed configuration is defined by $\left(\tilde{r}, \tilde{\theta}, \tilde{\phi}\right)$, where $\theta = \tilde{\theta}$ and $\phi = \tilde{\phi}$ due to radial symmetry. The two configurations are related arbitrarily by

$$\tilde{r} = f(r)\, r, \qquad \theta = \tilde{\theta}, \qquad \phi = \tilde{\phi}$$

and the deformation is

$$u_r = (f(r) - 1)\, r, \qquad u_\theta = 0, \qquad u_\phi = 0. \tag{B.1}$$

The deformation gradient tensor is [62]

$$\boldsymbol{F} = \boldsymbol{I} + \nabla \boldsymbol{u}$$

and thus

$$\boldsymbol{F} = \begin{bmatrix} f'r + f & 0 & 0 \\ 0 & f & 0 \\ 0 & 0 & f \end{bmatrix}. \tag{B.2}$$

The principal stretches are the diagonal terms of Eq. (B.2), such that

$$\lambda_{rr} = f'r + f, \qquad \lambda_{\theta\theta} = \lambda_{\phi\phi} = f. \tag{B.3}$$

For derivation purposes, it is simpler to consider the Biot stress, T. The components of the Biot stress are related to the strain energy density, $\mathscr{E}$, such that [64]

$$T_{ij} = \frac{\partial \mathcal{E}}{\partial \lambda_{ij}}. \tag{B.4}$$

Equilibrium in the absence of body forces requires $T_{ij,j} = 0$, which yields the following three equations in spherical coordinates [64]:

$$\frac{\partial T_{rr}}{\partial r} + \frac{1}{r}\frac{\partial T_{r\theta}}{\partial \theta} + \frac{1}{r\sin\theta}\frac{\partial T_{r\phi}}{\partial \phi} + \frac{2T_{rr} - T_{\theta\theta} - T_{\phi\phi} - T_{r\theta}\cos\phi}{r} = 0, \tag{B.5}$$

$$\frac{\partial T_{r\theta}}{\partial r} + \frac{1}{r}\frac{\partial T_{\theta\theta}}{\partial \theta} + \frac{1}{r\sin\theta}\frac{\partial T_{\theta\phi}}{\partial \phi} + \frac{(T_{\theta\theta} - T_{\phi\phi})\cot\theta + 3T_{r\theta}}{r} = 0, \tag{B.6}$$

$$\frac{\partial T_{r\phi}}{\partial r} + \frac{1}{r}\frac{\partial T_{\phi\theta}}{\partial \theta} + \frac{1}{r\sin\theta}\frac{\partial T_{\phi\phi}}{\partial \phi} + \frac{2T_{\theta\phi}\cot\theta + 3T_{r\phi}}{r} = 0. \tag{B.7}$$

The stress tensor will have the same form as the deformation gradient given in Eq. (B.2). Therefore, the only non-zero components of the stress tensor are

T_{rr} and $T_{\theta\theta} = T_{\phi\phi}$ and Eq. (B.6) and (B.7) are trivially satisfied and Eq. (B.5) reduces to

$$\frac{\partial T_{rr}}{\partial r} + \frac{2}{r}\left(T_{rr} - T_{\theta\theta}\right) = 0. \tag{B.8}$$

The expression for the strain energy density of the nonlinear matrix assumed in Ref. [6] is

$$\mathscr{E} = c_1 I_1^3 + c_2 I_1^2 + c_3 I_1 + c_4 - c_5 I_2 + c_6 I_3 \tag{B.9}$$

where I_1, I_2, and I_3 are the principal invariants of the strain tensor of the deformation gradient.

$$\begin{aligned} I_1 &= \lambda_{rr} + \lambda_{\theta\theta} + \lambda_{\phi\phi}, \\ I_2 &= \lambda_{rr}\lambda_{\theta\theta} + \lambda_{rr}\lambda_{\phi\phi} + \lambda_{\theta\theta}\lambda_{\phi\phi}, \\ I_3 &= \lambda_{rr}\lambda_{\theta\theta}\lambda_{\phi\phi}. \end{aligned} \tag{B.10}$$

If the matrix is assumed to be linear, the strain energy density is at most second order with respect to the invariants, such that the stress is first order. Therefore, $c_1 = 0$ and $c_6 = 0$. Expressing the strain energy density in terms of invariants,

$$\mathscr{E} = c_2\lambda_{rr}^2 + 2\left(c_2 - c_5\right)\lambda_{rr}\lambda_\theta\theta + \left(4c_2 - c_5\right)\lambda_{\theta\theta}^2 + c_3\left(\lambda_{rr} + 2\lambda_{\theta\theta}\right). \tag{B.11}$$

Since c_4 is a constant, it will not appear in the stress terms and it has also been set to zero. From Eqs. (B.4), (B.10) and (B.11), and using $\lambda_\phi = \lambda_\theta$, the stress components become

$$\begin{aligned} T_{rr} &= 2c_2\left(\lambda_{rr} + 2\lambda_{\theta\theta}\right) + c_3 - 2c_5\lambda_{\theta\theta}, \\ T_{\theta\theta} &= 2c_2\left(\lambda_{rr} + 2\lambda_{\theta\theta}\right) + c_3 - c_5\left(\lambda_{rr} + \lambda_{\theta\theta}\right), \end{aligned}$$

and equilibrium occurs when

$$\begin{aligned}
&\frac{\partial}{\partial r}\left[2c_2\left(\lambda_{rr}+2\lambda_{\theta\theta}\right)+c_3-2c_5\lambda_{\theta\theta}\right]+\frac{2c_5}{r}\left(\lambda_{rr}-\lambda_{\theta\theta}\right)=0\\
&2c_2\frac{\partial}{\partial r}\left(f'r+3f\right)-2c_5f'+\frac{2c_5}{r}f'r=0\\
&\frac{\partial}{\partial r}\left(f'r+3f\right)=0.
\end{aligned} \tag{B.12}$$

The last equation given in Eq. (B.12) can be integrated to yield

$$f=1+a+\frac{b}{r^3} \tag{B.13}$$

Using Eq. (B.13) in Eq. (B.1) yields the following expression for the radial displacement,

$$u_r=ar+\frac{b}{r^2}. \tag{B.14}$$

Similarly, the principal stretches of the deformation gradient are now expressed as

$$\lambda_{rr}=1+a-\frac{2b}{r^3},\qquad \lambda_{\theta\theta}=1+a+\frac{b}{r^3}. \tag{B.15}$$

A linear stress-strain constitutive relationship for the harmonic material only contains terms up first order with respect to the principal stretches. The strain energy density is therefore second order with respect to the invariants. The components of the strain tensor and the principal stretches are related such that $E_{ij}=\lambda_{ij}-1$. Thus, the Biot stress is [6]

$$T_{rr}=2c_2E_{rr}+2\left(2c_2-c_5\right)E_{\theta\theta}+6c_2+c_3-2c_5 \tag{B.16}$$

The reference configuration is stress-free, such that $E_{rr} = E_{\theta\theta} = 0$ and $T_{rr} = 0$, which gives rise to

$$c_3 = 2c_5 - 6c_2$$

The small strain limit of the radial stress is

$$T_{rr} = \left(K + \frac{4}{3}\mu\right) E_{rr} + 2\left(K - \frac{2}{3}\mu\right) E_{\theta\theta}. \tag{B.17}$$

Equating Eqs. (B.17) and (B.16) allows c_2 and c_5 to be defined in terms of K and μ, such that

$$c_2 = \frac{1}{2}\left(K + \frac{4}{3}\mu\right),$$
$$c_5 = \left(K + \frac{4}{3}\mu\right) - \left(K - \frac{2}{3}\mu\right) = 2\mu.$$

Expressions for the Biot stress, and strain energy density, can then be obtained in terms of the elastic moduli, K and μ, as in Ref. [6], such that

$$T_{rr} = \left(K + \frac{4}{3}\mu\right) E_{rr} + 2\left(K - \frac{2}{3}\mu\right) E_{\theta\theta}, \tag{B.18}$$

$$\begin{aligned}\mathscr{E} = &\frac{1}{2}\left(K + \frac{4}{3}\mu\right)\lambda_{rr}^2 + 2\left(K - \frac{2}{3}\mu\right)\lambda_{rr}\lambda_{\theta\theta} \\ &+ 2\left(K - \frac{1}{3}\mu\right)\lambda_{\theta\theta}^2 - 3K\left(\lambda_{rr} + 2\lambda_{\theta\theta}\right).\end{aligned} \tag{B.19}$$

The present work considers the Cauchy Stress instead of the Biot Stress. The radial component of the Cauchy stress is obtained from the strain energy density by [86]

$$\sigma_{rr} = \frac{1}{\lambda_{\theta\theta}^2}\frac{\partial \mathcal{E}}{\partial \lambda_{rr}}. \tag{B.20}$$

The radial component of the Cauchy stress is therefore,

$$\sigma_{rr} = \frac{1}{\lambda_{\theta\theta}^2}\left[\left(K + \frac{4}{3}\mu\right)\lambda_{rr} + 2\left(K - \frac{2}{3}\mu\right)\lambda_{\theta\theta} - 3K\right], \tag{B.21}$$

or

$$\sigma_{rr} = \left(1 + a + \frac{b}{r^3}\right)^{-2}\left(3Ka + \frac{2\mu b}{r^3}\right). \tag{B.22}$$

Equation (B.22) is the same expression used in Section 3.2.2.

Appendix C

Time Domain Algorithm Including Cubic Nonlinearity

The equation being modeled by the time domain code is

$$\frac{\partial P}{\partial \sigma} = \left(N_1 P + N_2 P^2\right) \frac{\partial P}{\partial \theta} + \frac{1}{\Gamma} \frac{\partial^2 P}{\partial \theta^2}, \tag{C.1}$$

as given by Eq. (3.65). Operator splitting of Eq. (C.1) into one differential equation for attenuation and another for nonlinear distortion, similar to what was done to derive the evolution equation, is applied here. The two equations are solved independently over spatial incremental step $\Delta\sigma$, which is known as the method of fractional steps. The analysis presented in Refs. [92] and [93] demonstrates that solving these equations separately converges to the correct answer for small enough step sizes.

C.1 Nonlinear Distortion

The dimensionless equation that models nonlinear distortion is

$$\frac{\partial P}{\partial \sigma} = \left(N_1 P + N_2 P^2\right) \frac{\partial P}{\partial \theta}. \tag{C.2}$$

This is solved analytically using the Poisson solution,

$$P\left(\sigma, \theta\right) = F\left[\theta + \sigma\left(N_1 P + N_2 P^2\right)\right], \tag{C.3}$$

where $F(\theta)$ is the waveform at source, $\sigma = 0$. If the source is a sinusoid, $F(\theta) = \sin\theta$. Propagation of waveform as it steps forward from $\sigma = 0$ at $\Delta\sigma$ increments is given by

$$P\left(\sigma + \Delta\sigma, \theta\right) = P\left[\sigma, \theta + \Delta\sigma\left(N_1 P + N_2 P^2\right)\right]. \tag{C.4}$$

The dimensionless time is thus transformed according to

$$\theta_i^{k+1} = \theta_i^k - \Delta\sigma\left[N_1\left(P_i^k\right) + N_2\left(P_i^k\right)^2\right], \tag{C.5}$$

where k corresponds to the current value of σ and $k+1$ corresponds to $\sigma + \Delta\sigma$. The subscripts i refer to the time step, which goes from 1 to M. The code cannot correctly model multivalued waveforms, thus $\theta_1^{k+1} < \theta_2^{k+1} < ... < \theta_M^{k+1}$ must be true for all times. This means

$$\Delta\sigma < \frac{\Delta\theta}{\max\left|P_i^k - P_{i-1}^k\right|}. \tag{C.6}$$

The times steps are no longer uniform and must be resampled via linear interpolation.

C.2 Thermoviscous Absorption

The component of the algorithm accounting for absorption in the time domain code remains unaltered, but is repeated below for convenience. The linear, lossy, dimensionless evolution equation is given as

$$\frac{\partial P}{\partial \sigma} = \frac{1}{\Gamma}\frac{\partial^2 P}{\partial \theta^2}. \tag{C.7}$$

A Crank-Nicolson method using standard forward-space, centered time finite differences is used to solve Eq. (C.7), such that

$$\frac{P_i^{k+1} - P_i^k}{\Delta\sigma} = \frac{1}{2\Gamma\left(\Delta\theta\right)^2}\left(P_{i+1}^{k+1} - 2P_i^{k+1} + P_{i-1}^{k+1} + P_{i+1}^k - 2P_i^k + P_{i-1}^k\right). \quad \text{(C.8)}$$

Letting $r = (\Delta\sigma)/[2\Gamma\left(\Delta\theta\right)^2]$, Eq. (C.8) can be rewritten as

$$-rP_{i-1}^{k+1} + (1+2r)\,P_i^{k+1} - rP_{i+1}^{k+1} = rP_{i-1}^k + (1-2r)\,P_i^k + rP_{i+1}^k, \quad \text{(C.9)}$$

where $\boldsymbol{P}^{k+1}$ is the output solution vector to be solved for at each time step i and $\boldsymbol{P}^k$ is a vector of the output from the previous iteration at each time step, such that $(\theta_i^{k+1}, P_i^{k+1})$ becomes (θ_i^k, P_i^k) at the next iteration, and $P^k = \left(P_1^k, P_2^k, ..., P_M^k\right)^T$. Thus, the system of equations is expressed as:

$$A_{\text{tv}} \cdot \boldsymbol{P}^{k+1} = B_{\text{tv}} \cdot \boldsymbol{P}^k, \quad \text{(C.10)}$$

where A_{tv} and B_{tv} are the following tridiagonal matrices:

$$A_{\text{tv}} = \begin{bmatrix} 1 & 0 & & \\ -r & 1+2r & -r & \\ & \ddots & \ddots & \ddots \\ & -r & 1+2r & -r \\ & & 0 & 1 \end{bmatrix}, \qquad B_{\text{tv}} = \begin{bmatrix} 1 & 0 & & \\ r & 1-2r & r & \\ & \ddots & \ddots & \ddots \\ & r & 1-2r & r \\ & & 0 & 1 \end{bmatrix},$$

from Eq. (C.9). P^{k+1} is calculated explicitly using the Thomas algorithm, which is a simplified form of Gaussian elimination used to solve tridiagonal systems of equations:

$$a_i P_{i-1}^{k+1} + b_i P_i^{k+1} + c_i P_{i+1}^{k+1} = d_i. \quad \text{(C.11)}$$

In Gaussian elimination, there is a change of coefficients such that

$$e_i = \begin{cases} c_1/b_1 & \text{for } i = 1 \\ c_i/\left(b_i - a_i e_{i-1}\right) & \text{for } i = 2, 3, ..., M \end{cases} \tag{C.12}$$

and

$$f_i = \begin{cases} d_1/b_1 & \text{for } i = 1 \\ \left(d_i - a_i f_{i-1}\right)/\left(b_i - a_i e_{i-1}\right) & \text{for } i = 2, 3, ..., M \end{cases} \tag{C.13}$$

Backwards substitution provides the following expressions for P_i^{k+1},

$$P_i^{k+1} = \begin{cases} f_M & \text{for } i = M \\ f_i - e_i P_{i+1}^{k+1} & \text{for } i = M-1, M-2, ..., 1 \end{cases}. \tag{C.14}$$

P_n^{k+1} then becomes P_n^k for the next iteration in the algorithm.

Appendix D

Derivation of Rayleigh-Plesset Type Equation

There are several ways to derive the Rayleigh-Plesset equation. The following approach utilizes Lagrange's equation, as outlined in Refs. [99] and [100]:

$$\frac{d}{dt}\left(\frac{\partial L}{\partial \dot{R}}\right) - \frac{\partial L}{\partial R} = -\frac{\partial \Psi}{\partial \dot{R}}, \tag{D.1}$$

where the Lagrangian, $L = T - U$, depends on the total kinetic energy T and total potential energy U, Ψ is a dissipative function, and R is the instantaneous radius. No component of the potential energy function, U, depends on time, such that Eq. (D.1) reduces to

$$\frac{d}{dt}\left(\frac{\partial T}{\partial \dot{R}}\right) - \frac{\partial T}{\partial R} = -\frac{\partial U}{\partial R} - \frac{\partial \Psi}{\partial \dot{R}}. \tag{D.2}$$

The derivation implements the assumptions discussed in Section 4.2. The first neglects the kinetic energy of the inclusion in both cases considered in Chapter 4. The mass of the inclusion can be accounted for easily, such as in Ref. [101], and will be included in future work. However, for the present derivation, the total kinetic energy is just that of the nearly incompressible matrix; thus [99]

$$T_{\text{total}} = T_{\text{M}} = 2\pi\rho_{\text{M}} R^3 \dot{R}^2. \tag{D.3}$$

The total potential energy on the surface of the sphere of interest is thus the summation of the potential energy due to work done by any external forces on the outer surface of the matrix, the strain energy of the surrounding matrix material, and the internal strain energy the inclusion in general, which may refer to a bubble, a SAMM element, or an effective medium. The work done by the outer surface of the matrix due to some pressure, P_∞, is given by

$$U_\infty = P_\infty V_0 \varepsilon_v, \tag{D.4}$$

where P_∞ includes two components, an acoustic forcing pressure, P_{ac}, and a static pressure, P_0 that serves as a 'DC offset' pressure. The pressure is assumed to be incident infinitely far away from the surface of the sphere.

The stored energy from the incompressible elastic matrix is derived in Ref. [99] up to second order in radius of the bubble, but only the linear approximation is of interest here. The strain energy density of a nearly incompressible matrix in terms of the shear modulus of the matrix, μ_{M} is thus expressed as

$$\mathscr{E}_{\text{M}} = \frac{2}{3}\mu_{\text{M}} \left(\frac{R_0}{r}\right)^6 \varepsilon_v^2. \tag{D.5}$$

The potential energy of the matrix is found by integrating the strain energy density given in Eq. (D.5) over the total volume of the matrix, originating at the boundary of the sphere and ending at the outer surface of the matrix, which is assumed to be infinitely far away, such that [99]

$$U_{\text{M}} = 4\pi \int_{r=R_0}^{\infty} \mathscr{E}_{\text{M}} r^2 dr = \frac{2}{3}\mu_{\text{M}} V_0 \varepsilon_v^2, \tag{D.6}$$

where R_0, V_0 and ε_v refer to the equilibrium radius, equilibrium volume and volumetric strain of the sphere.

When deriving the Hashin-Shtrikman bounds in Section 3.2.2.1, both the SAMM inclusion and effective medium obeyed a constitutive relationship of the same form. This also applies to the potential energy, which can be expressed as the following expansion

$$U = V_0 \left(\frac{1}{2} K \varepsilon_v^2 - \frac{1}{6} K' \varepsilon_v^3 + \frac{1}{24} K'' \varepsilon_v^4 \right). \tag{D.7}$$

The derivative of strain energy with respect to radius R as a function of pressure, as required for Lagrange's equation given in Eq. (D.2), is

$$-\frac{\partial U}{\partial R} = 4\pi R^2 P. \tag{D.8}$$

As a first level approximation, it is assumed that the only dissipation comes from the incompressible matrix and the dissipation factor, as given in Ref. [100], is

$$\Psi_{\text{M}} = 8\pi \eta_{\text{M}} R \dot{R}^2 \tag{D.9}$$

where η_{M} is the shear viscosity of the matrix. Using Eqs. (D.2), (D.3), (D.8), and the differentiation Eq. (D.9) with respect to $\dot{R}$, yields a differential equation for change in radius as a function of time,

$$4\pi \rho_{\text{M}} R^3 \ddot{R} + 6\pi \rho_{\text{M}} R^2 \dot{R}^2 = 4\pi R^2 P_{\text{total}} - \frac{4\eta_{\text{M}}}{\rho_{\text{M}}} \frac{\dot{R}}{R},$$

which is commonly expressed as

$$R\ddot{R} + \frac{3}{2}\dot{R}^2 = \frac{P_{\text{total}}}{\rho_{\text{M}}} - \frac{4\eta_{\text{M}}}{\rho_{\text{M}}} \frac{\dot{R}}{R}, \tag{D.10}$$

where the dots indicate derivatives with respect to time. The total pressure is obtained by differentiating the strain energy with respect to R, as given in Eq. (D.8). Differentiating Eq. (D.4) with respect to R provides a $-P_\infty$ contribution, whereas contributions to the total pressure for the matrix and the inclusion are both positive due to how the pressure is defined. The total pressure will have the following form in Chapter 4

$$P_{\text{total}} = P_{\text{I},*} + P_{\text{M}} - P_\infty \tag{D.11}$$

where $P_{\text{I},*}$ is the internal pressure of either the SAMM inclusion or effective medium and P_{M} is evaluated on the surface of the sphere.

Bibliography

[1] Z. Hashin, "Analysis of composite materials: A survey," *J. Appl. Mech.*, vol. 50, pp. 481–505, 1983.

[2] R. M. Christensen, *Mechanics of Composite Materials*. Dover Publications, Inc., 2005, pp. 47–51.

[3] D. T. Blackstock, M. F. Hamilton, and A. D. Pierce, "Progressive waves in lossless and lossy fluids," in *Nonlinear Acoustics*, M. F. Hamilton and D. T. Blackstock, Eds. Acoustical Society of America, 2008, ch. 4, pp. 71–74, 132–133.

[4] O. V. Rudenko, "Giant nonlinearities in structurally inhomogenous media and the fundamentals of nonlinear acoustic diagnostic techniques," *Phys.-Usp.*, vol. 49, no. 1, pp. 69–87, 2006.

[5] X. Guo, Z. Lin, J. Tu, B. Liang, J. Cheng, and D. Zhang, "Modeling and optimization of an acoustic diode based on micro-bubble nonlinearity," *J. Acoust. Soc. Am.*, vol. 133, no. 2, pp. 1119–1125, 2013.

[6] R. S. Lakes and W. J. Drugan, "Dramatically stiffer elastic composite material due to a negative stiffness phase?" *J. Mech. Phys. Solids*, vol. 50, pp. 979–1009, 2002.

[7] A. N. Norris and M. R. Haberman, "Introduction to the special issue on acoustic metamaterials," *J. Acoust. Soc. Am.*, vol. 132, no. 4, p. 2783, 2012.

[8] S. Guenneau and R. V. Craster, "Fundamentals of acoustic metamaterials," in *Acoustic Metamaterials: Negative Refraction, Imaging, Lensing and Cloaking*, R. V. Craster and S. Guenneau, Eds. Springer, 2013, ch. 1, pp. 2–4, 34.

[9] W. Thomson, "XLVI. On the reflexion and refraction of light," *Philos. Mag. Series 5*, vol. 26, no. 162, pp. 414–425, 1888.

[10] V. G. Veselago, "The electrodynamics of substances with simulataneous negative values of ϵ and μ," *Soviet Physics Uspekhi*, vol. 10, no. 4, pp. 509–514, 1968.

[11] R. A. Shelby, D. R. Smith, and S. Schultz, "Experimental verification of a negative index of refraction," *Science*, vol. 292, no. 77, p. 1058847, 2001.

[12] B. Banerjee, *An Introduction to Metamaterials and Waves in Composites*. CRC Press, 2011, ch. 4, pp. 133–135.

[13] K. Bertoldi and M. C. Boyce, "Mechanically triggered transformations of phononic band gaps in periodic elastomeric structures," *Phys. Rev. B*, vol. 77, p. 052105, 2008.

[14] N. Boechler, G. Theocharis, and C. Daraio, "Bifurcation-based acoustic switching and rectification," *Nat. Mater.*, vol. 10, pp. 665–668, 2011.

[15] N. Fang, D. Xi, J. Xu, M. Ambati, W. Srituravanich, C. Sun, and X. Zhang, "Ultrasonic metamaterials with negative modulus," *Nat. Mater.*, vol. 5, pp. 452–456, 2006.

[16] Z. Liu, X. Zhang, Y. Mao, Y. Y. Zhu, Z. Yang, C. T. Chan, and P. Sheng, "Locally resonant sonic materials," *Science*, vol. 289, pp. 1734–1736, 2000.

[17] L. Zigoneanua, B.-I. Popa, and S. A. Cummer, "Design and measurement of a broadband two-dimensional acoustic lens," *Phys. Rev. B*, vol. 84, p. 024305, 2011.

[18] S. A. Cummer, B.-I. Popa, D. Schurig, D. R. Smith, J. Pendry, M. Rahm, and A. Starr, "Scattering theory derivation of a 3D aoucstic cloaking shell," *Phys. Rev. Lett.*, vol. 100, p. 024301, 2008.

[19] H. H. Huang, C. T. Sun, and G. L. Huang, "On the negative effective mass density in acoustic metamaterials," *Int. J. Eng. Sci.*, vol. 47, pp. 610–617, 2009.

[20] M. R. Haberman, "Design of high loss viscoelastic composites through micromechanical modeling and descision based materials design," Ph.D. dissertation, Georgia Institute of Technology, 2007.

[21] T. Klatt and M. R. Haberman, "A nonlinear negative stiffness metamaterial unit cell and small-on-large multiscale material model," *J. Appl. Phys.*, vol. 114, p. 033503, 2013.

[22] S. P. Timoshenko and J. M. Gere, *Theory of Elastic Stability.* McGraw-Hill Book Company, Inc., 1961, pp. vii–viii, 46–47.

[23] J. S. Humphreys, "On dynamic snap buckling of shallow arches," *AIAA J.*, vol. 4, no. 5, pp. 878–886, 1966.

[24] C. S. Wojnar and D. M. Kochmann, "A negative-stiffness phase in elastic composites can produce stable extreme effective dynamics but not static stiffness," *Philos. Mag.*, vol. 94, no. 6, pp. 532–555, 2013.

[25] A. Khelif, Y. Achaoui, and B. Aoubiza, "Locally resonant structures for low freqeuncy surface acoustic band gap applications," in *Acoustic Metamaterials: Negative Refraction, Imaging, Lensing and Cloaking*, R. V. Craster and S. Guenneau, Eds. Springer, 2013, ch. 2, pp. 44–45.

[26] M. Gei, D. Bigoni, A. B. Movchan, and M. Bacca, "Band-gap properties of prestressed structures," in *Acoustic Metamaterials: Negative Refraction, Imaging, Lensing and Cloaking*, R. V. Craster and S. Guenneau, Eds. Springer, 2013, ch. 3, p. 61.

[27] Z. Liu, C. T. Chan, and P. Sheng, "Analytical model of phononic crystals with local resonances," *Phy. Rev. B*, vol. 71, p. 014103, 2005.

[28] A. B. Movchan and S. Guenneau, "Split-ring resonators and localized modes," *Phys. Rev. B*, vol. 70, p. 125116, 2004.

[29] J. Li and C. T. Chan, "Double-negative acoustic metamaterials," *Phys. Rev. E*, vol. 70, p. 055602, 2004.

[30] S. Guenneau, A. Movchan, G. Pétursson, and S. A. Ramakrishna, "Acoustic metamaterials for sound focusing and confinement," *New J. Phys.*, vol. 9, p. 399, 2007.

[31] R. S. Lakes, T. Lee, A. Bersie, and Y. C. Wang, "Extreme damping in composite materials with negative-stiffness inclusions," *Nature*, vol. 410, pp. 565–567, 2001.

[32] R. S. Lakes, "Extreme damping in composite materials with a negative stiffness phase," *Phys. Rev. Lett.*, vol. 86, no. 13, pp. 2897–2900, 2001.

[33] H. Kalathur and R. S. Lakes, "Column dampers iwth negative stiffness: high damping at small amplitudes," *Smart Mater. Struc.*, vol. 22, p. 084013, 2013.

[34] L. Dong and R. Lakes, "Advanced damper with high stiffness and high hysteresis damping based on negative strucutral stiffness," *Int. J. Solids Struc.*, vol. 50, pp. 2416–2423, 2013.

[35] R. S. Lakes, "Extreme damping in compliant composites with a negative-stiffness phase," *Phil. Mag. Lett.*, vol. 81, no. 2, pp. 95–100, 2001.

[36] H. W. Yap, R. S. Lakes, and R. W. Carpick, "Negative stiffness and enhanced damping of individual multiwalled carbon nanotubes," *Phys. Rev. B*, vol. 77, p. 045423, 2008.

[37] D. M. Kochmann and W. J. Drugan, "Analytical stability conditions for elastic composite materials with a non-positive-definite phase," *Proc. R. Sco. A*, vol. 465, no. 2144, pp. 2230–2254, 2012.

[38] B. A. Fulcher, D. W. Shahan, M. R. Haberman, C. C. Seepersad, and P. S. Wilson, "Analytical and experimental investigation of buckled beams as negative stiffness elements for passive vibration and shock isolation systems," *J. Vib. Acoust.*, vol. 136, no. 3, p. 031009, 2014.

[39] A. Carella, M. J. Brennan, and T. P. Waters, "Static analysis of a passive vibration isolator with quasi-zero-stiffness characteristic," *J. Sound Vib.*, vol. 301, pp. 678–689, 2007.

[40] W. G. Molyneux, "Supports for vibration isolation," Aeronautical Research Council, U.K., Tech. Rep. C.P. No. 322, 1957.

[41] J. van Eijk and J. F. Dijksman, "Plate spring mechanism with constant negative stiffness," *Mech. Mach. Theory*, vol. 14, pp. 1–9, 1979.

[42] D. L. Platus, "Negative-stiffness-mechanism vibration isolation system," *Vib. Control Microelectron. Opt. Metrol.*, vol. 1619, pp. 44–54, 1991.

[43] D. L. Platus, "Negative-stiffness-mechanism vibration isolation systems," in *Part of the SPIE Conference on Current Development in VIbraiton*

Control for Optomechanical Systems, Denver, Colorado, July 1999, vol. 3786. Denver, Colorado, USA: SPIE, 1999, pp. 98–105.

[44] C.-M. Lee, V. N. Goverdovskiy, and A. I. Temnikov, "Design of springs with 'negative' stiffness to improve vehicle driver vibration isolation," *J. Sound Vib.*, vol. 302, pp. 865–874, 2007.

[45] C.-M. Lee and V. N. Goverdovskiy, "A multi-stage high-speed railroad vibration isolation system with 'negative' stiffness," *J. Sound Vib.*, vol. 331, pp. 914–921, 2012.

[46] D. D. Quinn, S. Hubbard, N. Wierschem, M. A. Al-shudeifat, R. J. Ott, J. Luo, B. F. Spencer Jr., D. M. McFarland, A. F. Vakakis, and L. A. Bergman, "Equivalent modal damping, stiffening and energy exchanges in multi-degree-of-freedom systems with strongly nonlinear attachments," *J. Multi-body Dynamics*, vol. 226, no. 2, pp. 122–146, 2012.

[47] M. A. Al-Shudeifat, "Highly efficient nonlinear energy sink," *Nonlinear Dyn.*, vol. 76, pp. 1905–1920, 2014.

[48] K. L. Manktelow, M. J. Leamy, and M. Ruzzene, "Analysis and experimental estimation of nonlinear dispersion in a periodic string," *J. Vib. Acoust.*, vol. 136, no. 3, p. 031016, 2014.

[49] B. S. Lazarov and J. S. Jensen, "Low-frequency band gaps in chains with attached non-linear oscillators," *Int. J. Nonlinear Mech.*, vol. 42, pp. 1186–1193, 2007.

[50] K. Bertoldi and M. C. Boyce, "Wave propagation and instabilities in monolithic and periodically structured elastomeric materials undergoing large deformations," *Phys. Rev. B*, vol. 78, p. 184107, 2008.

[51] J.-H. Jang, C. H. Koh, K. Bertoldi, M. C. Boyce, and E. L. Thomas, "Combining pattern instability and shape-memory hysteresis for phonic switching," *Nano Lett.*, vol. 9, no. 5, pp. 2113–2119, 2009.

[52] B. Liang, B. Yuan, and J.-C. Cheng, "Acoustic diode: Rectification of acoustic energy flux in one-dimensional systems," *Phys. Rev. Lett.*, vol. 103, p. 184107, 2008.

[53] T. Klatt, "Extreme energy absorption: The design, modeling and testing of negative stiffness metamaterial inclusions," Master's thesis, The University of Texas at Austin, 2013.

[54] J. Qiu, J. H. Lang, and A. H. Slocum, "A curved-beam bistable mechanism," *J. Microelectromech. S.*, vol. 13, no. 2, pp. 137–146, 2004.

[55] P. M. Morse and K. U. Ingard, *Theoretical Acoustics*. McGraw-Hill Book Company, 1968, pp. 39–41.

[56] A. H. Nayfeh and D. T. Mook, *Nonlinear Oscillators*. John Wiley & Sons, Inc., 1997, pp. 8–9, 40.

[57] G. Duffing, *Erzwungene schwingungen bei veranderlicher eigenfrequenz und ihre technische bedeutung*. Braunschweig, F. Vieweg & sohn, 1918.

[58] L. N. Virgin, *Introduction to Experimental Nonlinear Dynamics: A Case Stuidy in Mechancial Vibration.* Cambridge Univ. Press, 2000, pp. 2, 23–24, 133–134.

[59] R. W. Ogden, "Pseudo-elasticity and stress softening," in *Nonlinear Elasticity: Theory and Applications*, Y. B. Fu and R. W. Ogden, Eds. Cambridge Univ. Press, 2001, ch. 13, pp. 491–494.

[60] R. W. Ogden, "Elements of the theory of finite elasticity," in *Nonlinear Elasticity: Theory and Applications*, Y. B. Fu and R. W. Ogden, Eds. Cambridge Univ. Press, 2001, ch. 1, pp. 19–21.

[61] J. M. Hill, "Exact integrals and solutions for finite deformations of the incompressible Varga elastic materials," in *Nonlinear Elasticity: Theory and Applications*, Y. B. Fu and R. W. Ogden, Eds. Cambridge Univ. Press, 2001, ch. 5, pp. 162–163.

[62] Y. C. Fung and P. Tong, *Classical and Computational Solid Mechanics.* World Scientific Publishing Co. Pte. Ltd., 2001, pp. 118–119, 139–140, 421.

[63] E. A. Jackson, *Perspectives on Nonlinear Dynamics I.* Cambridge Univ. Press, 1991, pp. 36–39.

[64] R. W. Ogden, *Non-linear Elastic Deformations.* Dover Publications, Inc., 1984, pp. 66, 246–251.

[65] A. N. Norris, "Finite-amplitude waves in solids," in *Nonlinear Acoustics*, M. F. Hamilton and D. T. Blackstock, Eds. Acoustical Society of America, 2008, ch. 9, p. 266.

[66] J. M. T. Thompson and G. W. Hunt, *A General Theory of Elastic Stability*. John Wily & Sons, 1973, pp. 1–5.

[67] R. T. Beyer, "The parameter B/A," in *Nonlinear Acoustics*, M. F. Hamilton and D. T. Blackstock, Eds. Acoustical Society of America, 2008, ch. 2, pp. 25–37.

[68] M. F. Hamilton and D. T. Blackstock, "On the coefficient of nonlinearity β in nonlinear acoustics," *J. Acoust. Soc. Am.*, vol. 83, no. 1, pp. 74–77, 1988.

[69] S. Kostek, B. K. Sinha, and A. N. Norris, "Third-order elastic constants for an inviscid fluid," *J. Acoust. Soc. Am.*, vol. 94, no. 5, pp. 3014–3017, 1993.

[70] E. A. Zabolotskaya, "Sound beams in a nonlinear isotropic solid," *Sov. Phys. Acoust.*, vol. 32, no. 4, pp. 296–299, 1986.

[71] E. A. Zabolotskaya, M. F. Hamilton, Yu. A. Ilinskii, and G. D. Meegan, "Modeling of nonlinear shear waves in soft solids," *J. Acoust. Soc. Am.*, vol. 116, no. 5, pp. 2807–2813, 2004.

[72] R. T. Beyer, *Nonlinear Acoustics*. The Acoustical Society of America, 1997, pp. 100–101.

[73] A. B. Coppens, R. T. Beyer, M. B. Seiden, J. Donohue, F. Guepin, R. H. Hodson, and C. Townsend, "Parameter of nonlinearity in fluids II," *J. Acoust. Soc. Am.*, vol. 38, pp. 797–804, 1965.

[74] X.-C. Xu, F. Mao, X.-F. Gong, and D. Zhang, "Theoretical calculation and experitmental study on the third-order nonlinearity parameter C/A for organic liquids and biological fluids," *J. Acoust. Soc. Am.*, vol. 113, no. 3, pp. 1743–1748, 2003.

[75] X. Liu, J. Li, X. Gong, Z. Zhu, and D. Zhang, "Theoretical and experimental study of third-order nonlinearity parameter C/A for biological media," *Physica D*, vol. 228, pp. 172–178, 2007.

[76] K. W. Winkler and X. Liu, "Measurements of third-order elastic constants in rocks," *J. Acoust. Soc. Am.*, vol. 100, no. 3, pp. 1392–1398, 1996.

[77] D. S. Hughes and J. L. Kelly, "Second-order elastic deformations of solids," *Phys. Rev.*, vol. 92, no. 5, pp. 1145–1149, 1953.

[78] E. H. Bogardus, "Third order elastic constants of Ge, MgO, and fused SiO2," *J. Appl. Phys.*, vol. 36, no. 8, pp. 2504–2513, 1965.

[79] M. F. Hamilton, Yu. A. Il'inskii, and E. A. Zabolotskaya, "Dispersion," in *Nonlinear Acoustics*, M. F. Hamilton and D. T. Blackstock, Eds. Acoustical Society of America, 2008, ch. 5, pp. 167, 173.

[80] D. H. Trivett, H. Pincon, and P. H. Rogers, "Investigation of a three-phase medium with a negative parameter of nonlinearity," *J. Acoust. Soc. Am.*, vol. 119, no. 6, pp. 3610–3617, 2006.

[81] P. A. Thompson and K. C. Lambrakis, "Negative shock waves," *J. Fluid Mech.*, vol. 60, no. 1, pp. 187–208, 1973.

[82] R. E. Apfel, "The effective nonlinearity parameter for immiscible liquid mixtures," *J. Acoust. Soc. Am.*, vol. 74, no. 6, pp. 1866–1868, 1983.

[83] E. C. Everbach, Z. Zhu, P. Jiang, B. T. Chu, and R. E. Apfel, "A corrected mixture law for B/A," *J. Acoust. Soc. Am.*, vol. 89, no. 1, pp. 446–447, 1991.

[84] E. C. Everbach, "Tissue composition determination via measurement of the acoustic nonlinearity parameter," Ph.D. dissertation, Yale University, 1989.

[85] Z. Hashin and S. Shtrikman, "A variational approach to the theory of the elastic behavior of multiphase materials," *J. Mech. Phys. Solids*, vol. 11, pp. 127–140, 1963.

[86] C. O. Horgan, "Equilibrium solutions for compressible nonlinearly elastic materials," in *Nonlinear Elasticity: Theory and Applications*, Y. B. Fu and R. W. Ogden, Eds. Cambridge Univ. Press, 2001, ch. 4, pp. 135–142.

[87] R. W. Ogden, "Waves in isotropic elastic materials of Hadamard, Green or Harmonic type," *J. Mech. Phys. Solids*, vol. 18, pp. 149–163, 1970.

[88] T. Faez, M. Emmer, K. Kooiman, M. Versluis, A. F. W. van der Steen, and N. de Jong, "20 years of ultrasound constrast agent modeling," *IEEE T. Ultraon. Ferr.*, vol. 60, no. 1, pp. 7–20, 2013.

[89] M. F. Hamilton and E. A. Zabolotskaya, "Nonlinear propagation of sound in a liquid layer between a rigid and a free surface," *J. Acoust. Soc. Am.*, vol. 90, no. 2, pp. 1048–1055, 1991.

[90] M. F. Hamilton and C. L. Morfey, "Model equations," in *Nonlinear Acoustics*, M. F. Hamilton and D. T. Blackstock, Eds. Acoustical Society of America, 2008, ch. 3, pp. 49–50, 56–57.

[91] Y.-S. Lee, "Numerical solution of the KZK equation for pulsed finite amplitude sound beams in thermoviscous fluids," Ph.D. dissertation, The University of Texas at Austin, 1993.

[92] Y.-S. Lee and M. F. Hamilton, "Time-domain modeling of pulse finite-amplitude sound beams," *J. Acoust. Soc. Am.*, vol. 97, no. 2, pp. 906–917, 1995.

[93] R. O. Cleveland, M. F. Hamilton, and D. T. Blackstock, "Time-domain modeling of finite-amplitude sound in relaxing fluids," *J. Acoust. Soc. Am.*, vol. 99, no. 6, pp. 3312–3318, 1996.

[94] M. S. Cramer and A. Kluwick, "On the propagation of waves exhibiting both positive and negative nonlinearity," *J. Fluid Mech.*, vol. 142, pp. 9–37, 1984.

[95] I. P. Lee-Babty and D. G. Crighton, "Nonlinear wave motion governed by the modified Burgers equation," *Phil. Trans. R. Soc. Lond. A*, vol. 323, pp. 173–209, 1987.

[96] S. Garrett, "Nonlinear distortion of 4th sound in superfluid ^{3}He-B," *J. Acoust. Soc. Am.*, vol. 69, no. 1, pp. 139–144, 1981.

[97] R. Lakes, *Viscoelastic Materials*. Cambridge Univ. Press, 2009, pp. 55–63.

[98] T. G. Leighton, *The Bubble Book*. Academic Press Ltd., 1994, pp. 84–85, 287–289, 301–306.

[99] S. Y. Emelianov, M. F. Hamilton, Yu. A. Ilinskii, and E. A. Zabolotskaya, "Nonlinear dynamics of a gas bubble in an incompressible elastic medium," *J. Acoust. Soc. Am.*, vol. 115, no. 2, pp. 581–588, 2004.

[100] E. A. Zabolotskaya, Yu. A. Ilinskii, G. D. Meegan, and M. F. Hamilton, "Modification of the equation for gas bubble dynamics in a soft elastic medium," *J. Acoust. Soc. Am.*, vol. 118, no. 4, pp. 2173–2181, 2005.

[101] E. A. Zabolotskaya, Yu. A. Ilinskii, and M. F. Hamilton, "Weakly nonlinear oscillations of a compliant object buried in soil," *J. Acoust. Soc. Am.*, vol. 125, no. 4, pp. 2035–2040, 2008.

[102] N. Cohen, I. Bucher, and M. Feldman, "Slow-fast response decompostion of a bi-stable eneryg harvester," *Mech. Syst. Signal Pr.*, vol. 38, pp. 797–804, 1965.

[103] R. Abeyaratne and C. O. Horgan, "The pressurized hollow sphere problem in finite elastostatics for a class of compressible materials," *Int. J. Solids Structures*, vol. 20, no. 8, pp. 715–723, 1984.